2010-03-01

Dispersion of Single-Walled Carbon Nanotubes in Organic Solvents

Qiaohuan Cheng
Technological University Dublin, qiaohuan.cheng@tudublin.ie

Dispersion of Single-Walled Carbon Nanotubes in Organic Solvents

By

Qiaohuan Cheng BEng MEng

A thesis submitted to the Dublin Institute of Technology
for the degree of Doctor of Philosophy (PhD)

School of Physics
Dublin Institute of Technology
Kevin Street, Dublin 8

Prof. Hugh J. Byrne and Dr. Elizabeth Gregan

March 2010

ABSTRACT

This thesis contains a systematic study of the dispersion of pristine HiPco Single Walled Carbon Nanotubes (SWNTs) in a series of organic solvents. A double beamed UV-Vis-NIR absorption spectrometer coupled with an integrating sphere was employed to demonstrate the dispersibility of SWNTs in different solvents. Raman Spectroscopy and Atomic Force Microscopy (AFM) were used to confirm the debundling and exfoliation of SWNTs aggregates.

An investigation of the solubility of SWNTs in four chlorinated aromatic solvents demonstrated that the similarity in structure between solvent molecules and nanotube sidewall is not a dominant factor to obtain stable SWNT solutions. A comparative study of the solubility of SWNTs between the aromatic solvents and other reported solvents was then conducted, in terms of the solvent solubility parameters, including Hildebrand and Hansen solubility parameters. Although the established correlation between extinction/absorption coefficients as a function of Hildebrand/Hansen solubility parameters indicated there may be a selective debundling of metallic and semiconducting SWNTs in different solvents, this was not confirmed by a detailed Raman investigation. A further study of the dispersion limit of SWNTs in different solvents as a function of the solvent solubility parameters was carried out. Good agreement with literature is demonstrated here in terms of Hildebrand parameters, but not in terms of the Hansen solubility parameters. It has been demonstrated that the degree of dispersion is critically dependent on sample preparation conditions, in particular sonication. Finally, the effect of sonication parameters and solvent properties

during the dispersion of SWNTs was investigated. The results indicated that the sonication process is closely dependent on many of the physical parameters of the solvent, including vapour pressure, viscosity, surface tension, density and molecular weight. Longer sonication time and higher sonication power help debundling SWNTs in organic solvents but significantly damage the nanotubes. The choice of solvent should be guided by minimisation of sonication requirements.

DECLARATION

I certify that this thesis which I now submit for examination for the award of doctor of philosophy, is entirely my own work and has not been taken from the work of others save and to the extent that such work has been cited and acknowledged within the text of my work.

This thesis was prepared according to the regulations for postgraduate study by research of the Dublin Institute of Technology and has not been submitted in whole or in part for an award in any other Institute or University.

The work reported on in this thesis conforms to the principles and requirements of the Institiute's guidelines for ethics in research.

The Institute has permission to keep, or lend or to copy this thesis in whole or in part, on condition that any such use of the material or the thesis be duly acknowledged.

Signature _____ Date ____/____/____

Candidate

ACKNOWLEDGEMENTS

I would like to take this opportunity to thank a number of people who gave suggestions, who encouraged me and helped me with their valuable suggestions and assistance.

First of all, I would like to thank Prof. Hugh J. Byrne for giving me the opportunity to do this degree. Thank you so much for all the help and encouragement. I would also like to acknowledge Dr. Elizabeth Gregan for giving me the valuable suggestions and guidance throughout the project.

I would like to express my thanks to all the technicians Anne, Theresa and Luke for there great support and technical advice for my research. Thanks to Andrew for solving the IT problems.

I would like to thank Sourabhi and Priya for giving me so much help in work and life, the time we spent together will be great memories forever.

I also like to thank all my friends who made my life here colorful and pleasant, especially Yiling, Qianling and Momo, I am so lucky to have your accompany in the last 3 years.

Finally, I am very much grateful to my parents, my sisters and brother for all their supports and encourage though out my studies.

ABBREVIATIONS

AFM	Atomic Force Microscope
BWF	Breigt-Wigner-Fano
CCVD	Catalytic Chemical Vapour deposition
CVD	Chemical Vapor Deposition
DBE	1, 2-dibromoethane
DCE	1, 2-dichloroethane
DEA	N, N –diethylacetamide
D_L	Dispersion limit
DMA	N, N -dimethylacetamide
DMF	N, N -dimethylformamide
DMP	N, N -dimethylpropanamide
DMSO	Dimethyl sulfoxide
DOS	Density of States
GQD	Graphene quantum dots
GNR	Graphene nanoribbons
HiPco	High pressure CO disproportionation process
HMPA	Hexamethylphosphoramide
m-DCB	meta-dichlorobenzene
MWNTs	Multi-Walled Carbon Nanotubes
NMP	N -methylpyrrolidinone
o-DCB	ortho-dichlorobenzene
SDS	Sodium Dodecyl Sulfate

SPM	Scanning Probe microscopy
STM	Scanning Tunneling Microscopy
SWNTs	Single Walled Carbon Nanotubes
TCB	1, 2, 4-trichlorobenzene
TEM	Transmission Electron Microscopy
UHV-STM	Ultrahigh-vacuum scanning tunnelling microscopy
UV-Vis-NIR	Ultra violet– visible-near infrared

TABLE OF CONTENTS

ABSTRACT i

DECLARATION iii

ACKNOWLEDGEMENTS iv

ABBREVIATIONS v

CHAPTER 1 1

INTRODUCTION 1

1.1 Research background 1

1.2 Research objectives 5

1.3 Thesis outline 6

1.4 References 9

CHAPTER 2 15

SINGLE WALLED CARBON NANOTUBES 15

2.1 What are Single Walled Carbon Nanotubes? 15

2.2 Why are SWNTs so interesting? 18

2.2.1 Electronic properties 18

2.2.2 Mechanical properties 22

2.2.3 Thermal conductivity 22

2.2.4 Nanoscale electronic properties 23

2.3 What are the applications of SWNTs? 23

2.4 How to Produce SWNTs? 24

2.4.1 Electric arc discharge 25

2.4.2 Laser vaporization 26

2.4.3 Chemical vapour deposition (CVD) 27
2.4.4 High pressure decomposition of CO (HiPco) 28
2.5 What are the problems preventing industrial applications? 29
2.6 How to solve the problems? 30
2.7 Summary 31
2.8 Reference 32
CHAPTER 3 45
CHARACTERIZATION TECHNIQUES 45
3.1 UV-Vis-NIR Spectroscopy 45
3.1.1 Absorbance and Scattering 45
3.1.2 UV-Vis-NIR Spectrometer with integrating sphere 49
3.1.3 UV-Vis-NIR spectroscopy of SWNTs 52
3.2 Resonant Raman Spectroscopy 55
3.2.1 Introduction of Resonant Raman spectroscopy 56
3.2.2 Raman Spectroscopy of SWNTs 58
3.2.2.1 The Radial Breathing Mode (RBM) 59
3.2.2.2 The G-band 62
3.2.2.3 The D and D^* modes 65
3.3 Atomic Force Microscopy (AFM) 65
3.4 Summary 71
3.5 References 71
CHAPTER 4 77
DISPERSION OF SWNTS IN CHLORINATED AROMATIC SOLVENTS 77
4.1 Introduction 77
4.2 Experimental 80

4.2.1 Sonication time 81
4.2.2 SWNT-solvent dispersion preparation 81
4.2.3 Optical absorption spectroscopy 82
4.3 Results and discussion 82
4.4 Summary 91
4.5 References 92
CHAPTER 5 95
SOLVENT SOLUBILITY PARAMETERS AND SWNTS 95
5.1 Introduction 95
5.2 Experimental Section 98
5.3 Results and Discussion 99
5.4 Summary 105
5.5 References 106
CHAPTER 6 108
STRUCTURAL ASSIGNMENT OF SWNTS 108
6.1 Introduction 108
6.2 Experimental 110
6.3 Results and discussions 111
6.4 Summary 124
6.5 References 125
CHAPTER 7 129
SOLVENT PARAMTERS AND DISPERSION LIMIT OF SWNTS 129
7.1 Introduction 129
7.2 Experimental Section 131
7.3 Results and Discussion 133

7.4 Summary 144
7.5 References 145
CHAPTER 8 147
ULTRASOUND-ASSISTED SWNT DISPERSION IN SOLVENTS 147
8.1 Introduction 147
8.2 Experimental Section 150
8.3 Results and Discussion 152
8.4 Summary 163
8.5 References 163
CHAPTER 9 167
SUMMARY 167
9.1 Summary of the results 167
9.2 Future Prospect 171
9.3 References 173
LIST OF PUBLICATIONS AND PRESENTATIONS 174

TABLE OF FIGURES

Figure 1.1 Conceptual diagram of single-walled carbon nanotube and multiwalled carbon nanotube 1

Figure 1.2 TEM image of SWNT bundles generated from alcohol CCVD method 3

Figure 2.1 Rolling of graphene to form a SWNT 15

Figure 2.2 Structure of a capped SWNT 16

Figure 2.3 Construction of a carbon nanotube from a single graphene sheet 17

Figure 2.4 Classification of SWNTs and their chiral parameters 17

Figure 2.5 Electrical properties of different materials 19

Figure 2. 6 Energy band structure in graphene 20

Figure 2. 7 Schematic diagram of electronic density of states for (a) metallic, (b) semiconducting SWNTs 21

Figure 2.8 Schematic representation of oven laser-vapourisation apparatus used at Rice University 27

Figure 2. 9 Layout of CO flow-tube reactor 29

Figure 3.1 Ground state (E_0) and two excited states (E_1, E_2) of a molecule (vibrational and rotational levels are not shown) 46

Figure 3.2 Schematic of absorption when light passes through a sample, adapted from 47

Figure 3.3 Schematic of Rayleigh scattering and Mie scattering.....48

Figure 3.4 Perkin Elmer Lambda 900 UV-Vis-NIR Spectrometer.....49

Figure 3.5 Schematic set-up of double beam UV-Vis-NIR spectrometer 50

Figure 3.6 Schematic of the different mode of absorbance spectrometer: (a) normal chamber, (b) integrating sphere 51

Figure 3.7 Typical optical spectrum of HiPco SWNTs dispersed in *m*-DCB....53

Figure 3.8 Absorption spectra of SWNTs in *o*-DCB at a concentration of 0.02 mg/ml 55

Figure 3.9 Energy level diagrams of the states involved in the Raman signal 57

Figure 3.10 Horiba Jobin Yvon LabRAM HR 800 Raman spectrometer 58

Figure 3.11 Raman spectrum of bundled HiPco SWNTs on quartz substrate excited at 1.88ev. 59

Figure 3.12 Schematic representation of the atomic vibrations for RBM and G-line 60

Figure 3.13 Kataura plot. Semiconducting (open circle), Metallic (filled circle). Four horizontal lines indicate the laser energies. Diameter range of the HiPco SWNTs is indicated by the two vertical lines. 61

Figure 3.14 RBM frequencies (normalised to the most intense peak) of bundled HiPco SWNTs dispersed on quartz substrate at different excitation energies. .62

Figure 3.15 Diamter dependence of the G^- frequency in metallic and semi-conducting SWNTs. 64

Figure 3.16 G-band frequencies (normalised to G^+) of bundled HiPco SWNTs disposed on quartz substrate at different excitation energies and the corresponding D band. 64

Figure 3.17 Working principle of AFM 66

Figure 3.18 The region where the contact and non contact mode can be operated. 67

Figure 3.19 Tapping mode of AFM 69

Figure 3.20 MFP-3D-BIO atomic force microscope (Asylum Research) 70

Figure 3.21 AFM images of bundled (a) and dispersed (b) SWNTs.....70

Figure 4.1 Molecular-modelling schematic illustrating the interaction of a SWNT with o-DCB, The interactions involve π-orbital (black arrow) and dipole–dipole (red arrow) interactions (the line width indicates the degree of strength). Color coding of atoms: C, gray; H, white; Cl, green.....78

Figure 4.2 Molecular structures of the chlorinated aromatic solvents 80

Figure 4.3 3-D surface structures of the solvents. Colour coding of atoms: C, gray; H, white, Cl, green. 80

Figure 4.4 (a) Picture of 0.04mg/ml SWNT/o-DCB dispersions with different sonication time, left to right, 20 s, 40 s, 60 s, 80 s, 100 s, 120 s,140 s and 160 s. (b) Sonication time dependence of the absorption of SWNT/o-DCB dispersions (supernatant) at 660nm.....83

Figure 4.5 (a) Plot of the absorbance at 660nm in SWNT/o-DCB dispersion versus concentration. (b) Concentration dependence of the absorbance in the integrating spheres (data from Figure 4.5(a)). 85

Figure 4.6 Plot of the absorbance at 660nm versus concentration in (a) MCB and (b) *m*-DCB dispersion. 86

Figure 4.7 Scattering fraction and aggregation mass fraction in different solvents.....88

Figure 5.1 Molecular structures of the solvents.....96

Figure 5.2 Concentration dependence of the absorbance of SWNT dispersions in various solvents, (a) in the normal chamber, (b) in the integrating sphere..100

Figure 5.3 (a) Relationship between the total Extinction coefficient of SWNTs in each solvent with the Hildebrand solubility parameters; (b) Relationship

between the Absorption coefficient of SWNTs in each solvent with the Hildebrand solubility parameters. 101

Figure 5.4 Extinction due to scattering in *o*-DCB and DCE dispersions 103

Figure 5.5 (a) total Extinction coefficient *vs* dispersion component (δ_D) ; (b) Absorption coefficient *vs* dispersion component (δ_D) ; (c) total Extinction coefficient *vs* Polar component (δ_P) ; (d) Absorption coefficient *vs* Polar component (δ_P) ; (e) total Extinction coefficient *vs* Hydrogen bonding component (δ_H) ; (f) Absorption coefficient *vs* Hydrogen bonding component (δ_H) 104

Figure 6.1 RBM frequencies (normalised to the most intense peak) of bundled HiPco SWNTs disposed on quartz substrate at different excitation energies and the corresponding G-band (normalized to the G^+ peak) 113

Figure 6.2 Radial breathing modes obtained from the HiPco SWNT bundles with 2.62eV excitation energy. The peaks are fitted by 12 Gauss/Lorentz curves. 113

Figure 6.3 Observed RBM frequencies at 2.62 eV as a function of inverse diameter. The filled circles fall into the best linear fitting line (the dashed line) with smallest error. A = 213.7 ± 0.6 cm^{-1} ·nm and B = 22.7 ± 0.7 cm^{-1}. 116

Figure 6.4 Locations of the assigned nanotubes within the Kataura plot for the different laser energies. 118

Figure 6.5 Energy differences between E_{ii} and E_{laser} (ΔE) as a function of nanotube diameter. 119

Figure 6.6 Histogram of the diameter distribution from the assignment results for four laser energies 119

Figure 6.7 Observed RBM frequencies as a function of inverse possible diameters at all laser lines. The dashed line is a linear fitting of the points from

2.62 eV, 1.88 eV and 1.58 eV, A= 213.1 ± 1.3 cm^{-1} · nm and B = 23.7 ± 1.4 cm^{-1}. 120

Figure 6.8 Raman spectra of Pristine SWNTs and SWNTs dispersed in DMF at 0.001 mg/ml. The insets are the corresponding RBMs with curve fitting. (a) 2.33 eV, (b) 1.88 eV. 122

Figure 6.9 Histogram of occurrence of identified SWNTs in DMF and *o*-DCB solutions. (a) 1.88 eV, (b) 2.33 eV. 123

Figure 7.1 Fraction of the nanotube aggregates in MCB, TCB and DMF dispersions as a function of prepared concentration. Two samples of SWNT/DMF dispersions with concentration of 0.0375 mg/ml (A) and 0.0067 mg/ml (B) and one sample of SWNT/TCB dispersion at concentration of 0.00282 mg/ml (C) were studied by AFM. 134

Figure 7.2 AFM images of SWNT/DMF dispersions after centrifugation, (a) 0.0375 mg/ml, (b) 0.0067 mg/ml. 134

Figure 7.3 Position of the employed solvents in Hansen parameter space, the size of the sphere indicates the ease of dispersion of SWNTs (dispersion limit) in the corresponding solvent. For the dispersion limit below 0.001 mg/ml, 0.0005 mg/ml is used to indicate the sphere size. 136

Figure 7.4 Absorption coefficients and Dispersion limits as a function of Hildebrand parameter. 136

Figure 7.5 Absorption coefficients and Dispersion limits *vs* (a) dispersion component (δ_D), (b) polar component (δ_P) and (c) hydrogen-bonding component (δ_H). 138

Figure 7.6 AFM image of DMF dispersion at ~ 0.003 mg/ml precentrifugation. 140

Figure 7.7 Aggregation fractions of SWNTs in DMF at different sonication time (volume 5ml, without temperature control). 141
Figure 7.8 I_D/I_{G+} ratio as a function of sonication time for SWNT/DMF 142
Figure 7.9 AFM images of SWNTs dispersed in TCB at 0.00282 mg/ml. 144
Figure 8.1 Absorbance of 0.04 mg/ml SWNTs in *o*-DCB and DMF after centrifugation as a function of sonication time (t). (The vertical Blue line indicates the sonication time applied in previous studies [8, 21], Chapter 4. The Red and Black lines are guide to the eye).. 154
Figure 8.2 Absorbance of 0.04mg/ml DMF and *o*-DCB dispersions after centrifuge as a function of sonicator output power (The vertical line indicates the output power used in previous studies [8, 21], Chapter 4) 154
Figure 8.3 Aggregation fractions of SWNTs below the dispersion limits in each solvent as a function of the solvent vapour pressure. The dashed line is a fit of an exponential dependence of (1- χ_{agg}) on the solvent vapour pressure. 156
Figure 8.4 Aggregation fractions of SWNTs below the dispersion limits in each solvent as a function of the solvent viscosity. The dashed line is a guide to the eye 157
Figure 8.5 Aggregation fractions of SWNTs below the debundling solvents in each solvent as a function of the solvent surface tension. The dashed line is a guide to the eye. 158
Figure 8.6 Aggregation fractions below the dispersion limit in each solvent as a function of the solvent density. The dashed line is a guide to the eye. 159
Figure 8.7 Aggregation fractions below the dispersion limit in each solvent as a function of the solvents molecular weight. The dashed line is a guide to the eye 160

Figure 8.8 Absorbance and I_D/I_{G+} ratio as a function of sonication time. Filled squares: absorbance of DMF solutions; Filled circles: absorbance of *o*-DCB solutions; Open squares: I_D/I_{G+} ratios for DMF solutions; Open circles: I_D/I_{G+} ratios for *o*-DCB solutions; the dashed lines indicate a √t dependence of the I_D/I_{G+} ratio.....161

Figure 8.9 Absorbance and I_D/I_{G+} ratio as a function of sonicator output power. Filled squares: absorbance of DMF solutions; Filled circles: absorbance of *o*-DCB solutions; Open squares: I_D/I_{G+} ratios for DMF solutions; Open circles: I_D/I_{G+} ratios for *o*-DCB solutions; the dashed lines indicate a √t dependence of the I_D/I_{G+} ratio.....162

Table 2.1 Summary of the contemporary SWNTs synthesis techniques and product description 25

Table 5.1 The Hildebrand solubility parameter and Hansen solubility parameters of the solvents and the total Extinction coefficient and Absorption coefficient of SWNTs in different solvents.....101

Table 6.1 Experimental ω_{RBM} at 2.62 eV and calculated diameter range d_1 (A = 216, B = 17) and d_2 (A = 234, B = 10), electronic property (M: metallic; S: semiconducting) together with the possible diameters (ω_{RBM}: mean value from 50 spectra).....115

Table 6.2 RBM shifts and the corresponding structure assignments (ω_{RBM}: Mean value from 50 spectra) 117

Table 7.1 The Hildebrand solubility parameter and Hansen solubility parameters of the solvents and the dispersion limits (D_L) of SWNTs in different solvents, together with the aggregation fraction (χ_{agg}) below dispersion limit in each solvent and absorption coefficient. 135

Table 8.1 Different sonication conditions for dispersing SWNTs in liquid 148

Table 8.2 The dispersion limits of SWNTs and aggregation fraction below D_L in different solvents together with the solvents physical parameters (all the samples get 2 mins sonication)..... 153

CHAPTER 1
INTRODUCTION

1.1 Research background

Carbon Nanotubes, as the name suggests, are cylindrical nanostructures consisting entirely of carbon. Within the developing field of nanotechnology, they are proposed as a material of significant applications potential, due to their reported unique physical properties [1].

Carbon nanotubes can be classified into two types: Single-walled carbon nanotube (SWNTs), double walled carbon nanotubes (DWNTs) and multi-walled carbon nanotubes (MWNTs). Figure 1.1 shows a conceptual diagram of SWNT and MWNT.

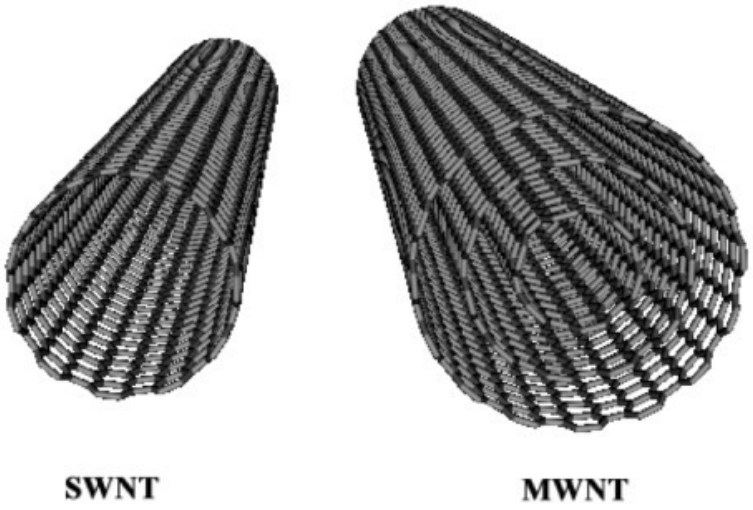

Figure 1.1 Conceptual diagram of SWNT and MWNT.

Most SWNTs have a diameter in a range of 1-2 nm, depending on the synthesis method, with the length between 0.2 and 5 μm [2]. The length-to-diameter ratios of SWNTs normally exceed 10,000, because of which SWNTs are considered to be an ideal one-dimensional material. Ultra long SWNTs have been constructed which have length-to-diameter ratios up to 132,000,000:1 [3]. MWNTs consist of more than one concentrically rolled layer of graphite, and have diameters which vary from 2-100 nm [2, 4] depending on the number of layers. The interlayer distance in multi-walled nanotubes is close to the distance between graphene layers in graphite, approximately 0.335 nm [5].

Based on the unique structure of the parent material, graphene, carbon nanotubes are proposed to have novel properties that make them potentially useful in many fields. These applications include high performance nanocomposites which are conductive and high strength in nature [6, 7], nano-sized semiconductor devices [8], nano-probes [9, 10], energy conversion devices [11-14], sensors [15, 16], field emission displays [17, 18], radiation sources [19, 20] and drug delivery systems [21-23]. However these applications still remain in the “potential” stage. Bulk availability of high quality, low cost samples and processing difficulties are the main obstacles in expanding the technological applications of carbon nanotubes.

As a member of the fullerene structural family, the carbon atoms in carbon nanotubes are sp^2-bonded. Due to the extended π electron system, the surface electrons are highly polarizable, and so are subject to large attractive inter-tubular van der Waals forces [24]. Thus, as-produced SWNT samples are obtained in bundled form and are difficult to separate. The size of bundles has

been shown to be determined by distortions of van der Waals bonds between nanotubes in the vicinity of a catalytic particle and the extent of nanotube bending in the bundle [25]. The typical bundle size of as-produced SWNTs varies between nanometers to microns. Figure 1.2 shows a Transmission Electron Microscopy (TEM) image of a nanotube bundle. It has been seen that an individual nanotube can be bent and tangled within a bundle, increasing the difficulty of exfoliation and debundling of SWNTs aggregates.

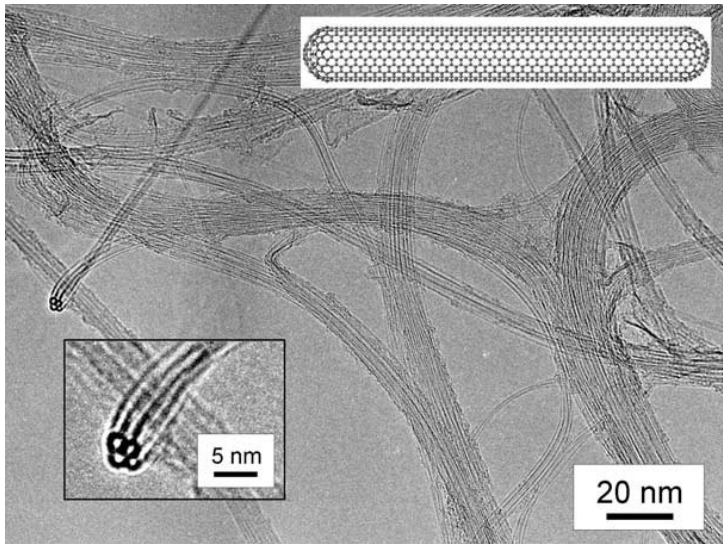

Figure 1.2 TEM image of SWNT bundles generated from alcohol CCVD method [26].

Although the chemical reactivity of nanotubes, compared with graphene, is enhanced as a result of the surface curvature, SWNTs are still relatively inert and insoluble in either water or common organic solvents, which is a significant obstacle to the effective processing of SWNTs. With the aid of surfactant [27, 28], organic molecules [29, 30] or small biomolecules [31, 32], SWNTs can be dispersed in aqueous solution. Conjugated polymers and small molecules can

also be employed in organic solvents [33, 34]. Covalent side-wall functionalization is another effective method to improve the solubility and stability of SWNTs in solution [35]. However, the introduction of a third component and the modification of the side wall would affect the pristine properties of the tubes which should be avoided. Over the years, unremitting effort has been devoted, aimed at finding appropriate media to solubilize pristine nanotubes. Various solvents have been investigated in order to solubilise and disperse SWNT aggregates. Non hydrogen-bonding Lewis bases, such as dimethylformamide (DMF), N-methylpyrrolidone (NMP) and hexamethylphosphoramide (HMPA), with high electron pair donicity and low hydrogen-bonding parameters have demonstrated the ability to readily form stable dispersions of SWNT produced by different techniques [36-38]. However the high electron pair donicity alone has proven to be insufficient as dimethylsulfoxide (DMSO) is not an effective solvent for SWNTs although it contains three lone pairs [39]. A systematic study of the efficacy of a series of amide solvents to disperse as-produced and purified laser-generated SWNTs suggested that the favorable interaction between SWNTs and alkyl amide solvents is attributed to the highly polar π system and optimal geometries (appropriate bond lengths and bond angles) of the solvent structures [40]. Ortho-dichlorobenzene (*o*-DCB) and monochlorobenzene (MCB) have also been demonstrated to be effective solvents for SWNTs [38, 41]. The high solubility of SWNTs in these solvents was attributed to π - π stacking due to the similarity of the aromatic solvent molecules and carbon nanotube side wall [41]. However, this concept is somehow undermined by the poor solubility of SWNTs in toluene [39], since it also contains a phenyl ring. It was also reported that in

o-DCB dispersions, sonication caused the decomposition and polymerization of *o*-DCB and the sonopolymer coated on the tubes was proposed to contribute to the stabilization of SWNT in *o*-DCB suspension [42]. A theoretical study indicated that the interaction between *o*-DCB and SWNTs surface was enhanced when there were defects on the side wall, which would suggest that the high solubility of SWNTs in *o*-DCB is probably due to the destruction of nanotube surface during sample preparation [43].

1.2 Research objectives

Although substantial effort has been devoted to the purification and exfoliation of as-produced SWNTs, the successes are limited. As discussed in Section 1.1, although some solvents show some ability of solubilising SWNTs aggregates, no agreement on the underlying mechanisms has been reached. Therefore, a systematic study of the solubility of SWNTs in different solvents in order to determine the parameters which govern the debundling and solubilisation process is required in order to optimise processing techniques for applications.

The main objectives of this thesis include:

(1) To undertake a systematic study of the efficiency of systematically structurally varied chlorinated aromatic solvents in dispersing as-produced SWNTs.

(2) To extend the range of solvents and gain an in-depth understanding of the mechanism of interaction between SWNTs and solvents, establishing the solvents parameters which affect the solubility of SWNTs.

(3) To investigate selective debundling of metallic or semiconducting SWNTs by different solvents.

(4) To investigate the effect of sonication parameters and solvent properties during ultrasonic debundling of SWNTs.

1.3 Thesis outline

Chapter 2 gives a brief introduction to the properties of SWNTs, including their structural, electrical and mechanical characteristics. This chapter reviews the synthesis techniques of SWNTs developed over the last two decades, and the problems hindering the industrial applications of the as-produced material. Commonly employed purification and dispersing techniques are also described.

Chapter 3 outlines the characterization techniques employed in this work, including UV-Vis-NIR spectroscopy, resonant Raman spectroscopy and Atomic Force Microscopy. The instrument set up and working principles are discussed with the aid of schematic illustrations.

Chapter 4 is adapted from "**Effects of chlorinated aromatic solvents on the dispersion of HiPco SWNTs**" (Qiaohuan Cheng, Sourabhi Debnath, Elizabeth Gregan, Hugh J. Byrne), published in ***Physica Status Solidi B 2008, 245, 1947***. In this chapter, the capability of a series of chlorinated aromatic solvents, including monochlorobenzene (MCB), *ortho*-dichlorobenzene (*o*-DCB), *meta*-dichlorobenzene (*m*-DCB) and 1, 2, 4-trichlorobenzene (TCB), to disperse and solubilise HiPco SWNTs is evaluated. The variation of the dispersiblity of

SWNTs in the examined solvents indicates that the similarity in structure between SWNTs and the aromatic solvent molecules is not the dominant factor of obtaining stable high concentration SWNT dispersions.

Chapter 5 is adapted from "Effect of Solvent Solubility Parameters on the Dispersion of Single-Walled Carbon Nanotubes" (Qiaohuan Cheng, Sourabhi Debnath, Elizabeth Gregan, Hugh J. Byrne), published in ***Journal of Physical Chemistry C 2008, 112, 20154***. In order to further investigate the effect of solvent solubility parameters on the dispersion of SWNTs, a further 4 solvents, toluene, chloroform, 1, 2-dichloroethane (DCE) and dimethylformamide (DMF), previously reported as dispersion agents for SWNTs, are included. The abilities of the solvents to solubilise and disperse SWNTs are compared in terms of solvent solubility parameters, including Hildebrand and Hansen parameters.

Chapter 6 is adapted from "Vibrational mode assignments for bundled single-wall carbon nanotubes using Raman spectroscopy at different excitation energies" (Qiaohuan Cheng, Sourabhi Debnath, Elizabeth Gregan, Hugh J. Byrne) submitted to ***Applied Physics A, Jan.2010***. Due to the different linear correlations of extinction/absorption coefficients as a function of solvent solubility parameters inferred in Chapter 5 for the classes of chlorinated aromatic solvents and "other" solvents, a Raman study of the SWNT/DMF and SWNT/*o*-DCB samples, extremes of the observed behaviour from the two different classes, was conducted. Prior to this, an entire Raman study of the nanotube sample used in this work was carried out. The structural assignments of the bundled SWNTs were carried out for different excitation laser energies using a novel fitting technique.

Chapter 7 is adapted from "**Systematic study of the dispersion of SWNTs in organic solvents**" (Qiaohuan Cheng, Sourabhi Debnath, Luke O'Neill, Theresa G. Hedderman, Elizabeth Gregan, Hugh J. Byrne), published in ***Journal of Physical Chemistry C 2010, 114, 4857***. In this chapter, the range of examined solvents was further extended. The Dispersion limit, at which concentration the aggregation ceases to dominate the dispersion, together with the absorption coefficient, were studied as a function of Hildebrand solubility parameters and Hansen solubility parameters.

Chapter 8 is adapted from "Ultrasound-assisted SWNTs dispersion: effects of sonication parameters and solvent properties" (Qiaohuan Cheng, Sourabhi Debnath, Elizabeth Gregan, Hugh J. Byrne), published in ***Journal of Physical Chemistry C 2010, 114, 8821***. In the systematic study of the dispersion limit of SWNTs in different solvents, it was surprising to find that the aggregation fraction below the dispersion limit in each solvent varies significantly and that there is no correlation with the dispersion limit of SWNTs in the corresponding solvent. This variation of aggregation fractions is shown to derive from the sonication procedure. A systematic study of the relationship between the solubilisation process and the solvent sonication parameters is described. The correlations observed indicate that it is these solvent parameters which govern the dispersion and solubilisation of SWNTs.

Chapter 9 provides a summary, conclusion and outlook based on this project.

1.4 References

1. Baughman, R.H.; Zakhidov, A.A.; de Heer, W.A. Carbon nanotubes - the route toward applications. Science, 2002, **297**, 787-792.
2. Ajayan, P.M. Nanotubes from carbon. Chemical Reviews, 1999, **99**, 1787-1799.
3. Wang, X.S.; Li, Q.Q.; Xie, J.; Jin, Z.; Wang, J.Y.; Li, Y.; Jiang, K.L.; Fan, S.S. Fabrication of Ultralong and Electrically Uniform Single-Walled Carbon Nanotubes on Clean Substrates. Nano Letters, 2009, **9**, 3137-3141.
4. Delzeit, L.; McAninch, I.; Cruden, B.A.; Hash, D.; Chen, B.; Han, J.; Meyyappan, M. Growth of multiwall carbon nanotubes in an inductively coupled plasma reactor. Journal of Applied Physics, 2002, **91**, 6027-6033.
5. Palser, A.H.R. Interlayer interactions in graphite and carbon nanotubes. Physical Chemistry Chemical Physics, 1999, **1**, 4459-4464.
6. Dalton, A.B.; Collins, S.; Munoz, E.; Razal, J.M.; Ebron, V.H.; Ferraris, J.P.; Coleman, J.N.; Kim, B.G.; Baughman, R.H. Super-tough carbon-nanotube fibres - These extraordinary composite fibres can be woven into electronic textiles. Nature, 2003, **423**, 703-703.
7. Wang, W.; Fernando, K.A.S.; Lin, Y.; Meziani, M.J.; Veca, L.M.; Cao, L.; Zhang, P.; Kimani, M.M.; Sun, Y.P. Metallic single-walled carbon nanotubes for conductive nanocomposites. Journal of the American Chemical Society, 2008, **130**, 1415-1419.

8. McEuen, P.L.; Fuhrer, M.S.; Park, H.K. Single-walled carbon nanotube electronics. Ieee Transactions on Nanotechnology, 2002, **1**, 78-85.

9. Cheung, C.L.; Hafner, J.H.; Lieber, C.M. Carbon nanotube atomic force microscopy tips: Direct growth by chemical vapor deposition and application to high-resolution imaging. Proceedings of the National Academy of Sciences of the United States of America, 2000, **97**, 3809-3813.

10. Nguyen, C.V.; Ye, Q.; Meyyappan, M. Carbon nanotube tips for scanning probe microscopy: fabrication and high aspect ratio nanometrology. Measurement Science & Technology, 2005, **16**, 2138-2146.

11. Pasquier, A.D.; Unalan, H.E.; Kanwal, A.; Miller, S.; Chhowalla, M. Conducting and transparent single-wall carbon nanotube electrodes for polymer-fullerene solar cells. Applied Physics Letters, 2005, **87**, 203511.

12. Rowell, M.W.; Topinka, M.A.; McGehee, M.D.; Prall, H.J.; Dennler, G.; Sariciftci, N.S.; Hu, L.B.; Gruner, G. Organic solar cells with carbon nanotube network electrodes. Applied Physics Letters, 2006, **88**, 233506.

13. Suzuki, K.; Yamaguchi, M.; Kumagai, M.; Yanagida, S. Application of carbon nanotubes to counter electrodes of dye-sensitized solar cells. Chemistry Letters, 2003, **32**, 28-29.

14. Gabor, N.M.; Zhong, Z.H.; Bosnick, K.; Park, J.; McEuen, P.L. Extremely Efficient Multiple Electron-Hole Pair Generation in Carbon Nanotube Photodiodes. Science, 2009, **325**, 1367-1371.

15. Dai, L.M.; Soundarrajan, P.; Kim, T. Sensors and sensor arrays based on conjugated polymers and carbon nanotubes. Pure and Applied Chemistry, 2002, **74**, 1753-1772.

16. Li, J.; Lu, Y.J.; Ye, Q.; Cinke, M.; Han, J.; Meyyappan, M. Carbon nanotube sensors for gas and organic vapor detection. Nano Letters, 2003, **3**, 929-933.

17. Deheer, W.A.; Chatelain, A.; Ugarte, D. A Carbon Nanotube Field-Emission Electron Source. Science, 1995, **270**, 1179-1180.

18. Lim, S.C.; Lee, D.S.; Choi, H.K.; Lee, I.H.; Lee, Y.H. Field emission of carbon-nanotube point electron source. Diamond and Related Materials, 2009, **18**, 1435-1439.

19. Boul, P.J.; Turner, K.; Li, J.; Pulikkathara, M.X.; Dwivedi, R.C.; Sosa, E.D.; Lu, Y.J.; Kuznetsov, O.V.; Moloney, P.; Wilkins, R.; O'Rourke, M.J.; Kliabashesku, V.N.; Arepalli, S.; Yowell, L. Single Wall Carbon Nanotube Response to Proton Radiation. Journal of Physical Chemistry C, 2009, **113**, 14467-14473.

20. Tang, X.W.; Yang, Y.; Kim, W.; Wang, Q.; Qi, P.F.; Dai, H.J.; Xing, L. Measurement of ionizing radiation using carbon nanotube field effect transistor. Physics in Medicine and Biology, 2005, **50**, N23-N31.

21. Bianco, A.; Kostarelos, K.; Prato, M. Applications of carbon nanotubes in drug delivery. Current Opinion in Chemical Biology, 2005, **9**, 674-679.

22. Li, S.S.; He, H.; Jiao, Q.C.; Chuong, P.H. Applications of Carbon Nanotubes in Drug and Gene Delivery. Progress in Chemistry, 2008, **20**, 1798-1803.

23. Liu, Z.; Chen, K.; Davis, C.; Sherlock, S.; Cao, Q.Z.; Chen, X.Y.; Dai, H.J. Drug delivery with carbon nanotubes for in vivo cancer treatment. Cancer Research, 2008, **68**, 6652-6660.

24. Henrard, L.; Hernandez, E.; Bernier, P.; Rubio, A. van der Waals interaction in nanotube bundles: Consequences on vibrational modes. Physical Review B, 1999, **60**, 8521-8524.

25. Alekseev, N.I.; Charykov, N.A. The characteristic size of carbon nanotube bundles. Russian Journal of Physical Chemistry A, 2009, **83**, 1176-1181.

26. Maruyama, S. CVD Generation of Single-Walled Carbon Nanotubes from Alcohol. Catalysts & Catalysis, 2005, **47**, 207-212.

27. Islam, M.F.; Rojas, E.; Bergey, D.M.; Johnson, A.T.; Yodh, A.G. High weight fraction surfactant solubilization of single-wall carbon nanotubes in water. Nano Letters, 2003, **3**, 269-273.

28. Moore, V.C.; Strano, M.S.; Haroz, E.H.; Hauge, R.H.; Smalley, R.E.; Schmidt, J.; Talmon, Y. Individually suspended single-walled carbon nanotubes in various surfactants. Nano Letters, 2003, **3**, 1379-1382.

29. Hu, C.G.; Chen, Z.L.; Shen, A.G.; Shen, X.C.; Li, H.; Hu, S.S. Water-soluble single-walled carbon nanotubes via noncovalent functionalization by a rigid, planar and conjugated diazo dye. Carbon, 2006, **44**, 428-434.

30. O'Connell, M.J.; Boul, P.; Ericson, L.M.; Huffman, C.; Wang, Y.H.; Haroz, E.; Kuper, C.; Tour, J.; Ausman, K.D.; Smalley, R.E. Reversible water-solubilization of single-walled carbon nanotubes by polymer wrapping. Chemical Physics Letters, 2001, **342**, 265-271.

31. Nakashima, N.; Okuzono, S.; Murakami, H.; Nakai, T.; Yoshikawa, K. DNA dissolves single-walled carbon nanotubes in water. Chemistry Letters, 2003, **32**, 456-457.

32. Zheng, M.; Jagota, A.; Semke, E.D.; Diner, B.A.; Mclean, R.S.; Lustig, S.R.; Richardson, R.E.; Tassi, N.G. DNA-assisted dispersion and separation of carbon nanotubes. Nature Materials, 2003, **2**, 338-342.

33. Curran, S.A.; Ajayan, P.M.; Blau, W.J.; Carroll, D.L.; Coleman, J.N.; Dalton, A.B.; Davey, A.P.; Drury, A.; McCarthy, B.; Maier, S.; Strevens, A. A composite from poly(m-phenylenevinylene-co-2,5-dioctoxy-p-phenylenevinylene) and carbon nanotubes: A novel material for molecular optoelectronics. Advanced Materials, 1998, **10**, 1091-1093.

34. Hedderman, T.G.; Keogh, S.M.; Chambers, G.; Byrne, H.J. Solubilization of SWNTs with organic dye molecules. Journal of Physical Chemistry B, 2004, **108**, 18860-18865.

35. Tasis, D.; Tagmatarchis, N.; Georgakilas, V.; Prato, M. Soluble carbon nanotubes. Chemistry-a European Journal, 2003, **9**, 4001-4008.

36. Ausman, K.D.; Piner, R.; Lourie, O.; Ruoff, R.S.; Korobov, M. Organic solvent dispersions of single-walled carbon nanotubes: Toward solutions of pristine nanotubes. Journal of Physical Chemistry B, 2000, **104**, 8911-8915.

37. Furtado, C.A.; Kim, U.J.; Gutierrez, H.R.; Pan, L.; Dickey, E.C.; Eklund, P.C. Debundling and dissolution of single-walled carbon nanotubes in amide solvents. Journal of the American Chemical Society, 2004, **126**, 6095-6105.

38. Bahr, J.L.; Mickelson, E.T.; Bronikowski, M.J.; Smalley, R.E.; Tour, J.M. Dissolution of small diameter single-wall carbon nanotubes in organic solvents? Chemical Communications, 2001193-194.

39. Giordani, S.; Bergin, S.D.; Nicolosi, V.; Lebedkin, S.; Kappes, M.M.; Blau, W.J.; Coleman, J.N. Debundling of single-walled nanotubes by dilution: Observation of large populations of individual nanotubes in amide solvent dispersions. Journal of Physical Chemistry B, 2006, **110**, 15708-15718.

40. Landi, B.J.; Ruf, H.J.; Worman, J.J.; Raffaelle, R.P. Effects of alkyl amide solvents on the dispersion of single-wall carbon nanotubes. Journal of Physical Chemistry B, 2004, **108**, 17089-17095.

41. Kim, D.S.; Nepal, D.; Geckeler, K.E. Individualization of single-walled carbon nanotubes: Is the solvent important? Small, 2005, **1**, 1117-1124.

42. Niyogi, S.; Hamon, M.A.; Perea, D.E.; Kang, C.B.; Zhao, B.; Pal, S.K.; Wyant, A.E.; Itkis, M.E.; Haddon, R.C. Ultrasonic dispersions of single-walled carbon nanotubes. Journal of Physical Chemistry B, 2003, **107**, 8799-8804.

43. Fagan, S.B.; Souza, A.G.; Lima, J.O.G.; Mendes, J.; Ferreira, O.P.; Mazali, I.O.; Alves, O.L.; Dresselhaus, M.S. 1,2-dichlorobenzene interacting with carbon nanotubes. Nano Letters, 2004, **4**, 1285-1288.

CHAPTER 2
SINGLE WALLED CARBON NANOTUBES

2.1 What are Single Walled Carbon Nanotubes?

A Single Walled Carbon Nanotube (SWNT) is a one-atom thick sheet of graphite (called graphene) rolled up into a seamless cylinder capped by semi-fullerene type caps at both ends, with a diameter typically in the range of 1-2 nm [1]. Figure 2.1 shows the rolling of graphene to form a Single Walled Carbon Nanotube, and the structure of a capped SWNT is shown in Figure 2.2. The discovery of SWNTs was reported in 1993, by the International Business Machines (IBM) and Nippon Electric Company (NEC) groups, in back to back papers published in ***Nature*** [2, 3].

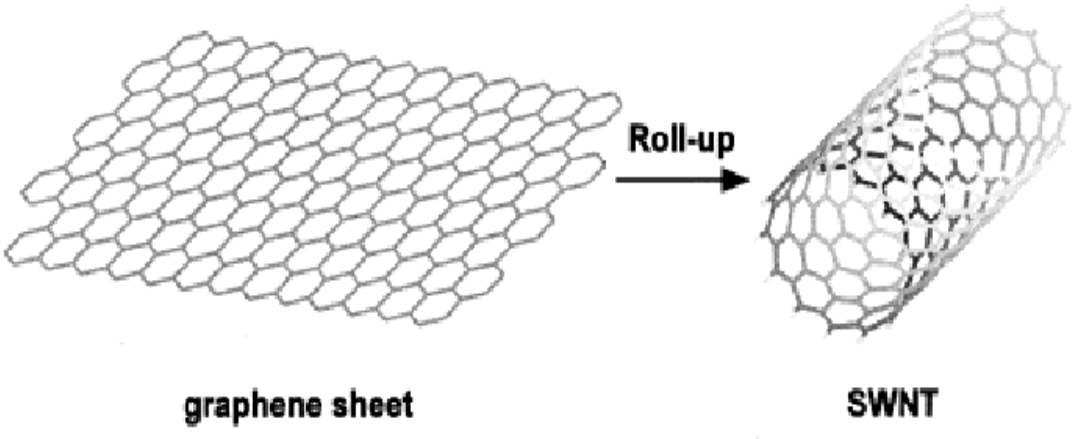

Figure 2.1 Rolling of graphene to form a SWNT [4]

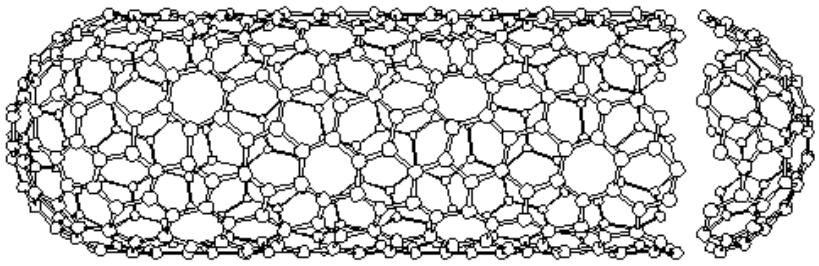

Figure 2.2 Structure of a capped SWNT [1]

Based on the difference of structures which result from different wrapping angles, SWNTs can be divided into three types, *zigzag*, *armchair* and *chiral*. As shown in Figure 2.3, if two sites are overlapped by wrapping, the wrapping vector $\boldsymbol{C}$, which defines the relative location of the two sites, is specified by a pair of integers $(n,\ m)$ that relate $\boldsymbol{C}$ to the two unit vectors $\boldsymbol{a_1}$ and $\boldsymbol{a_2}$, the relationship between these parameters being given by

$$C = na_1 + ma_2 \qquad \text{Equation 2.1 [5-8]}$$

When $n = m$ and $\theta = 30°$, and an '*armchair*' tube will be constructed. However, in the case when $m = 0$ and $\theta = 0°$, and the tube formed is a '*zigzag*' tube, shown in Figure 2.3. Both armchair and zigzag SWNTs are 'a*chiral*' in that they are superimposable on their mirror image. All other tubes are of the '*chiral*' type and have a wrapping angle θ with value $0° < \theta < 30°$ [5-8]. The classification of SWNTs is shown in Figure 2.4.

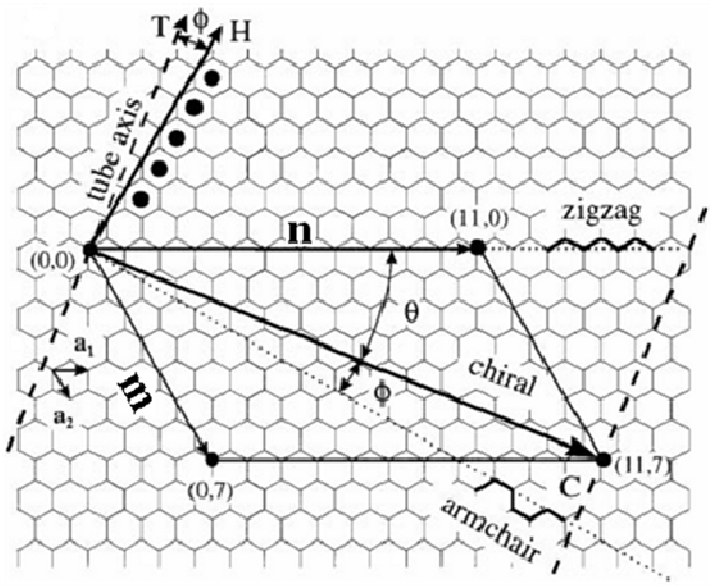

Figure 2.3 Construction of a carbon nanotube from a single graphene sheet [6]

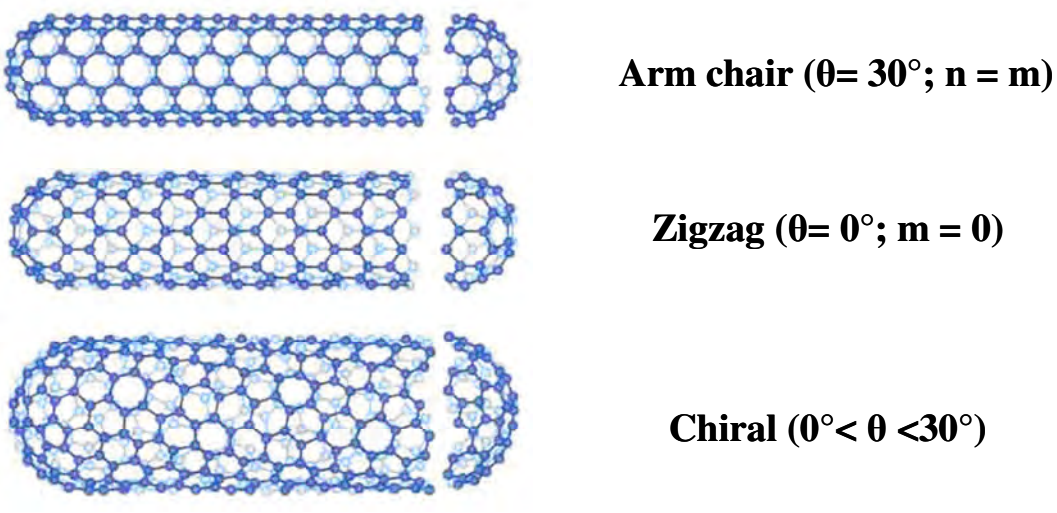

Figure 2.4 Classification of SWNTs and their chiral parameters [1]

For a carbon nanotube defined by the index (n, m), the diameter, d, and the chiral angle, θ, are given by Equations 2.2 and 2.3, where b is the distance between neighboring carbon atoms in the flat sheet [8]. Normally either 0.142 nm [9] or 0.144 nm [10] have been used in literature for calculations. In this study, 0.144 nm was chosen for all the calculations.

$$d = \sqrt{3(n^2 + m^2 + mn)}b / \pi \qquad \text{Equation 2.2 [9]}$$

$$\tan\theta = \sqrt{3}m/(2n+m) \qquad \text{Equation 2.3 [9]}$$

The chirality of the carbon nanotube has significant implications on the material properties. In particular, tube chirality is known to have a strong impact on the electronic properties of the carbon nanotubes. Theoretical calculations [11] have predicted that when $(n - m)$ mod 3 = 0, the tubes are metallic, otherwise the tubes are semiconducting when $(n - m)$ mod 3 = 1 or 2, with an energy gap of the order of ~ 0.5 eV [6]. If the distribution of the structural vector in the tubes is uniform, 1/3 of the tubes will be metallic and the remaining 2/3 semiconducting [9].

2.2 Why are SWNTs so interesting?

With all the Carbon atoms bonded by sp^2 σ bond, SWNTs are promised to have excellent optical [12], mechanical [13], electrical [14, 15] and thermal properties [16, 17] which render them of great interest for a range of potential applications in many fields [18].

2.2.1 Electronic properties

Most material conductors can be classified as either metals or semiconductors. However, graphene, the parent material of carbon nanotubes, is known to be a semimetal or zero-gap semiconductor [19]. The electrical properties of different materials are illustrated schematically in Figure 2.5.

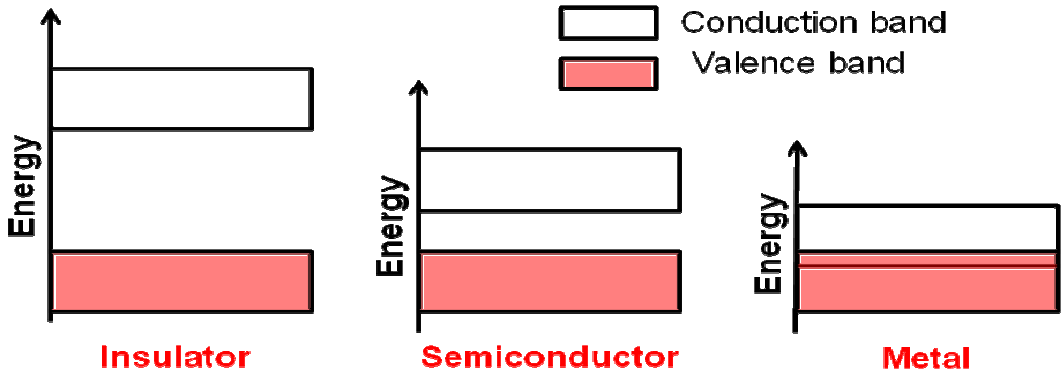

Figure 2.5 Electrical properties of different materials.

The electrical properties of a material depend on the separation between the valence band filled with electrons and the conduction band that is empty, shown in Figure 2.5. In metals, the two bands are overlapped, and many electrons can access the conduction band easily. There is a band gap between the valence band and conduction band in a semiconductor. However, with an energy boost from light or an electrical field, some electrons are able to jump the gap. Within graphene, there is a narrow path for a few electrons to a conduction state without any external boost, as shown in Figure 2.6, which makes it a unique semi-metal [19, 20]. A recent experimental study detected that the electrical properties of graphene quantum dots (GQD) and nanoribbons (GNR) significantly influenced by the edge structure [21]. By using ultrahigh-vacuum scanning tunnelling microscopy (UHV-STM), Ritter et al experimentally

measured the correlation between energy gap of GQD and GNR with the edge structure. The results showed that zigzag-edged graphene structures are more metallic than armchair structures, while armchair-edged graphenes are normal semiconductors. This indicates that controlled engineering of the graphene edge structure is probably required for obtaining uniform performance among graphene-based nanoelectronic devices.

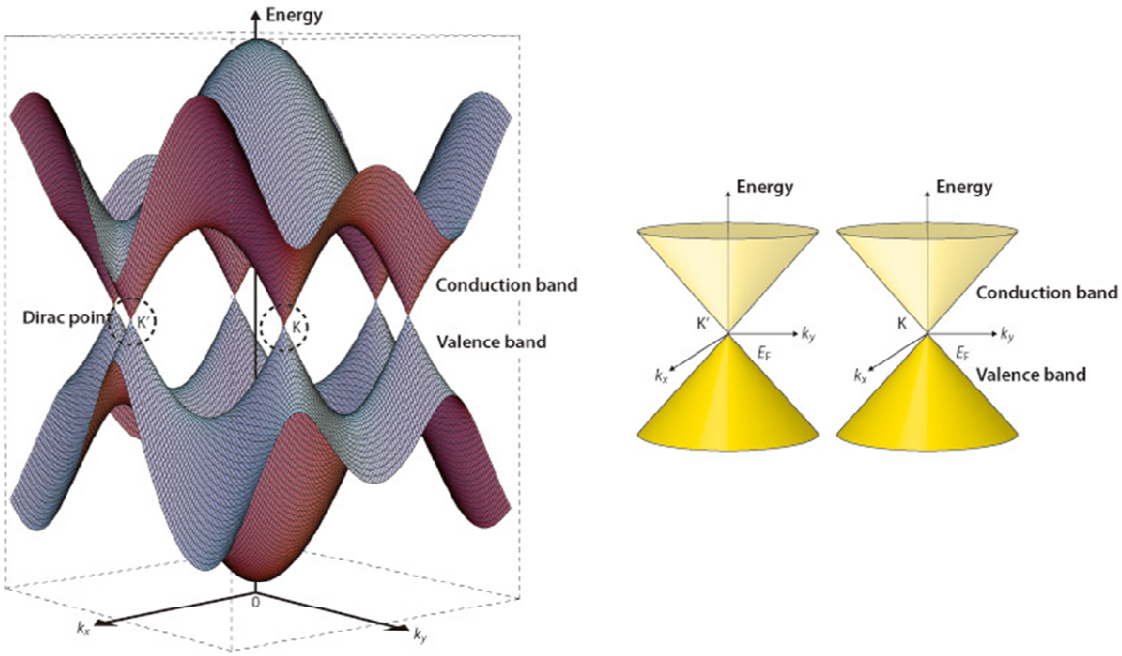

Figure 2.6 Energy band structure in graphene [22]

The electronic structure of SWNTs derives from that of a 2-D graphene sheet, but because of the radial confinement of the wave function, the continuous electronic density of states (DOS) in graphite divides into a series of spikes in SWNTs which are referred to as van Hove singularities [23]. Van Hove singularities are discontinuities in the density of states of a solid, usually s a result of low dimensionality on one or more directions [24]. SWNTs can be

metallic or semiconducting, depending on the chirality and diameter. Figure 2.7 below shows the DOS for both a (a) metallic and (b) semiconducting carbon nanotube where v_n represents the valence bands and c_n, the conduction bands for the first electronic transition [10]. DOS calculations can be performed using tight-binding and *ab-initio* calculations [25].

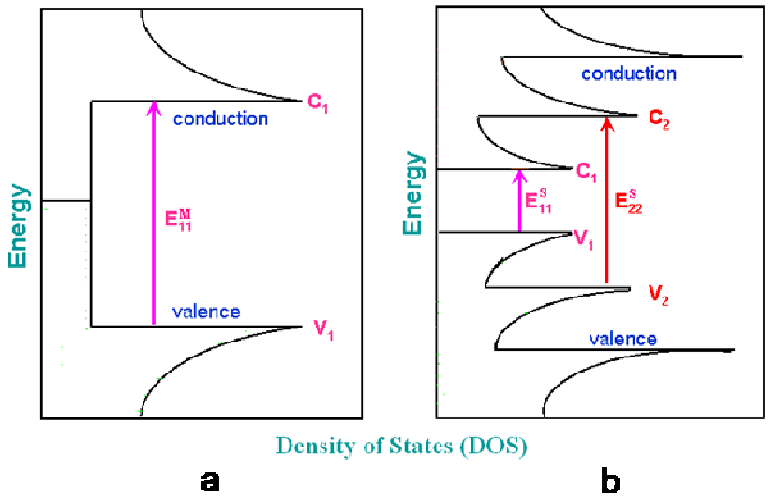

Figure 2.7 Schematic diagram of electronic density of states for (a) metallic, (b) semiconducting SWNTs [10]

E_{ii} (i = 1, 2, 3, …) describes the electronic transition between the states v_i and c_i. A simplified correlation between E_{ii} and nanotube diameter d has been established to predict the inter-band transition energies:

$$E_{ii}^{S,M} = 2na_{C-C}\gamma_0 / d \qquad \text{Equation 2.4}$$

where $a_{C\text{-}C}$ is the distance between the *C-C* bonds, chosen as 0.144 nm [10] or 0.142nm [9], γ_0 is the nearest-neighbour C-C interaction energy, values of 2.75eV [12] and 2.90eV [26] having been used for calculations and n is a constant. The value of n is 1, 2 and 4 for the 1st, 2nd and 3rd van Hove transitions

in semiconducting tubes and 3, and 6 for the 1st and 2nd van Hove transitions in metallic tubes respectively [10, 26]. Theoretical predictions suggest that the absorbance peaks of SWNT can be ascribed to the inter-band transitions between the mirror image spikes in the DOS of SWNT. The experimental optical absorption spectrum is presented and described in detail in Chapter 3.

2.2.2 Mechanical properties

The carbon atoms of a single sheet of graphite form a planar honeycomb lattice, in which each atom is connected via a strong sp^2 σ bond to three neighboring atoms. Related to the sp^2 bond strength, the basal plane elastic modulus of graphite is one of the largest of any known material, with a value of ~1060 GPa [27]. For this reason, the seamless cylindrical graphitic structures of SWNTs are expected to have many unique mechanical properties [28-32], including a high Young's modulus and a low specific weight. The Young's modulus of SWNTs has been determined to be higher than 1 TPa by theoretical calculation [33] and experimental measurement [28, 29, 34, 35], which is nearly the same as diamond. These properties render carbon nanotubes suitable candidates for reinforcing composites and ultrahigh frequency nano-mechanical resonator applications [36-39].

2.2.3 Thermal conductivity

It is known that monocrystalline diamond is one of the best thermal conductors as the atoms are connected by stiff sp^3 bonds [40]. Held together by stronger sp^2 σ bonds, carbon nanotubes are expected to have an unusually high thermal conductance [41]. The room temperature thermal conductivity of SWNTs has been predicted to be extremely high, exceeding even that of graphite or diamond [16]. For a single (10,10) SWNT, the thermal conductivity was measured to be 6, 600 W/m·K, which exceeds the reported room temperature thermal conductivity of isotopically pure diamond by almost a factor of 2 [17].

2.2.4 Nanoscale electronic properties

With the combination of nano-scale structure and unique electronic properties, SWNTs are considered to be an optimum candidate for nanometer-scale electromechanical tweezers, widely used in scanning probe microscopes (SPMs) such as the atomic force microscope (AFM) [39, 42, 43], which can yield surface topographies and scanning tunneling microscope (STM), which can be used to determine electronic bandgaps [44, 45].

2.3 What are the applications of SWNTs?

The excellent properties described above potentially open up an incredible range of applications of SWNTs in materials science, for example as reinforcement fibres for composites as SWNTs have high strength, high aspect

ratio, high thermal and chemical stability [46], electronics for example as conducting nanowires and field emitters as the excellent electronic properties of SWNTs [47-50], nanotools such as tips for Scanning Tunneling, Atomic Force, Magnetic Resonance Force and Scanning Near-field Optical, Chemical/Biological Force Microscopes, nanomanipulators and nanotweezers [39, 51], medical and biological sciences [52] and many other fields [53].

2.4 How to Produce SWNTs?

Since carbon nanotubes have so many excellent properties and potential applications described above, it is highly desirable to have large quantities of pure nanotubes. Many different techniques exist and are used to produce the material. Table 2.1 summaries the contemporary SWNTs synthesis techniques and product description [54]. In this section, the most important techniques, arc discharge, laser vaporization, chemical vapour deposition (CVD) and high pressure decomposition of CO (HiPco), are described in details.

Table 2.1 Summary of the contemporary SWNTs synthesis techniques and product description, adapted from [54].

Synthesis methods	Technology of preparation	Typical mean diameter (nm)	Product description
Arc discharge	First reported production [2, 3]	1.5 (0.9-3.1)	Less quality, carbonaceous impurities abundant, bundled.
Laser ablation	Ablation from graphite doped with catalyst [55]	1.4 (1-1.8)	High quality, good diameter control, bundled tubes.
chemical vapour deposition	Catalytic chemical vapour deposition. Supported metal catalysts are used [56]	1.5 (1.3-2)	Cheapest, commercial, up-scalable. Most feasible from application point of view.
Gas phase decomposition	Decomposition in an oxygen-free environment. Typical: HiPco [57]	1 (0.9-1.3)	Easy purification, commercial, good quality.
Flame pyrolysis	Carbon source + metallocene catalyst, comventional low pressure pyrolysis reactor [58]	2-3	Low yield, bad quality. Still under development. Plant technology available, large commercialization potential.
Solar furnace	Solar rays focused on a metal doped graphite target [59]	1.4	Good quality SCNTs, little amorphous carbon.
Inner tubes of DWCNTs	Catalyst free growth from peapods by coalescence of C_{60} molecules [60]	0.7 (0.55-1)	Well shielded, best quality. Seperation from outer tubes is very challenging.
Zeolite grown	CNTs grow by thermal decomposition of template molecules within zeolite channels [61]	0.45	Monodisperse diameter distribution, oriented tubes. SWNTs metastable outside the channels

2.4.1 Electric arc discharge

The electric arc discharge method, initially used for producing C_{60} fullerenes [62], was the first reported and is still one of the most widely used techniques for the production of SWNTs. Isolated SWNTs can be produced by including transition metals as catalysts, such as Fe, Co, Ni and rare earth metals such as Y and Gd [2, 3, 63], whereas composite catalysts such as Fe/Ni , Co/Ni and Ni/Y have been used to synthesize bundles of SWNTs [64, 65]. SWNTs have

also been prepared by using various oxides (Y_2O_3, La_2O_3, CeO_2) as catalysts [66, 67]. Typical diameters of SWNTs produced by this method are in the range 0.9-3.1 nm, with an average of 1.5 nm [54].

Compared to other methods, arc discharge is a more common and easy way to produce a less defective, large scale product. However more by-products such as amorphous carbon, multi-shell graphite particles and catalytic metal particles are formed during the process and are typically present in amounts up to 30% by weight of the product.

2.4.2 Laser vaporization

The laser vaporization technique for synthesising carbon nanotubes was first reported in 1995 by Smally's group [55]. The laser vaporization apparatus used by Smalley's group is shown in Figure 2.8.

Nanotubes produced by laser ablation are purer (up to about 90 % purity) than those produced in the arc discharge process. The SWNTs produced by this technique are normally bundles with narrower diameter distribution, normally 1.0-1.8 nm with an average of 1.4 nm. Unfortunately, the laser technique is not economically advantageous because the process requires high-purity graphite rods, the laser powers required are high (in some cases two laser beams are required), and the amount of SWNTs that can be produced per day is not as high as the arc discharge method [55].

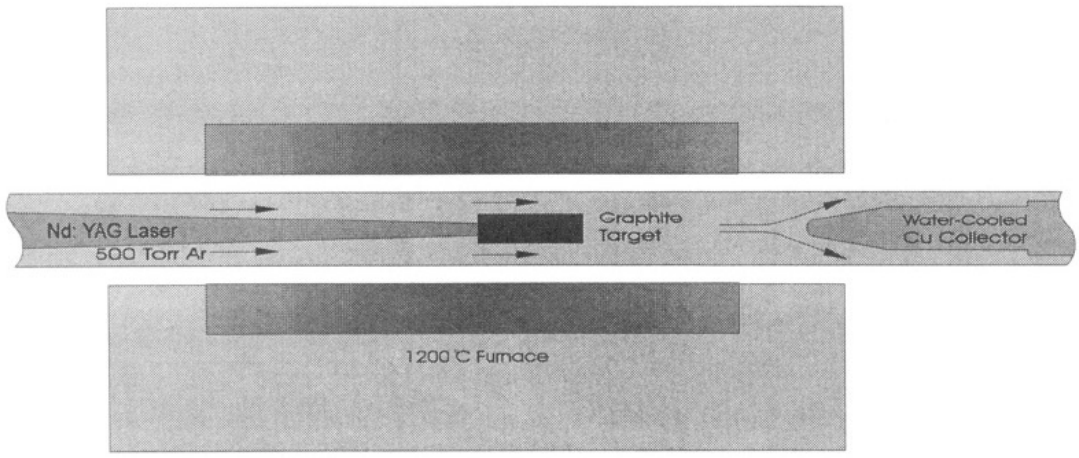

Figure 2.8 Schematic representation of oven laser-vapourisation apparatus used at Rice University [55]

2.4.3 Chemical vapour deposition (CVD)

Chemical vapour deposition (CVD) is one of the most popular methods for synthesizing SWNTs. Different from arc discharge and laser vaporization techniques, catalytic CVD requires a medium temperature (700-1473 K) and long time reaction (typically minutes to hours), whereas the other two can be classified as high temperature (>3000 K) and short time reaction (μs-ms) techniques [68-71].

SWNTs produced by CVD techniques can grow on a conventional or patterned substrate, which allows the possibility of synthesising aligned SWNTs [68-71]. In the last ten years, different techniques for the synthesis of carbon nanotubes with CVD have been developed, such as plasma enhanced CVD [72, 73],

thermal chemical CVD [74], alcohol catalytic CVD [74, 75], vapour phase growth [76], aero gel-supported CVD [77] and laser-assisted CVD [78].

CVD technique can produce high purity SWNT samples (up to 96%) [79], normally with a diameter range between 1 nm to 2 nm [80]. It was also reported to be able to produce large diameter SWNTs greater than 3 nm [81].

2.4.4 High pressure decomposition of CO (HiPco)

The high pressure CO disproportionation process (HiPco) is a technique for catalytic production of SWNTs in a continuous-flow gas phase using CO as the carbon feedstock and $Fe(CO)_5$ as the iron-containing catalyst precursor [57]. SWNTs are produced by flowing CO, mixed with a small amount of $Fe(CO)_5$ through a heated reactor. The current production rates approach 450 mg/h (or 10 g/day), and nanotubes typically have no more than 7 mol % of iron impurities. Figure 2.9 shows the layout of a CO flow-tube reactor [57].

The average diameter of HiPco SWNTs is approximately 1.1 nm [82], which is typically smaller than SWNTs produced by the laser-oven process, where the average diameter is about 1.3 - 1.4 nm [83]. The dominant impurity in HiPco nanotubes is the metal catalyst, which is encased in thin carbon shells and distributed throughout the sample as 3-5 nm size particles [82]. Compared with other techniques, production by the HiPco method has the advantages of high quality, ease of purification and large scale commercial products.

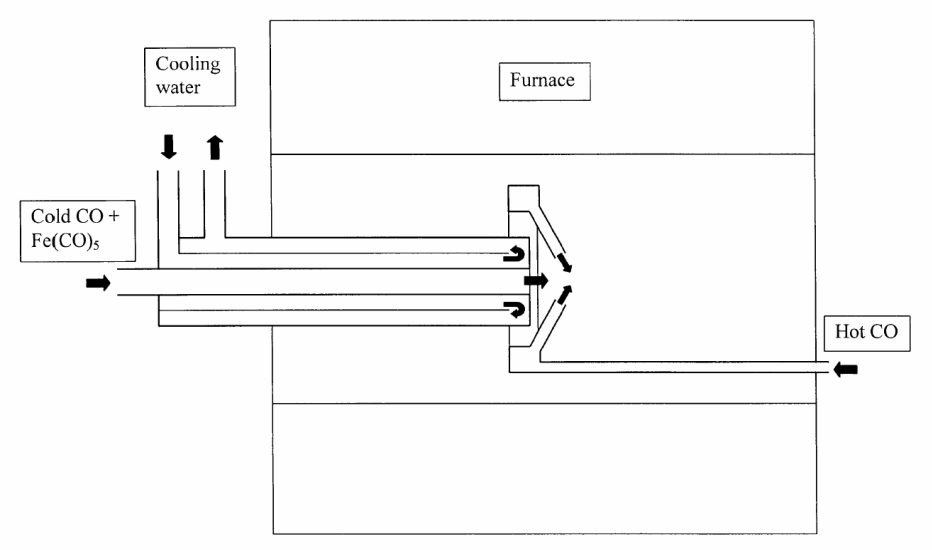

Figure 2.9 Layout of CO flow-tube reactor [57]

2.5 What are the problems preventing industrial applications?

SWNTs were predicted to have great application in many fields. However most of the applications are still in the stage of laboratory research. The high cost, polydispersity in nanotube type and limitations in processing and assembly methods are the most significant obstacles facing the realisation of many industrial applications.

Although SWNTs were discovered nearly two decades ago, and many production methods have been developed, researchers are still devoting considerable effort to finding a proper way to synthesize high quality, low cost SWNTs, to face the increasing requirements of the developing industry.

Currently, as-produced SWNTs always contain different types of impurities, such as fullerenes, metal particles from the catalyst which are always coated by a carbon layer and amorphous carbon. Often the removal of the by product costs more than the synthesis of SWNTs, hindering the application of SWNTs in many fields such as electronics where high purity is needed.

The price of SWNTs remains very high. High purity (> 80%) tubes with (7,6) chirality costs €868/g and even samples containing substantial impurities cost over €200/g (Sigma Aldrich, March 2010). The high cost of SWNTs is an impediment to their large scale applications.

In addition, strong van der Waals forces between the tubes mean that they grow in bundles or ropes (Figure 1.2). Their relative insolubility in common organic solvents compounds the problem and the solubilisation and dispersion of SWNTs remains a challenge for the breakthrough in applications of SWNTs. Furthermore, the synthesis of SWNTs is not structurally specific and thus as-produced samples contain metallic and semiconducting structures. The polydispersity in nanotube type makes it difficult if specific electronic structures are needed. Thus the selection of SWNTs with different electronic properties becomes essential [84].

2.6 How to solve the problems?

Since the discovery of SWNTs, scientists from the chemical, physical and biological sciences have been trying to solve the existing problems. Efforts include the development of the synthesis method to achieve high quantity and quality and low cost tubes as well as covalent [85-87] and noncovalent [88-91] functionalisation of SWNTs to improve the solubility in water and common organic solvents. Depending on the reactivity of the impurities and the stability of the tubes, chemical and physical or even combined methods have been developed to purify and debundle SWNTs. These include oxidation in air or acid and microwave treatment [92], size selection chromatography [92-94], filtration [95] and directly dissolving [96, 97] SWNTs in organic solvents.

2.7 Summary

This chapter provided a brief introduction to Single-walled Carbon Nanotubes, particularly the structure, properties, production methods and impediments to realisation of their applications potential. Due to the unique structure SWNTs are predicted to have excellent electrical and mechanical properties, and also have great potential application in energy storage and thermal conduction. Although the synthetic techniques have been developing for nearly two decades, the as-produced SWNTs are still not readily meeting the requirements. Different purification methods have been developed for different purposes. Proper solvents, in which pristine SWNTs can be dispersed and debundled without introduction of any third component in the solution, are highly desirable for the

promotion of the application of SWNTs. This thesis aims to explore the efficacy of a range of organic solvents to disperse and solubilise SWNTs. Systematic structural variation is employed in an effort to elucidate the underlying physical mechanisms and guide optimisation of the processes.

2.8 Reference

1. Saito, R.; Dresselhaus, G.; Dresselhaus, M.S., Physical Properties of Carbon Nanotubes. 1998, Imperial College Press.
2. Bethune, D.S.; Kiang, C.H.; Devries, M.S.; Gorman, G.; Savoy, R.; Vazquez, J.; Beyers, R. Cobalt-Catalyzed Growth of Carbon Nanotubes with Single-Atomic-Layerwalls. Nature, 1993, **363**, 605-607.
3. Iijima, S.; Ichihashi, T. Single-Shell Carbon Nanotubes of 1-nm Diameter. Nature, 1993, **363**, 603-605.
4. Rao, C.N.R.; Satishkumar, B.C.; Govindaraj, A.; Nath, M. Nanotubes. Chemphyschem, 2001, **2**, 78-105.
5. Odom, T.W.; Huang, J.L.; Kim, P.; Lieber, C.M. Atomic structure and electronic properties of single-walled carbon nanotubes. Nature, 1998, **391**, 62-64.
6. Wildoer, J.W.G.; Venema, L.C.; Rinzler, A.G.; Smalley, R.E.; Dekker, C. Electronic structure of atomically resolved carbon nanotubes. Nature, 1998, **391**, 59-62.

7. Gao, G.H.; Cagin, T.; Goddard, W.A. Energetics, structure, mechanical and vibrational properties of single-walled carbon nanotubes. Nanotechnology, 1998, **9**, 184-191.

8. Rao C.N.R.; Rovindaraj, A. Nanotubes and Nanowires. 2005, RSC Publishing.

9. Saito, R.; Fujita, M.; Dresselhaus, G.; Dresselhaus, M.S. Electronic-Structure of Chiral Graphene Tubules. Applied Physics Letters, 1992, **60**, 2204-2206.

10. Yu, Z.H.; Brus, L. Rayleigh and Raman scattering from individual carbon nanotube bundles. Journal of Physical Chemistry B, 2001, **105**, 1123-1134.

11. Dresselhaus, M.S.; Dresselhaus, G.; Eklund, P. Science of Fullerenes and Carbon Nanotubes. 1996, Academic Press.

12. Kataura, H.; Kumazawa, Y.; Maniwa, Y.; Umezu, I.; Suzuki, S.; Ohtsuka, Y.; Achiba, Y. Optical properties of single-wall carbon nanotubes. Synthetic Metals, 1999, **103**, 2555-2558.

13. Yu, M.F.; Files, B.S.; Arepalli, S.; Ruoff, R.S. Tensile loading of ropes of single wall carbon nanotubes and their mechanical properties. Physical Review Letters, 2000, **84**, 5552-5555.

14. Zhou, C.W.; Kong, J.; Dai, H.J. Intrinsic electrical properties of individual single-walled carbon nanotubes with small band gaps. Physical Review Letters, 2000, **84**, 5604-5607.

15. Javey, A.; Shim, M.; Dai, H.J. Electrical properties and devices of large-diameter single-walled carbon nanotubes. Applied Physics Letters, 2002, **80**, 1064-1066.

16. Hone, J.; Whitney, M.; Piskoti, C.; Zettl, A. Thermal conductivity of single-walled carbon nanotubes. Physical Review B, 1999, **59**, R2514-R2516.

17. Berber, S.; Kwon, Y.K.; Tomanek, D. Unusually high thermal conductivity of carbon nanotubes. Physical Review Letters, 2000, **84**, 4613-4616.

18. Ajayan, P.M.; Zhou, O.Z. Applications of carbon nanotubes. Carbon Nanotubes, 2001, **80**, 391-425.

19. Collins, P.G.; Avouris, P. Nanotubes for electronics. Scientific American, 2000, **283**, 62-69.

20. Anantram, M.P.; Leonard, F. Physics of carbon nanotube electronic devices. Reports on Progress in Physics, 2006, **69**, 507-561.

21. Ritter, K.A.; Lyding, J.W. The influence of edge structure on the electronic properties of graphene quantum dots and nanoribbons. Nature Materials, 2009, **8**, 235-242.

22. Ando, T. The electronic properties of graphene and carbon nanotubes. NPG Asia Materials, 2009, **1**, 17-21.

23. Kataura, H.; Kumazawa, Y.; Maniwa, Y.; Umezu, I.; Suzuki, S.; Ohtsuka, Y.; Achiba, Y. Optical properties of single-wall carbon nanotubes. Synthetic Metals, 1999, **103**, 2555-2558.

24. Van Hove, L. The Occurrence of Singularities in the Elastic Frequency Distribution of a Crystal. Physics Review, 1953, **89**, 1189-1193.

25. Reich, S.; Thomsen, C.; Maultzsch, J., Carbon nanotubes: basic concepts and physical properties. 2004, Wiley-VCH Verlag GmbH & Co. KGaA.

26. Jorio, A.; Saito, R.; Hafner, J.H.; Lieber, C.M.; Hunter, M.; McClure, T.; Dresselhaus, G.; Dresselhaus, M.S. Structural (n, m) determination of

isolated single-wall carbon nanotubes by resonant Raman scattering. 2001, 86, 1118-1121. Physical Review Letters 2001, **86**, 1118-1121.

27. Poncharal, P.; Wang, Z.L.; Ugarte, D.; de Heer, W.A. Electrostatic Deflections and Electromechanical Resonances of Carbon Nanotubes Science, 1999, **283**, 1513-1516.

28. Treacy, M.M.J.; Ebbesen, T.W.; Gibson, J.M. Exceptionally high Young's modulus observed for individual carbon nanotubes. Nature, 1996, **381**, 678-680.

29. Lourie, O.; Wagner, H.D. Evaluation of Young's modulus of carbon nanotubes by micro-Raman spectroscopy. Journal of Materials Research, 1998, **13**, 2418-2422.

30. Poncharal, P.; Wang, Z.L.; Ugarte, D.; de Heer, W.A. Electrostatic deflections and electromechanical resonances of carbon nanotubes. Science, 1999, **283**, 1513-1516.

31. Walters, D.A.; Ericson, L.M.; Casavant, M.J.; Liu, J.; Colbert, D.T.; Smith, K.A.; Smalley, R.E. Elastic strain of freely suspended single-wall carbon nanotube ropes. Applied Physics Letters, 1999, **74**, 3803-3805.

32. Yu, M.F.; Lourie, O.; Dyer, M.J.; Moloni, K.; Kelly, T.F.; Ruoff, R.S. Strength and breaking mechanism of multiwalled carbon nanotubes under tensile load. Science, 2000, **287**, 637-640.

33. Lu, J.P. Elastic properties of carbon nanotubes and nanoropes. Physical Review Letters, 1997, **79**, 1297-1300.

34. Rice, N.A.; Soper, K.; Zhou, N.Z.; Merschrod, E.; Zhao, Y.M. Dispersing as-prepared single-walled carbon nanotube powders with linear conjugated polymers. Chemical Communications, 20064937-4939.

35. Krishnan, A.; Dujardin, E.; Ebbesen, T.W.; Yianilos, P.N.; Treacy, M.M.J. Young's modulus of single-walled nanotubes. Physical Review B, 1998, **58**, 14013-14019.

36. Babic, B.; Furer, J.; Sahoo, S.; Farhangfar, S.; Schonenberger, C. Intrinsic thermal vibrations of suspended doubly clamped single-wall carbon nanotubes. Nano Letters, 2003, **3**, 1577-1580.

37. Li, C.Y.; Chou, T.W. Single-walled carbon nanotubes as ultrahigh frequency nanomechanical resonators. Physical Review B, 2003, **68**, 073405.

38. Li, C.Y.; Chou, T.W. Strain and pressure sensing using single-walled carbon nanotubes. Nanotechnology, 2004, **15**, 1493-1496.

39. Cheung, C.L.; Hafner, J.H.; Lieber, C.M. Carbon nanotube atomic force microscopy tips: Direct growth by chemical vapor deposition and application to high-resolution imaging. Proceedings of the National Academy of Sciences of the United States of America, 2000, **97**, 3809-3813.

40. Wei, L.H.; Kuo, P.K.; Thomas, R.L.; Anthony, T.R.; Banholzer, W.F. Thermal-Conductivity of Isotopically Modified Single-Crystal Diamond. Physical Review Letters, 1993, **70**, 3764-3767.

41. Hone, J. Carbon Nanotubes: Thermal Properties. Dekker Encyclopedia of Nanoscience and Nanotechnology, 2004.

42. Austin, A.J.; Nguyen, C.V.; Ngo, Q. Electrical conduction of carbon nanotube atomic force microscopy tips: Applications in nanofabrication. Journal of Applied Physics, 2006, **99**, 114304.

43. Wilson, N.R.; Macpherson, J.V. Carbon nanotube tips for atomic force microscopy. Nature Nanotechnology, 2009, **4**, 483-491.

44. Pasquini, A.; Picotto, G.B.; Pisani, M. STM carbon nanotube tips fabrication for critical dimension measurements. Sensors and Actuators a-Physical, 2005, **123-24**, 655-659.

45. Shingaya, Y.; Nakayama, T.; Aono, M. Carbon nanotube tip for scanning tunneling microscopy. Physica B-Condensed Matter, 2002, **323**, 153-155.

46. Biercuk, M.J.; Llaguno, M.C.; Radosavljevic, M.; Hyun, J.K.; Johnson, A.T.; Fischer, J.E. Carbon nanotube composites for thermal management. Applied Physics Letters, 2002, **80**, 2767-2769.

47. Milne, W.I.; Teo, K.B.K.; Amaratunga, G.A.J.; Legagneux, P.; Gangloff, L.; Schnell, J.P.; Semet, V.; Binh, V.T.; Groening, O. Carbon nanotubes as field emission sources. Journal of Materials Chemistry, 2004, **14**, 933-943.

48. Saito, Y.; Uemura, S. Field emission from carbon nanotubes and its application to electron sources. Carbon, 2000, **38**, 169-182.

49. Dekker, C. Carbon nanotubes as molecular quantum wires. Physics Today, 1999, **52**, 22-28.

50. Diehl, M.R.; Steuerman, D.W.; Tseng, H.R.; Vignon, S.A.; Star, A.; Celestre, P.C.; Stoddart, J.F.; Heath, J.R. Single-walled carbon nanotube based molecular switch tunnel junctions. Chemphyschem, 2003, **4**, 1335-1339.

51. Dresselhaus, M.S.; Avouris, Ph., Carbon Nanotubes: Synthesis, Structure, Properties and Applications. 2001, Springer.

52. Lin, Y.; Taylor, S.; Li, H.P.; Fernando, K.A.S.; Qu, L.W.; Wang, W.; Gu, L.R.; Zhou, B.; Sun, Y.P. Advances toward bioapplications of carbon nanotubes. Journal of Materials Chemistry, 2004, **14**, 527-541.

53. Lu, S.X.Panchapakesan, B. Photoconductivity in single wall carbon nanotube sheets. Nanotechnology, 2006, **17**, 1843-1850.

54. Kuzmany, H.; Kukovecz, A.; Simon, F.; Holzweber, A.; Kramberger, C.; Pichler, T. Functionalization of carbon nanotubes. Synthetic metals, 2004, **141**, 113-122.

55. Guo, T.; Nikolaev, P.; Rinzler, A.G.; Tomanek, D.; Colbert, D.T.; Smalley, R.E. Self-Assembly of Tubular Fullerenes. Journal of Physical Chemistry, 1995, **99**, 10694-10697.

56. Colomer, J.F.; Stephan, C.; Lefrant, S.; Van Tendeloo, G.; Willems, I.; Konya, Z.; Fonseca, A.; Laurent, C.; Nagy, J.B. Large-scale synthesis of single-wall carbon nanotubes by catalytic chemical vapor deposition (CCVD) method. Chemical Physics Letters, 2000, **317**, 83-89.

57. Nikolaev, P.; Bronikowski, M.J.; Bradley, R.K.; Rohmund, F.; Colbert, D.T.; Smith, K.A.; Smalley, R.E. Gas-phase catalytic growth of single-walled carbon nanotubes from carbon monoxide. Chemical Physics Letters, 1999, **313**, 91-97.

58. Vander Wal, R.L.; Ticich, T.M.; Curtis, V.E. Flame synthesis of metal-catalyzed single-wall carbon nanotubes. Journal of Physical Chemistry A, 2000, **104**, 7209-7217.

59. Laplaze, D.; Bernier, P.; Maser, W.K.; Flamant, G.; Guillard, T.; Loiseau, A. Carbon nanotubes: The solar approach. Carbon, 1998, **36**, 685-688.

60. Bandow, S.; Takizawa, M.; Hirahara, K.; Yudasaka, M.; Iijima, S. Raman scattering study of double-wall carbon nanotubes derived from the chains of fullerenes in single-wall carbon nanotubes. Chemical Physics Letters, 2001, **337**, 48-54.

61. Tang, Z.K.; Sun, H.D.; Wang, J.; Chen, J.; Li, G. Mono-sized single-wall carbon nanotubes formed in channels of AlPO4-5 single crystal. Applied Physics Letters, 1998, **73**, 2287-2289.

62. Iijima, S. Helical Microtubules of Graphitic Carbon. Nature, 1991, **354**, 56-58.

63. Saito, Y.; Okuda, M.; Fujimoto, N.; Yoshikawa, T.; Tomita, M.; Hayashi, T. Single-Wall Carbon Nanotubes Growing Radially from Ni Fine Particles Formed by Arc Evaporation. Japanese Journal of Applied Physics Part 2-Letters, 1994, **33**, L526-L529.

64. Seraphin, S.Zhou, D. Single-Walled Carbon Nanotubes Produced at High-Yield by Mixed Catalysts. Applied Physics Letters, 1994, **64**, 2087-2089.

65. Glerup, M.; Steinmetz, J.; Samaille, D.; Stephan, O.; Enouz, S.; Loiseau, A.; Roth, S.; Bernier, P. Synthesis of N-doped SWNT using the arc-discharge procedure. Chemical Physics Letters, 2004, **387**, 193-197.

66. Saito, Y.; Kawabata, K.; Okuda, M. Single-Layered Carbon Nanotubes Synthesized by Catalytic Assistance of Rare-Earths in a Carbon-Arc. Journal of Physical Chemistry, 1995, **99**, 16076-16079.

67. Lv, X.; Du, F.; Ma, Y.F.; Wu, Q.; Chen, Y.S. Synthesis of high quality single-walled carbon nanotubes at large scale by electric arc using metal compounds. Carbon, 2005, **43**, 2020-2022.

68. Ago, H.; Qi, J.F.; Tsukagoshi, K.; Murata, K.; Ohshima, S.; Aoyagi, Y.; Yumura, M. Catalytic growth of carbon nanotubes and their patterning based on ink-jet and lithographic techniques. Journal of Electroanalytical Chemistry, 2003, **559**, 25-30.

69. Han, Y.S.; Shin, J.K.; Kim, S.T. Synthesis of carbon nanotube bridges on patterned silicon wafers by selective lateral growth. Journal of Applied Physics, 2001, **90**, 5731-5734.

70. Kong, J.; Soh, H.T.; Cassell, A.M.; Quate, C.F.; Dai, H.J. Synthesis of individual single-walled carbon nanotubes on patterned silicon wafers. Nature, 1998, **395**, 878-881.

71. Hongo, H.; Nihey, F.; Ochiai, Y. Horizontally directional single-wall carbon nanotubes grown by chemical vapor deposition with a local electric field. Journal of Applied Physics, 2007, **101**, 024325.

72. Amama, P.B.; Maschmann, M.R.; Fisher, T.S.; Sands, T.D. Dendrimer-templated Fe nanoparticles for the growth of single-wall carbon nanotubes by plasma-enhanced CVD. Journal of Physical Chemistry B, 2006, **110**, 10636-10644.

73. Delzeit, L.; Nguyen, C.V.; Stevens, R.M.; Han, J.; Meyyappan, M. Growth of carbon nanotubes by thermal and plasma chemical vapour deposition processes and applications in microscopy. Nanotechnology, 2002, **13**, 280-284.

74. Liao, H.W.Hafner, J.H. Low-temperature single-wall carbon nanotube synthesis by thermal chemical vapor deposition. Journal of Physical Chemistry B, 2004, **108**, 6941-6943.

75. Maruyama, S. CVD Synthesis of Single-Walled Carbon Nanotubes from Alcohol, Nanotube'04 Conference, 2004.

76. Lee, C.J.; Lyu, S.C.; Kim, H.W.; Park, C.Y.; Yang, C.W. Large-scale production of aligned carbon nanotubes by the vapor phase growth method. Chemical Physics Letters, 2002, **359**, 109-114.

77. Su, M.; Zheng, B.; Liu, J. A scalable CVD method for the synthesis of single-walled carbon nanotubes with high catalyst productivity. Chemical Physics Letters, 2000, **322**, 321-326.

78. Rummeli, M.H.; Kramberger, C.; Loffler, M.; Kalbac, M.; Hubers, H.W.; Gruneis, A.; Barreiro, A.; Grimm, D.; Ayala, P.; Gemming, T.; Schaffel, F.; Dunsch, L.; Buchner, B.; Pichler, T. Synthesis of single wall carbon nanotubes with invariant diameters using a modified laser assisted chemical vapour deposition route. Nanotechnology, 2006, **17**, 5469-5473.

79. Li, Y.L.; Zhang, L.H.; Zhong, X.H.; Windle, A.H. Synthesis of high purity single-walled carbon nanotubes from ethanol by catalytic gas flow CVD reactions. Nanotechnology, 2007, **18**, 225604.

80. Byon, H.R.; Lim, H.; Song, H.J.; Choi, H.C. A synthesis of high purity single-walled carbon nanotubes from small diameters of cobalt nanoparticles by using oxygen-assisted chemical vapor deposition process. Bulletin of the Korean Chemical Society, 2007, **28**, 2056-2060.

81. Yang, Q.H.; Bai, S.; Sauvajol, J.L.; Bai, J.B. Large-diameter single-walled carbon nanotubes synthesized by chemical vapor deposition. Advanced Materials, 2003, **15**, 792-795.

82. Chiang, I.W.; Brinson, B.E.; Huang, A.Y.; Willis, P.A.; Bronikowski, M.J.; Margrave, J.L.; Smalley, R.E.; Hauge, R.H. Purification and

characterization of single-wall carbon nanotubes (SWNTs) obtained from the gas-phase decomposition of CO (HiPco process). Journal of Physical Chemistry B, 2001, **105**, 8297-8301.

83. Yudasaka, M.; Yamada, R.; Sensui, N.; Wilkins, T.; Ichihashi, T.; Iijima, S. Mechanism of the effect of NiCo, Ni and Co catalysts on the yield of single-wall carbon nanotubes formed by pulsed Nd : YAG laser ablation. Journal of Physical Chemistry B, 1999, **103**, 6224-6229.

84. Krupke, R.; Hennrich, F. Separation techniques for carbon nanotubes. Advanced Engineering Materials, 2005, **7**, 111-116.

85. Guo, Z.; Du, F.; Ren, D.M.; Chen, Y.S.; Zheng, J.Y.; Liu, Z.B.; Tian, J.G. Covalently porphyrin-functionalized single-walled carbon nanotubes: a novel photoactive and optical limiting donor-acceptor nanohybrid. Journal of Materials Chemistry, 2006, **16**, 3021-3030.

86. Wong, S.S.; Joselevich, E.; Woolley, A.T.; Cheung, C.L.; Lieber, C.M. Covalently functionalized nanotubes as nanometre-sized probes in chemistry and biology. Nature, 1998, **394**, 52-55.

87. Bahr, J.L.; Tour, J.M. Covalent chemistry of single-wall carbon nanotubes. Journal of Materials Chemistry, 2002, **12**, 1952-1958.

88. Gregan, E.; Keogh, S.M.; Maguire, A.; Hedderman, T.G.; Neill, L.O.; Chambers, G.; Byrne, H.J. Purification and isolation of SWNTs. Carbon, 2004, **42**, 1031-1035.

89. Liu, Y.T.; Zhao, W.; Huang, Z.Y.; Gao, Y.F.; Xie, X.M.; Wang, X.H.; Ye, X.Y. Noncovalent surface modification of carbon nanotubes for solubility in organic solvents. Carbon, 2006, **44**, 1613-1616.

90. Star, A.; Liu, Y.; Grant, K.; Ridvan, L.; Stoddart, J.F.; Steuerman, D.W.; Diehl, M.R.; Boukai, A.; Heath, J.R. Noncovalent side-wall functionalization of single-walled carbon nanotubes. Macromolecules, 2003, **36**, 553-560.

91. Chen, J.; Liu, H.Y.; Weimer, W.A.; Halls, M.D.; Waldeck, D.H.; Walker, G.C. Noncovalent engineering of carbon nanotube surfaces by rigid, functional conjugated polymers. Journal of the American Chemical Society, 2002, **124**, 9034-9035.

92. Li, Y.; Zhang, X.B.; Luo, J.H.; Huang, W.Z.; Cheng, J.P.; Luo, Z.Q.; Li, T.; Liu, F.; Xu, G.L.; Ke, X.X.; Li, L.; Geise, H.J. Purification of CVD synthesized single-wall carbon nanotubes by different acid oxidation treatments. Nanotechnology, 2004, **15**, 1645-1649.

93. Duesberg, G.S.; Burghard, M.; Muster, J.; Philipp, G.; Roth, S. Separation of carbon nanotubes by size exclusion chromatography. Chemical Communications, 1998435-436.

94. Duesberg, G.S.; Blau, W.; Byrne, H.J.; Muster, J.; Burghard, M.; Roth, S. Chromatography of carbon nanotubes. Synthetic Metals, 1999, **103**, 2484-2485.

95. Kim, Y.; Luzzi, D.E. Purification of pulsed laser synthesized single wall carbon nanotubes by magnetic filtration. Journal of Physical Chemistry B, 2005, **109**, 16636-16643.

96. Giordani, S.; Bergin, S.D.; Nicolosi, V.; Lebedkin, S.; Kappes, M.M.; Blau, W.J.; Coleman, J.N. Debundling of single-walled nanotubes by dilution: Observation of large populations of individual nanotubes in amide solvent dispersions. Journal of Physical Chemistry B, 2006, **110**, 15708-15718.

97. Ausman, K.D.; Piner, R.; Lourie, O.; Ruoff, R.S.; Korobov, M. Organic solvent dispersions of single-walled carbon nanotubes: Toward solutions of pristine nanotubes. Journal of Physical Chemistry B, 2000, **104**, 8911-8915.

CHAPTER 3
CHARACTERIZATION TECHNIQUES

3.1 UV-Vis-NIR Spectroscopy

3.1.1 Absorption and Scattering

When an electron in the ground state absorbs the incident energy of a photon and is excited to a higher energy level, absorption takes place. Figure 3.1 illustrates a simple schematic of absorption and emission (fluorescence) in a molecule between the ground state (E_0) to two excited states (E_1, E_2). The wavelength at which a molecule absorbs light is determined by the energy gaps between the excited states and the ground state (E_1 - E_0, or E_2 - E_0). When the incident light contains an energy that matches a possible electronic transition within the sample molecule, the light will be absorbed, and as a result, the electron is promoted to a higher energy orbital. An optical spectrometer records the wavelength at which absorption occurs, together with the degree of absorption (absorbance, A) at each wavelength, producing a spectrum of absorbance as a function of wavelength [1].

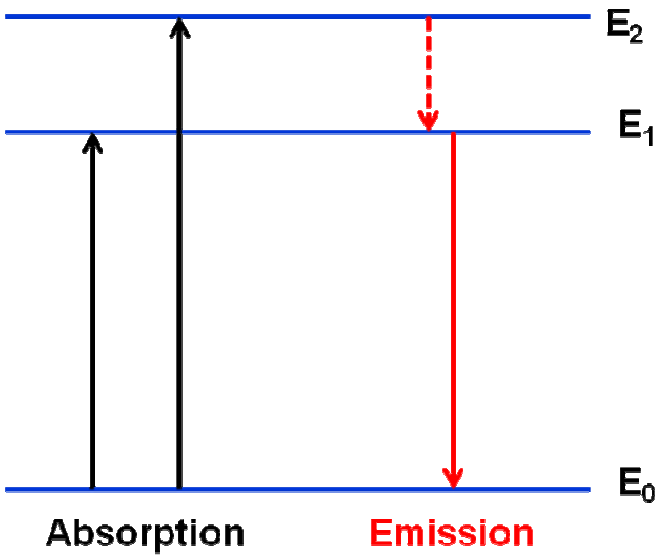

Figure 3.1 Ground state (E_0) and two excited states (E_1, E_2) of a molecule (vibrational and rotational levels are not shown), reproduced from Ref. [1].

The absorbance (A) at a specific wavelength (λ) is defined as [1]

$$A = -log\ (I/I_0) \qquad \text{Equation 3.1[1]}$$

where I_0 and I are the incident light intensity and transmitted light intensity, as shown in Figure 3.2. In an ideal molecular solution, the absorbance of a sample can be related to the molar concentration (c) and the sample thickness (l) by the Beer-Lambert law, via the molar extinction co-efficient ε.

$$A = \varepsilon cl \qquad \text{Equation 3.2 [1]}$$

ε is wavelength dependent and describes the probability of absorption of a phonon by a chromophore at the excitation energy. In the absence of aggregation it is concentration independent.

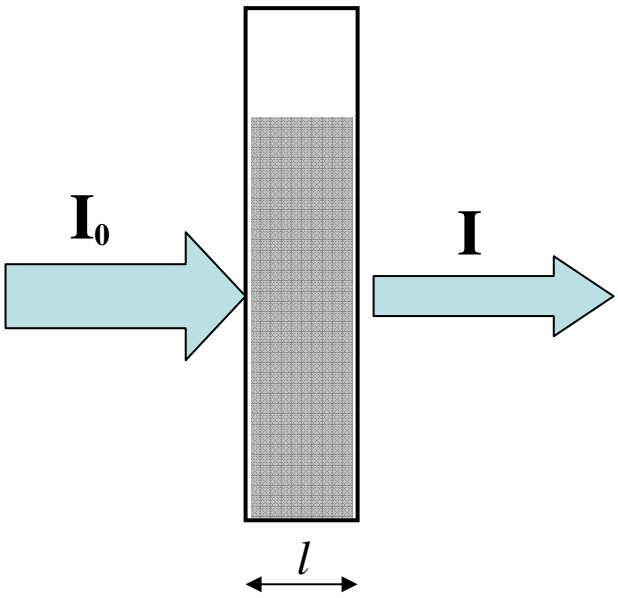

Figure 3.2 Schematic of absorption when light passes through a sample

In dispersions of aggregates, such as those of SWNTs in solvents which normally contain large bundles of tubes, the scattering of light cannot be ignored. Depending on the particle size, elastic scattering can take place and can be mainly of two types, Rayleigh and Mie scattering. Rayleigh scattering occurs when the diameter of the particle is less than one tenth of the wavelength of the incident beam and the scattered intensity is inversely proportional to the fourth power of the wavelength of the incident beam [2].

On the other hand, Mie scattering occurs when the particle size is equal to or greater than the incident wavelength. As the particle size increases, forward scattering dominates over back scattering and a forward lobe is formed, unlike Rayleigh scattering which occurs in all directions forming forward and backward lobes around the particle as shown in Figure 3.3 [3]. Increasing the particle size leads to increased Mie scattering rather than absorption and further results in interference of the scattered lobes.

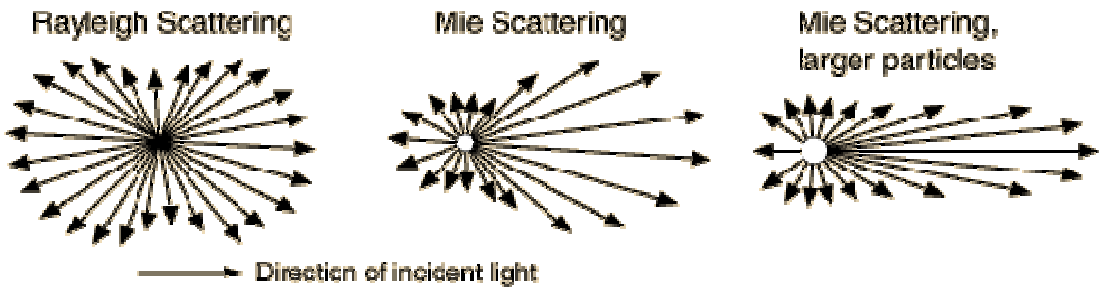

Figure 3.3 Schematic of Rayleigh scattering and Mie scattering [3]

When light of initial intensity I_0 passes through a sample, both absorption and scattering can take place. The transmitted intensity I is a function of the path length l and I_0. Their relationship can be described by the following equations [1], Equation 3.1, 3.4 and 3.5:

$$I\ (l) = I_0 10^{-\varepsilon_{ext} cl} \qquad \text{Equation 3.3 [1]}$$

$$T = I \big/ I_0 = 10^{-\varepsilon_{ext} cl} \qquad \text{Equation 3.4 [1]}$$

$$\varepsilon_{ext} = \varepsilon_{abs} + \varepsilon_{scatter} \qquad \text{Equation 3.5 [1]}$$

where T is the transmittance, ε_{ext} is the extinction coefficient which measures how well the sample scatters and/or absorbs the light, ε_{abs} is the absorption coefficient and $\varepsilon_{\text{scatter}}$ is the scattering coefficient. Both ε_{abs} and $\varepsilon_{\text{scatter}}$ are wavelength dependent and the spectrum is characteristic of the sample to be measured.

It is to be noted that in the case of SWNT suspensions/ solutions, it is difficult to assess the molar concentration. In all cases throughout this work, as-produced mass concentrations are quoted and the extinction/absorption coefficients defined are based on the mass concentration of the dispersion.

3.1.2 UV-Vis-NIR Spectrometer with integrating sphere

The absorbance spectrometer used in this study is a Perkin Elmer Lambda 900 UV-Vis-NIR Spectrometer, shown in Figure 3.4. It is a double-beam, double monochromator ratio recording system with pre-aligned tungsten-halogen and deuterium lamps as sources. The working wavelength is from 175 nm to 3300 nm with an accuracy of 0.08 nm in the UV-Visible region and 0.3 nm in the near infrared region. The spectrometer is equipped with an integrating sphere light collector which enables the differentiation of absorption and scattering, the principle of which is discussed below.

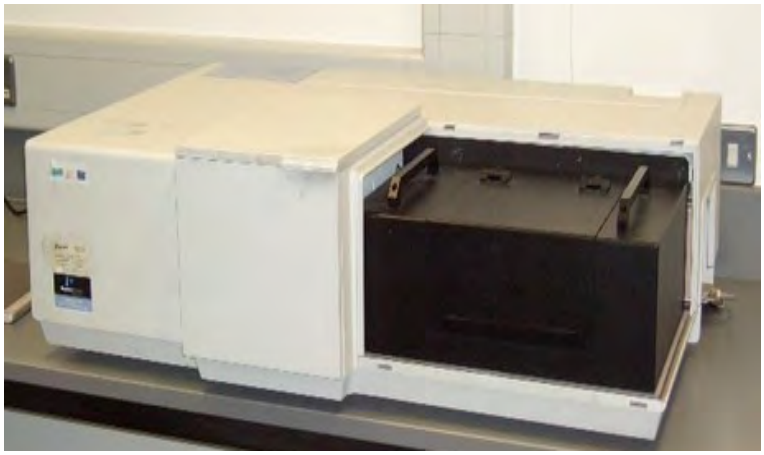

Figure 3.4 Perkin Elmer Lambda 900 UV-Vis-NIR Spectrometer

Figure 3.5 is a diagram of the components of a typical double beam UV-Vis-NIR spectrometer. For all the experimental studies the absorption was measured at all times with a reference sample in a double beam arrangement. Normally the

corresponding pure solvent is used as reference during the characterization of SWNT-solvent dispersions.

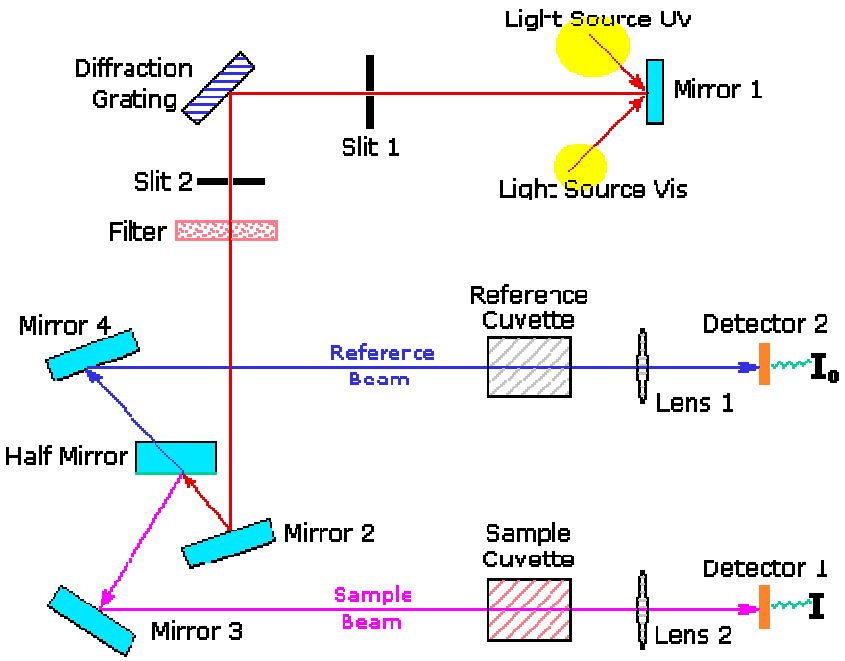

Figure 3.5 Schematic set-up of double beam UV-Vis-NIR spectrometer [4].

The principle of this double beam instrument is that in the sample beam, the light passes through the cuvette containing the sample, and the other beam passes through an identical cuvette containing only solvent. The intensities of these light beams are then measured by electronic detectors and compared. The intensity of the reference beam, which should have suffered little or no light absorption, is defined as I_0. The intensity of the sample beam is defined as I.

If the sample compound does not absorb light of a given wavelength, $I = I_0$. However, if the sample compound absorbs light then I is less than I_0, and the absorption may be presented as transmittance ($T = I/I_0$) or absorbance ($A = \log I_0/I$).

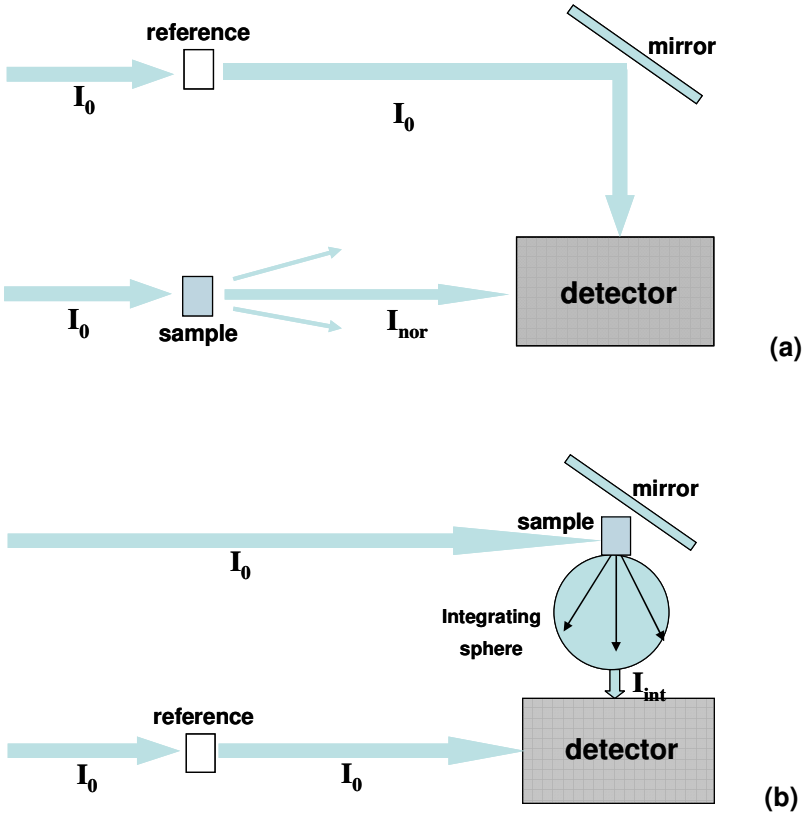

Figure 3.6 Schematic of the different mode of absorbance spectrometer: (a) normal chamber, (b) integrating sphere

However, when scattering happens, the light collected by the detector is only the light which has passed through the sample, and the scattered light is often lost before it reaches the detector. The UV-Vis-NIR spectrometer which was used in this study is equipped with an integrating sphere, by which the scattered light can be collected, giving a more accurate estimate of the absorption of light by the sample material (Figure 3.6).

As the sample is a significant distance from the detector, the absorbance measured from the standard mode of the spectrometer using the normal chamber, A_{nor} (absorbance measured in the normal chamber) contains contributions from scattering and/or absorption

$$A_{nor} = (\varepsilon_{abs} + \varepsilon_{scatter}) \cdot c \cdot l = \varepsilon_{ext} \cdot c \cdot l \qquad \text{Equation 3.6}$$

ε_{abs}, $\varepsilon_{scatter}$, ε_{ext} are defined as above in Section 3.1.1. Utilising the integrating sphere, the scattered light is collected and detected and therefore the absorbance measured (A_{int}) is a more accurate assessment of the true optical absorption.

$$A_{int} = \varepsilon_{abs} \cdot c \cdot l \qquad \text{Equation 3.7}$$

The contributions of absorption and scattering can thus be independently determined as the total extinction coefficient and absorption coefficient can be obtained from the slope of the linear fitting of the absorption in the normal chamber and in the integrating sphere. The efficiency of collection of the scattered radiation is dependent on the angular dispersion and thus in the relative contributions of Rayleigh and Mie scattering. In the case of dispersions of SWNTs, it may be expected that the dominant contribution is from large bundles and thus Mie scattering in the forward direction.

3.1.3 UV-Vis-NIR spectroscopy of SWNTs

UV-Vis-NIR spectroscopy is an analytical technique which is ideally suited for the characterization of SWNTs, because it allows the measurement of the absorption of light in the region of the inter-band electronic transitions. These electronic transitions are the characteristic signature of the SWNT electronic structure and may be observed in the solution or solid state as a function of photon energy [5].

In addition to qualitative characterization of SWNTs [6-9], absorbance spectroscopy has been advanced as an efficient tool for characterization of the stability of SWNTs in surfactant aqueous solution [10], the exfoliation kinetics of arc-discharge and HiPco SWNTs in aqueous surfactant solution [11], and the purity assessment of SWNTs [12]. With reference to the Beer-Lambert law (Equation 3.2), Bahr et al reported a method for determining the dispersion limit of SWNTs in different organic solvents through the extinction at 500nm [13].

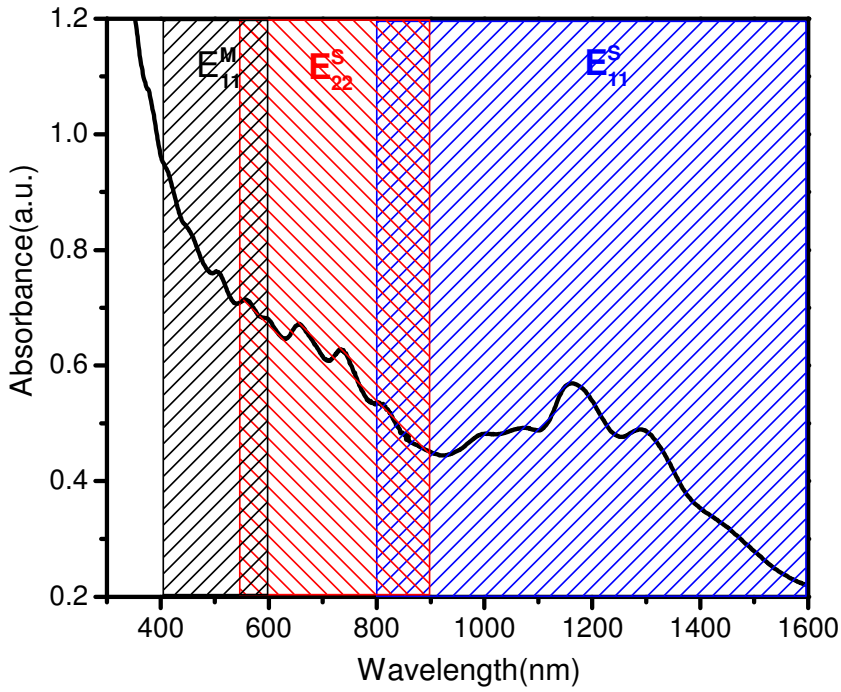

Figure 3.7 Typical optical spectrum of HiPco SWNTs dispersed in *m*-DCB

Figure 3.7 shows a typical absorption spectrum of a sample of (HiPco) SWNTs of mixed electronic character. Following the treatment of Chapter 2, absorbance features between 800 - 1600 nm are assigned to the first inter-band transition $v_1 \rightarrow c_1$ in semiconducting SWNT (S_{11}), whereas the peaks between 550 - 900 nm are assigned to the second inter-band transitions $v_2 \rightarrow c_2$ (S_{22}) again in

semiconducting SWNT. The absorbance features of $v_1 \rightarrow c_1$ (M_{11}) of metallic SWNT are predicted to be located between 400 - 600 nm [14]. The features of SWNTs sit on a strong background of π-plasmon absorption from both SWNTs and carbonaceous impurities [15].

The features observed consist of several van Hove transitions of nanotubes of different diameters. Usually these peaks are not individually resolved. Therefore, the location of these unresolved prominent features in the absorption spectrum to some extent depends on the nanotube diameter distribution in samples. As the transition energy depends on the diameter and electronic properties of the SWNTs (Equation 2.4), many parameters, such as the different growth methods, diameter dispersion and even the purity of the tubes, can affect the shape of the spectra of the tubes, which makes the analysis of the spectra more complicated.

It is expected that the absorbance spectrum of the as prepared dispersion contains contributions from the intrinsic absorption of the nanotubes and scattering from bundles. Indeed, in all cases, it appears that the absorption features sit on a broadband background, in addition to the π-plasmon resonance, which is characteristic of Mie and/or Rayleigh scattering. In order to minimize and evaluate this contribution, the samples were measured using the integrating sphere geometry. Figure 3.8 shows the absorption spectra measured both in the normal chamber (black line) and the integrating sphere (red line) of a sample of concentration 0.02 mg/ml in *o*-DCB. The difference in the recorded absorbance is due to scattering from bundles which is not measured by the normal chamber. The loss of light due to scattering is taken into account as absorption in the case of the normal chamber. The red

spectrum is that as measured using the integrating sphere more closely represents the actual absorption of the bundles and the individual tubes, the loss of light due to scattering having been minimised, and so the absorbance is lower than that measured in the normal chamber. Comparing the two spectra, it can be seen that the extinction in the normal chamber is much higher than that using the integrating sphere, indicating that the extinction due to scattering is significant, and illustrating that a large amount of SWNTs exist in bundles at this concentration.

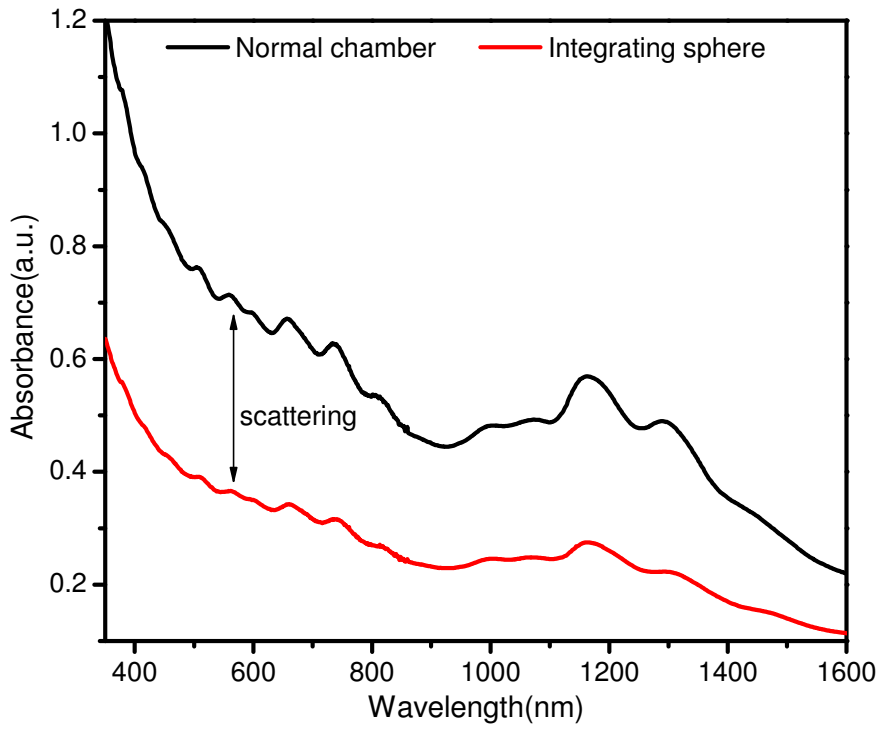

Figure 3.8 Absorption spectra of SWNTs in o-DCB at a concentration of 0.02 mg/ml

3.2 Resonant Raman Spectroscopy

3.2.1 Introduction of Resonant Raman spectroscopy

Resonant Raman spectroscopy is the most widely used technique for the characterization of carbon nanotubes, especially for structural analysis. It is a very powerful method for obtaining qualitative and quantitative information of SWNTs regarding diameter, electronic structure, purity, crystallinity, distinguishing metallic and semiconducting, as well as chirality [16]. It requires very little sample preparation and spectra are obtained in a rapid, less-destructive way.

Raman spectroscopy is a technique to study vibrational, rotational, and other low-frequency modes in a sample. When a material is exposed to a monochromatic light, usually from a laser in the visible, near infrared, or near ultraviolet range, the incoming light interacts with an electron that makes a virtual or real transition to a higher energy level, where the electron interacts with a phonon (via electron-phonon coupling) before making a transition back to the electronic ground state [15]. Figure 3.9 shows the energy level diagram of the states involved in this Raman scattering process [17]. The line thickness is roughly proportional to the signal strength from the different transitions. Through the interaction, the photon is inelastically scattered, either creating (Stokes) or annihilating (anti-Stokes) a phonon (vibration) in the material. The energy of the inelastically scattered light is measured with respect to the laser energy (in cm^{-1}), the energy difference being the vibrational energy. The choice of laser energy (typically in the visible or near-infrared) does not affect the Raman shift, but if the laser energy is resonant with an electronic transition, the Raman

intensity can be increased by many orders of magnitude and the process is said to be resonantly enhanced [15]. Due to the strongly peaked density of states in carbon nanotubes, resonance Raman scattering from nanotubes gives information of the vibrational modes from the Raman shift, as well as the optical transition energy since it is close to the energy of the laser.

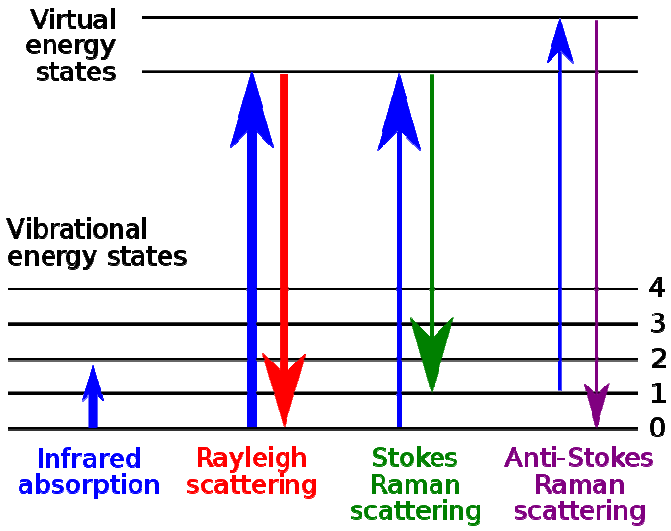

Figure 3.9 Energy level diagrams of the states involved in the Raman signal [17]

Figure 3.10 shows the Raman spectrometer used in this study. The instrument consists of a true confocal microscope system with available laser lines at 475 nm, 533 nm, 660 nm, and 785 nm. All lasers are polarized, enabling measurement of depolarisation ratios and studies of orientation in materials. Light is imaged to a diffraction limited spot (typically 1 micron) via the objective of the microscope. The scattered light is collected by the objective in a confocal geometry, and is dispersed onto an air cooled CCD array by one of four interchangeable gratings, 300 gr/mm, 600 gr/mm, 950 gr/mm, and 1800 gr/mm.

Band analysis in the order of 0.3 cm^{-1} to 1 cm^{-1} is particularly suited to the high resolution mode.

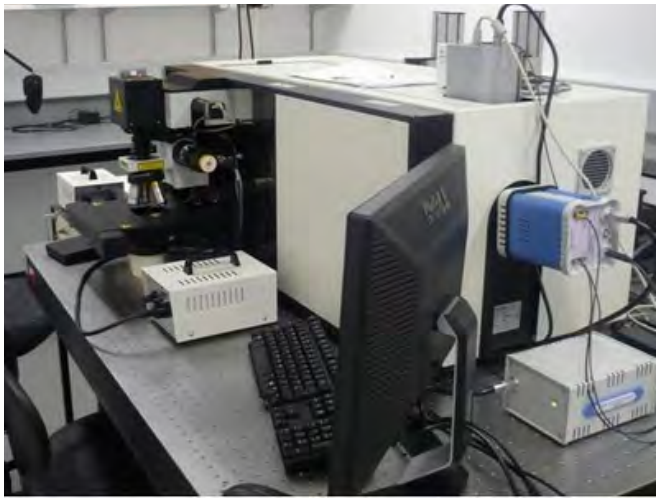

Figure 3.10 Horiba Jobin Yvon LabRAM HR 800 Raman spectrometer

3.2.2 Raman Spectroscopy of SWNTs

When the incident laser energy is close enough to the energy between the van Hove singularities in the valence and conduction bands, a strong resonantly enhanced Raman signal of a single SWNT can be obtained [18]. When a bundle or collection of isolated SWNTs is exposed to the laser line, only those tubes with inter-band transition energies resonant with the excitation energy will contribute strongly to the spectrum. Figure 3.11 shows a typical Raman spectrum of a SWNTs bundle with the excitation energy at 1.88ev (660nm). The most prominent Raman active modes of SWNTs include the radial breathing modes (RBMs), the D-band (D-disorder), the G-band (G-graphite) and the D*-band (second-order Raman scattering from D-band vibrations), which are

located from lower to higher frequency respectively. The RBMs, which arise from the scattering of the isotropic radial expansion of the tube, are unique features of carbon nanotubes. However, other Raman active modes are also observed in graphite, as it is the parent material of carbon nanotubes [15].

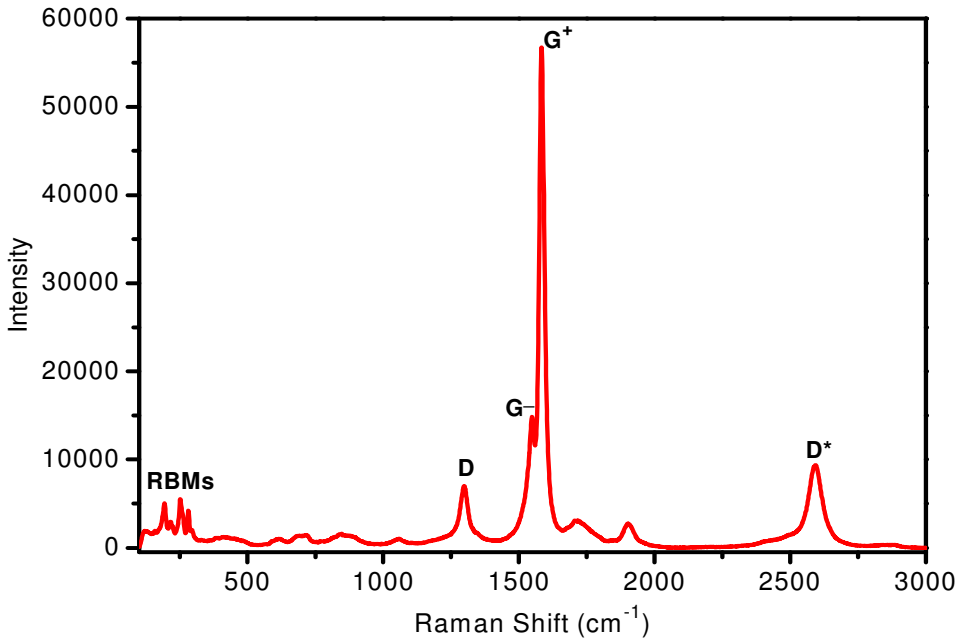

Figure 3.11 Raman spectrum of bundled HiPco SWNTs on quartz substrate excited at 1.88ev.

3.2.2.1 The Radial Breathing Mode (RBM)

RBMs arise from the scattering of light from the radial breathing modes in carbon nanotubes in which the phonon modes are dominated by the radial out-of-plane modes (shown in Figure 3.12). They are normally located in the range of ~100 - 300 cm^{-1}. These features can be used to confirm the presence of carbon nanotubes in a sample as it cannot be observed in other forms of carbon

materials. The frequency of an RBM (ω_{RBM}) sensitively depends on the diameter of the tube d [19] according to the following expression [18]:

$$\omega_{RBM} = A/d + B \qquad \text{Equation 3.8 [18]}$$

where d uniquely relates to the structural indices (n, m) as described in Chapter 2 (Equation 2.2).

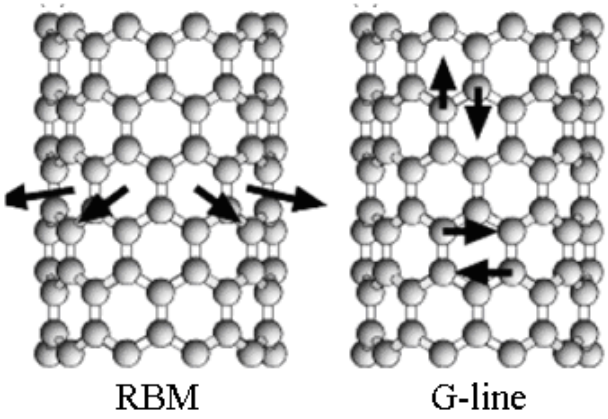

Figure 3.12 Schematic representation of the atomic vibrations for RBM and G-line [20].

A in Equation 3.8 is a constant of proportionality and B is interpreted to be related to the damping of the environment surrounding the tube, due for example to the additional interactions in a bundle [18], on a substrate or dispersed in surfactant, and it is expected to be zero for free standing isolated SWNT [21].

The most important application of resonance Raman spectroscopy in the characterisation of SWNTs is to analyze the diameter distribution of the sample [22, 23] and furthermore to determine the structural assignments of the tubes. The RBM frequencies have thus became the most important feature of a

Raman spectrum and other characteristics can be used to confirm the assignments.

The so-called Kataura plot, shown in Figure 3.13, is well established in the determination of the tube diameter and the associated chiral vectors [21, 24-26].

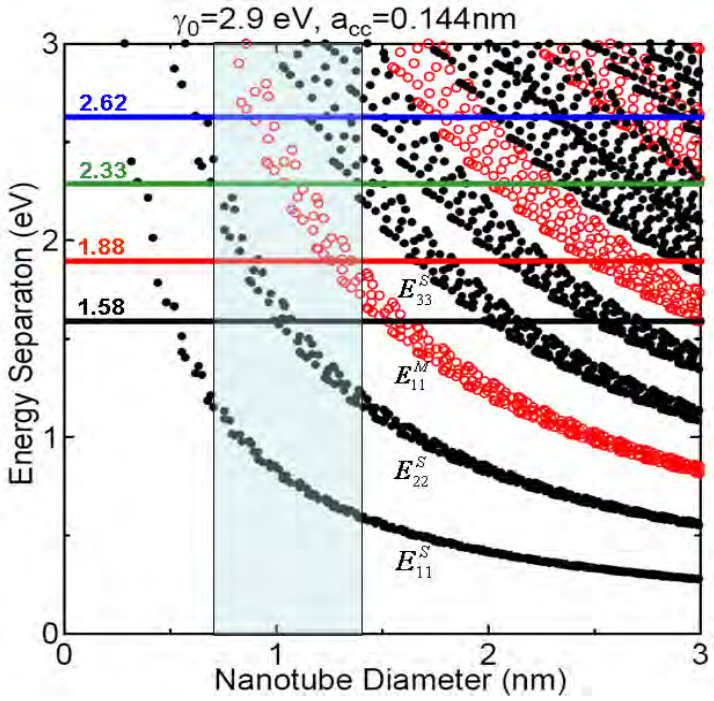

Figure 3.13 Kataura plot [7]. Semiconducting (open circle), Metallic (filled circle). Four horizontal lines indicate the laser energies. Diameter range of the HiPco SWNTs is indicated by the two vertical lines.

At the laser frequencies commonly employed for Raman spectroscopy, carbon nanotubes can be resonant and thus the signal enhanced. According to the resonance theory, only when the excitation energy, *i.e.* the laser energy, is close enough to E_{ii}, will the tube be resonant and give a strong Raman signal [7, 21]. Therefore, it is not surprising to obtain Raman spectra which are dominated by different diameter nanotubes when a given sample of multiple diameters is

excited by different laser energies [24, 26]. Thus, to fully characterize a sample of mixed diameter nanotubes, as broad a range of laser sources as possible should be employed [24]. Figure 3.14 shows the RBM peaks of a single sample containing bundled SWNTs under different excitation energies. It is obvious that the RBM frequencies vary significantly due to the different resonance behaviour of different tubes.

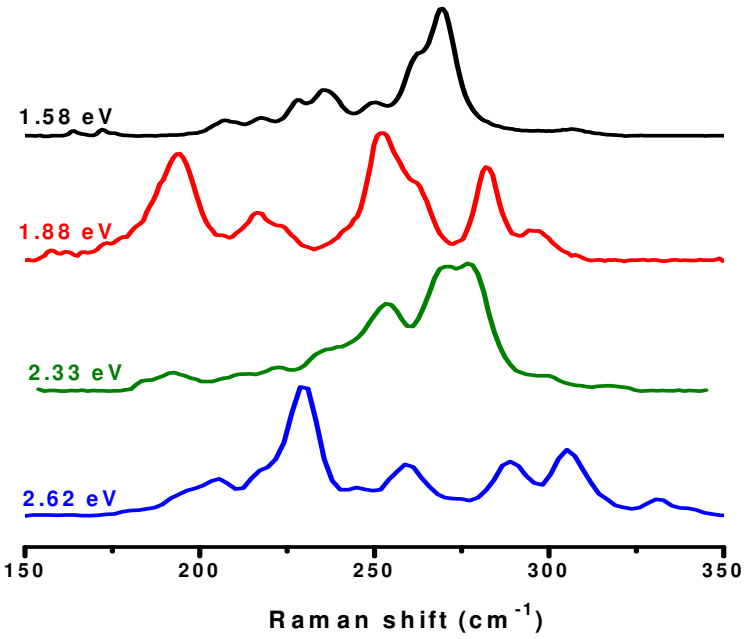

Figure 3.14 RBM frequencies (normalised to the most intense peak) of bundled HiPco SWNTs dispersed on quartz substrate at different excitation energies.

3.2.2.2 The G-band

The G-band comes from the tangential shear mode of the carbon atoms, as shown in Figure 3.12. In graphite, there is one single G-band at ≈ 1580 cm^{-1}. However, in carbon nanotubes, due to the curvature of the graphene sheet, the

G-band is split into two peaks, the lower frequency component (G^-), and the higher frequency component (G^+) [22].

The lineshape of the G-band was predicted to relate to the electronic property of the tube which depends on its structural indices (n, m) [27]. When $(n - m)$ mod 3 = 0, the tubes are metallic, otherwise semiconducting when $(n - m)$ mod 3 = 1 or 2 [27]. The G^+ features of metallic and semiconducting tubes are found to show no significant difference in the frequency and width. But the lineshape of the G^- feature, while Lorentzian for semiconducting tubes, is found to be broadened and down shifted for metallic tubes and to have a characteristic Breit-Wigner-Fano (BWF) lineshape [7, 22]. A BWF lineshape is usually associated with the resonant coupling of phonon modes with electronic continuum states and in SWNTs has been used to identify the presence of metallic nanotubes [16]. More recent studies have demonstrated that while the G^+ and G^- line correspond to the longitudinal optical and transverse optical phonon in semi-conducting nanotubes, the reverse is the case in metallic nanotubes [28, 29]. It has furthermore been demonstrated that in metallic nanotubes, the G^-, Breigt-Wigner-Fano lineshape is a result of coupling of phonons with electron-hole pairs [28]. By combining Rayleigh scattering with Raman resonance profiles, Fouquet *et al* suggested that the G^+ and G^- originate from longitudinal optical phonons of different tubes, G^- being the longitudinal mode of the metallic tube and G^+ the longitudinal mode of the semiconducting tube [30]. Although there are still arguments about the origin of G^+ and G^- bands, it is well accepted that the metallic tube shows a broader and lower G^- feature, and the frequency of G^- is diameter dependent, as shown in Figure 3.15 [31]. Figure 3.16 shows the G-band of the same sample which contains bundled HiPco SWNTs excited at

different laser energies. It is clearly seen that the signal from semi-conducting tubes dominates the spectrum at 1.88 eV. However, the spectrum obtained at 2.33 eV shows a signal characteristic of metallic tubes.

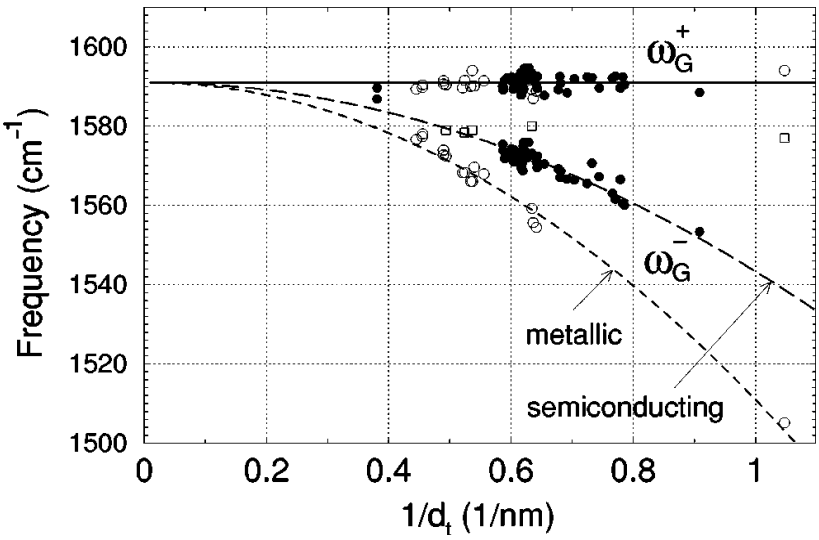

Figure 3.15 Diameter dependence of the G^- frequency in metallic and semi-conducting SWNTs [31].

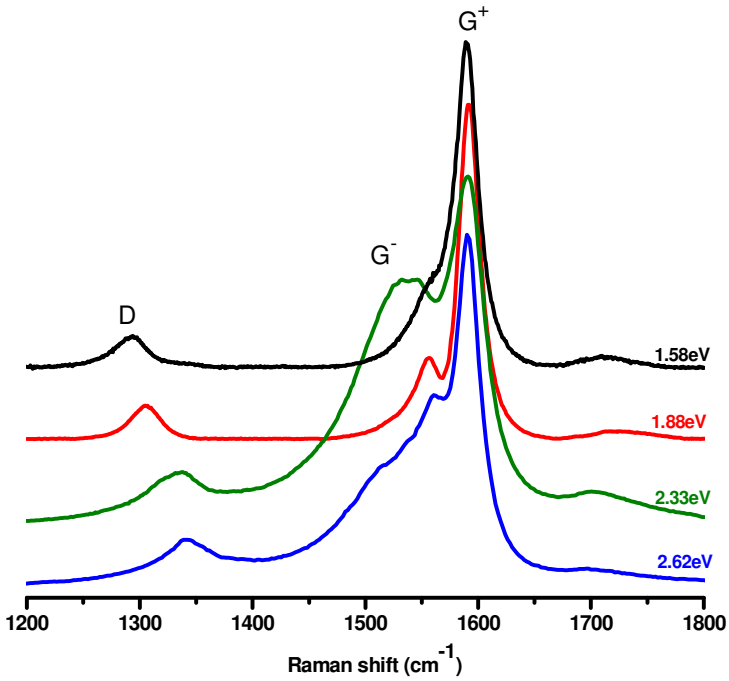

Figure 3.16 G-band frequencies (normalised to G^+) of bundled HiPco SWNTs disposed on quartz substrate at different excitation energies and the corresponding D band.

3.2.2.3 The D and D* modes

The D-band frequency ω_{D}, appearing between 1250 and 1450 cm^{-1}, shows a strong linear dependence on the excitation laser energy (E_{laser}) [32], while the D* band, the overtone of the D-band, is located at 2500 to 2900 cm^{-1}, which is close to twice the frequency of the corresponding ω_{D}.

The D band is called a defect mode because a defect is needed to elastically scatter in order for the process to conserve momentum. The intensity of the D band, related to the number of defects or other symmetry-breaking elements, or the end of a nanotube [18], reflects the quality of the sample, such as the number of defects and impurities. The relative strength and width of the D band also gives a qualitative measurement of how large a fraction of graphitic material and nanotubes with defects are present in the sample [16]. The relative strength of the D band has previously been employed to monitor nanotube damage [33, 34], and in this work it will be employed to investigate the sonication-induced scission of the tubes in Chapters 7 and 8.

The D* band can be regarded as the overtone of the D mode which is an intrinsic property of the nanotube and graphite [18]. The dispersion of the D* band is $\omega_{D^*} \approx 2420\ cm^{-1} + 105\ cm^{-1}/\ E_{laser}$ (eV) [15].

3.3 Atomic Force Microscopy (AFM)

Atomic Force Microscopy (AFM) is one of the most important techniques in nanoscience and nanotechnology, and it is called “the eyes of nanotechnology” [35]. The atomic force microscope is a high-resolution imaging and measurement tool that allows researchers to directly view single atoms or molecules that are only a few nanometers in size, and then produce a three-dimensional map of the sample surface.

Like all other scanning probe microscopies, Atomic Force Microscopy (AFM) utilizes a sharp probe moving over the surface of a sample in a raster scan and three dimensional images of surfaces at atomic resolution can be obtained. The technique uses a tip with an atomically defined point to scan the surface and a laser beam is incident on the top edge of a reflective surface of a tip-cantilever set up and a photo detector with a feedback loop is used to collect the light. The working principle of AFM is illustrated in Figure 3.17.

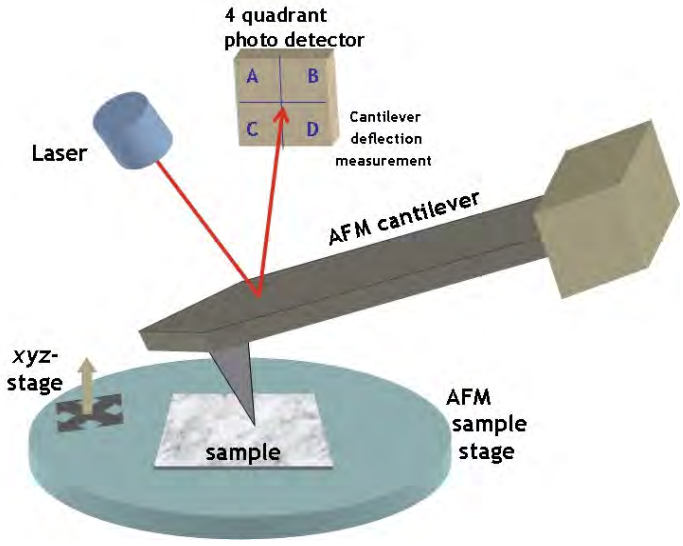

Figure 3.17 Working principle of AFM [36]

When the tip is brought in proximity to a sample surface, forces between the tip and the sample lead to a deflection of the cantilever according to Hooke's law. Depending on the situation, forces that are measured in AFM include mechanical contact, van der Waals, capillary, chemical bonding, electrostatic, magnetic, casimir, solvation forces, etc [1]. The movement of the tip or sample is performed by an extremely precise positioning device made from piezo-electric ceramics, most often in the form of a tube scanner. The scanner is capable of sub-Angstrom resolution in x-, y- and z-directions.

AFM can be operated in three modes, namely the contact mode, non contact mode and the tapping mode depending on the force that is acting between the tip and the sample as shown in the Figure 3.18.

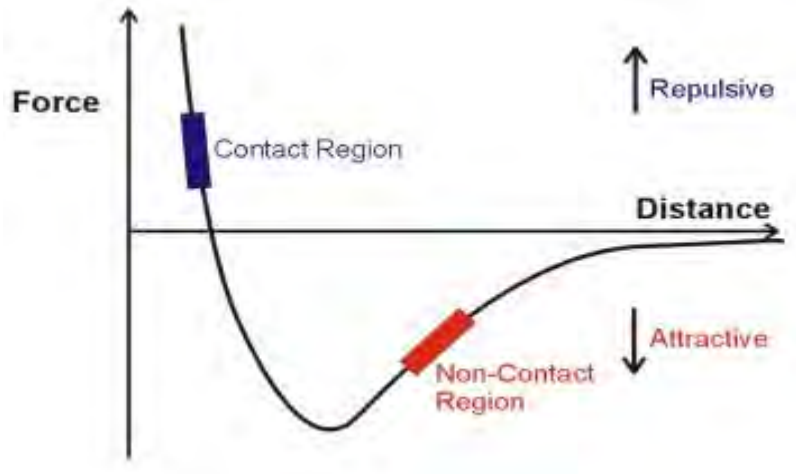

Figure 3.18 The region where the contact and non contact mode can be operated [36]

In the contact mode the tip is positioned in the repulsive region with a mean force of 10^{-9}N and the tip is physically made to touch the surface. As soon as the cantilever is pushed towards the surface it enters into the repulsive region.

Once it enters those regions the cantilever is deflected. This deflection is measured by the photo detector laser set up and the signal is sent to the feed back loop which aims to have a constant force between the tip and the sample by adjusting the deflection.

The non contact mode works in the attractive force regime, whereby a constant height is maintained between the sample and the tip. The tip is made to hover above the sample from a distance of 50 to 150 Å and the imaging is done with the same principle with the photo detector, feed back loop and the piezo elements [36]. However this is a very difficult mode to operate in ambient conditions with the AFM. The thin layer of water contamination which exists on the surface on the sample will invariably form a small capillary bridge between the tip and the sample and cause the tip to "jump-to-contact".

Another common mode of AFM is named the tapping mode, which can be operated in air or other gas environment, as shown in Figure 3.19 [36]. The cantilever is oscillated at its resonant frequency (often hundreds of kilohertz) and positioned above the surface so that it only taps the surface for a very small fraction of its oscillation period [1]. This is still in contact with the sample in the sense defined earlier, but the very short time over which this contact occurs means that lateral forces are dramatically reduced as the tip scans over the surface [1]. In comparison to contact mode, tapping mode is a better choice for the imaging of poorly immobilized or soft samples.

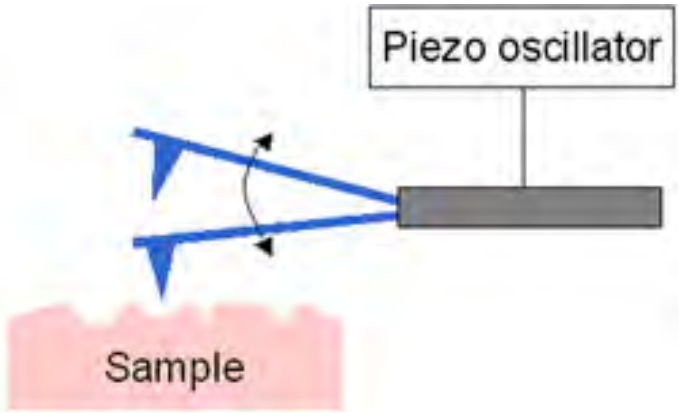

Figure 3.19 Tapping mode of AFM

Phase imaging is a powerful extension of tapping mode AFM that provides nanometer-scale information about surface structure and properties often not revealed by other SPM techniques. By mapping the phase of the cantilever oscillation during the tapping mode scan, phase imaging goes beyond simple topographical mapping to detect variations in composition, adhesion, friction, viscoelasticity and numerous other properties [37].

An Asylum Research MFP-3D-BIO atomic force microscope was used in this study, shown in Figure 3.20. This is a multi mode, high performance microscope, with XYZ scanning range up to 90 µm x 90 µm x 7 µm. The resolution is as low as 0.5 nm [38].

Figure 3.20 MFP-3D-BIO atomic force microscope (Asylum Research) [38]

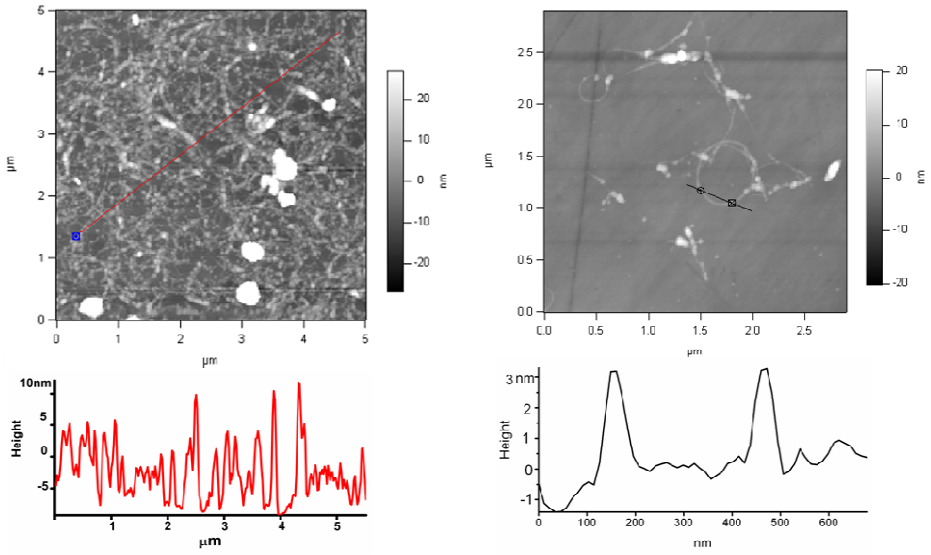

(a) (b)

Figure 3.21 AFM images of (a) bundled and (b) dispersed SWNTs

In order to avoid damage of the nanotube surface, the tapping mode is normally used in the study of carbon nanotubes. Figure 3.21 shows typical AFM images of bundled and dispersed SWNTs on a quartz substrate obtained in the tapping

mode. The bundle size information can be obtained by the height data, and the diameter distribution indicates the degree of dispersion of the SWNT samples.

3.4 Summary

This chapter has provided a brief introduction of the characterization techniques employed in this work, including UV-Vis-NIR spectroscopy, resonant Raman spectroscopy and Atomic Force Microscopy. Employment of these spectroscopic and microscopic techniques with respect to the aims and objectives of this thesis is discussed in the following chapters.

3.5 References

1. Gauglitz, G.; Vo-Dinh, T., Handbook of Spectroscopy. 2003, WILEY-VCH.
2. Tilley, R. J. D., Colour and Optical Properties of Materials: An Exploration of the Relationship Between Light, the Optical Properties of Materials and Colour. 1999, John Wiley & Sons.
3. Borengasser, M.; Hungate, W.S.; Watkins, R., Hyperspectral remote sensing: principles and applications. 2007, CRC Press, Taylor & Francis Group.
4. Khandpur, R.S., Handbook of analytical instruments. 2006, Tata McGraw-Hill publishing company Ltd.

5. Ryabenko, A.G.; Dorofeeva, T.V.; Zvereva, G.I. UV–VIS–NIR spectroscopy study of sensitivity of single-wall carbon nanotubes to chemical processing and Van-der-Waals SWNT/SWNT interaction. Verification of the SWNT content measurements by absorption spectroscopy Carbon 2004, **42**, 1523-1535.

6. Chen, J.; Rao, A.M.; Lyuksyutov, S.; Itkis, M.E.; Hamon, M.A.; Hu, H.; Cohn, R.W.; Eklund, P.C.; Colbert, D.T.; Smalley, R.E.; Haddon, R.C. Dissolution of full-length single-walled carbon nanotubes. Journal of Physical Chemistry B 2001, **105**, 2525-2528.

7. Kataura, H.; Kumazawa, Y.; Maniwa, Y.; Umezu, I.; Suzuki, S.; Ohtsuka, Y.; Achiba, Y. Optical properties of single-wall carbon nanotubes. Synthetic Metals 1999, **103**, 2555-2558.

8. Chen, J.; Hamon, M.A.; Hu, H.; Chen, Y.S.; Rao, A.M.; Eklund, P.C.; Haddon, R.C. Solution properties of single-walled carbon nanotubes. Science 1998, **282**, 95-98.

9. Itkis, M.E.; Niyogi, S.; Meng, M.E.; Hamon, M.A.; Hu, H.; Haddon, R.C. Spectroscopic study of the Fermi level electronic structure of single-walled carbon nanotubes. Nano Letters 2002, **2**, 155-159.

10. Jiang, L.Q.; Gao, L.; Sun, J. Production of aqueous colloidal dispersions of carbon nanotubes. Journal of Colloid and Interface Science 2003, **260**, 89-94.

11. Grossiord, N.; Regev, O.; Loos, J.; Meuldijk, J.; Koning, C.E. Time-dependent study of the exfoliation process of carbon nanotubes in aqueous dispersions by using UV-visible spectroscopy. Analytical Chemistry 2005, **77**, 5135-5139.

12. Landi, B.J.; Ruf, H.J.; Evans, C.M.; Cress, C.D.; Raffaelle, R.P. Purity assessment of single-wall carbon nanotubes, using optical absorption spectroscopy. Journal of Physical Chemistry B 2005, **109**, 9952-9965.

13. Bahr, J.L.; Michael, E.T.M.; Bronikowski, J.; Smalley, R.E.; Tour, J.M. Dissolution of small diameter single-wall carbon nanotubes in organic solvents? Chemical Communications, 2001, 193-194.

14. Nair, N.; Usrey, M.L.; Kim, W.J.; Braatz, R.D.; Strano, M.S. Estimation of the (n,m) concentration distribution of single-walled carbon nanotubes from photoabsorption spectra. Analytical Chemistry 2006, **78**, 7689-7696.

15. Freiman Stephen; Hooker Stephanie; Migler Kalman; Sivaram, A. Measurement Issues in Single Wall Carbon Nanotubes. National Institute of Standard and Technology, Special publication 2008, 960-19.

16. Dresselhaus, M.S.; Dresselhaus, G.; Saito, R.; Jorio, A. Raman spectroscopy of carbon nanotubes. Physics Reports-Review Section of Physics Letters 2005, **409**, 47-99.

17. Long, D.A., The Raman Effect: A Unified Treatment of the Theory of Raman Scattering by Molecules. 2002, John Wiley & Sons Ltd.

18. Thomsen, C.; Reich, S. Raman scattering in carbon nanotubes. Light Scattering in Solids Ix 2007, **108**, 115-235.

19. Rao, A.M.; Richter, E.; Bandow, S.; Chase, B.; Eklund, P.C.; Williams, K.A.; Fang, S.; Subbaswamy, K.R.; Menon, M.; Thess, A.; Smalley, R.E.; Dresselhaus, G.; Dresselhaus, M.S. Diameter-selective Raman scattering from vibrational modes in carbon nanotubes. Science 1997, **275**, 187-191.

20. Jorio, A.; Pimenta, M.A.; Souza, A.G.; Saito, R.; Dresselhaus, G.; Dresselhaus, M.S. Characterizing carbon nanotube samples with resonance Raman scattering. New Journal of Physics 2003, **5**, 139.

21. Jorio, A.; Saito, R.; Hafner, J.H.; Lieber, C.M.; Hunter, M.; McClure, T.; Dresselhaus, G.; Dresselhaus, M.S. Structural (n, m) determination of isolated single-wall carbon nanotubes by resonant Raman scattering. Physical Review Letters 2001, **86**, 1118-1121.

22. Dresselhaus, M.S.; Dresselhaus, G.; Jorio, A.; Souza, A.G.; Saito, R. Raman spectroscopy on isolated single wall carbon nanotubes. Carbon 2002, **40**, 2043-2061.

23. Duesberg, G.S.; Loa, I.; Burghard, M.; Syassen, K.; Roth, S. Polarized Raman spectroscopy on isolated single-wall carbon nanotubes. Physical Review Letters 2000, **85**, 5436-5439.

24. Fantini, C.; Jorio, A.; Souza, M.; Strano, M.S.; Dresselhaus, M.S.; Pimenta, M.A. Optical transition energies for carbon nanotubes from resonant Raman spectroscopy: Environment and temperature effects. Physical Review Letters 2004, **93**, 147406.

25. Telg, H.; Maultzsch, J.; Reich, S.; Hennrich, F.; Thomsen, C. Chirality distribution and transition energies of carbon nanotubes. Physical Review Letters 2004, **93**, 177401.

26. Thomsen, C.; Telg, H.; Maultzsch, J.; Reich, S. Chirality assignments in carbon nanotubes based on resonant Raman scattering. Physica Status Solidi B-Basic Solid State Physics 2005, **242**, 1802-1806.

27. Saito, R.; Fujita, M.; Dresselhaus, G.; Dresselhaus, M.S. Electronic-Structure of Chiral Graphene Tubules. Applied Physics Letters 1992, **60**, 2204-2206.

28. Lazzeri, M.; Piscanec, S.; Mauri, F.; Ferrari, A.C.; Robertson, J. Phonon linewidths and electron-phonon coupling in graphite and nanotubes. Physical Review B 2006, **73**, 155426.

29. Piscanec, S.; Lazzeri, M.; Robertson, J.; Ferrari, A.C.; Mauri, F. Optical phonons in carbon nanotubes: Kohn anomalies, Peierls distortions, and dynamic effects. Physical Review B 2007, **75**, 035427.

30. Fouquet, M.; Telg, H.; Maultzsch, J.; Wu, Y.; Chandra, B.; Hone, J.; Heinz, T.F.; Thomsen, C. Longitudinal Optical Phonons in Metallic and Semiconducting Carbon Nanotubes. Physical Review Letters 2009, **102**, 075501.

31. Jorio, A.; Souza, A.G.; Dresselhaus, G.; Dresselhaus, M.S.; Swan, A.K.; Unlu, M.S.; Goldberg, B.B.; Pimenta, M.A.; Hafner, J.H.; Lieber, C.M.; Saito, R. G-band resonant Raman study of 62 isolated single-wall carbon nanotubes. Physical Review B 2002, **65**, 155412.

32. Pimenta, M.A.; Jorio, A.; Brown, S.D.M.; Souza, A.G.; Dresselhaus, G.; Hafner, J.H.; Lieber, C.M.; Saito, R.; Dresselhaus, M.S. Diameter dependence of the Raman D-band in isolated single-wall carbon nanotubes. Physical Review B 2001, **6404**, 041401.

33. Giordani, S.; Bergin, S.D.; Nicolosi, V.; Lebedkin, S.; Kappes, M.M.; Blau, W.J.; Coleman, J.N. Debundling of single-walled nanotubes by dilution: Observation of large populations of individual nanotubes in amide solvent dispersions. Journal of Physical Chemistry B 2006, **110**, 15708-15718.

34. Osswald, S.; Flahaut, E.; Ye, H.; Gogotsi, Y. Elimination of D-band in Raman spectra of double-wall carbon nanotubes by oxidation. Chemical Physics Letters 2005, **402**, 422-427.

35. Galatsis, K. The Eyes and Ears of Nanotechnology. Nanotechnology Now, Jan 20th 2009.

36. Hawkes, P.W., Advances in Imaging and Electron Physics. 2005, Elsevier Academic Press.

37. Babcock, K.L.; Prater, C.B. Phase Imaging: Beyond Topography. Veeco Instruments Inc. 2004.

38. Delzeit, L.; McAninch, I.; Cruden, B.A.; Hash, D.; Chen, B.; Han, J.; Meyyappan, M. Growth of multiwall carbon nanotubes in an inductively coupled plasma reactor. Journal of Applied Physics 2002, **91**, 6027-6033.

CHAPTER 4
DISPERSION OF SWNTS IN CHLORINATED AROMATIC SOLVENTS

Adapted from "**Effects of chlorinated aromatic solvents on the dispersion of HiPco SWNTs**" ***Phys. Stat. Sol. (b).*** **2008, 245, 1947.**

Authors: Qiaohuan Cheng, Sourabhi Debnath, Elizabeth Gregan, Hugh J. Byrne

4.1 Introduction

Since their discovery, different methods, including the assistance of surfactant [1, 2], covalent and non-covalent side wall modification [3, 4], and dispersion in a range of organic solvents [5-7] have been explored to yield stable SWNT dispersions. Compared to other dispersion methods, successful stable dispersions of as-produced SWNTs with organic solvents can avoid the modification of the pristine properties of SWNTs and the introduction of a third component to the system. Therefore, the formation of stable dispersions of SWNTs in a suitable solvent is desirable to enable more accurate solution-phase analyses, processing and applications. A systematic study of a series of alkyl amide solvents has elucidated some structural relationships determining the dispersion of as-produced and purified laser-generated SWNTs, the favourable interaction between SWNTs and alkyl amide solvents being attributed to the highly polar π system and optimal geometries (appropriate bond

lengths and bond angles) of the solvent structures [7]. However, chlorinated aromatic solvents have been reported to be more effective solvents [6], and *o*-DCB as a good dispersive agent for SWNTs has been investigated extensively [8-11]. The possible reasons for its effectiveness are based on the strong π-π interaction between the aromatic solvent molecule and nanotube surface electrons, indicated in Figure 4.1. Although the interaction of *o*-DCB and SWNT has been investigated extensively, a systematic study of aromatic solvents is still lacking.

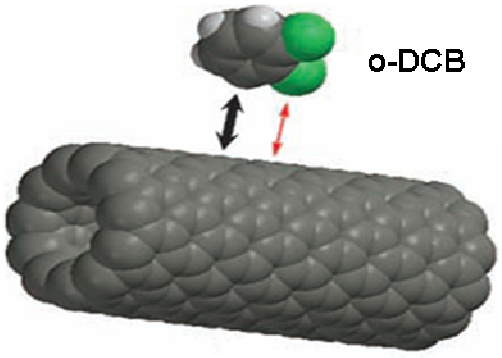

Figure 4.1 Molecular-modelling schematic illustrating the interaction of a SWNT with *o*-DCB, The interactions involve π-orbital (black arrow) and dipole-dipole (red arrow) interactions (the line width indicates the degree of strength). Color coding of atoms: C, gray; H, white; Cl: green. Reproduced from reference [6].

Motivated by this, a systemic study of the dispersion of as-produced HiPco SWNTs in chlorinated aromatic solvents, namely monochlorobenzene (MCB), *ortho*-dichlorobenzene (*o*-DCB), *meta*-dichlorobenzene (*m*-DCB) and 1, 2, 4-trichlorobenzene (TCB), has been conducted and is presented in this chapter. The molecular structures of the solvents are shown in Figure 4.2 and 3-D surface structures are shown in Figure 4.3. The dispersions are characterized using UV-Vis-NIR absorption spectroscopy, a widely used technique in the

qualitative [12] and quantitative [8, 13] characterization of SWNTs. Correlated with the Beer-Lambert law, a concentration dependent study of the absorption enables the calculation of extinction coefficients and dispersion limits of SWNTs in the respective solvents [5, 7]. The Beer-Lambert law is most applicable in mono-disperse molecular solutions. In most cases, however, it is more appropriate to consider SWNT dispersions to be “suspensions” rather than “solutions” and due to the presence of large bundles, the scattering of the light cannot be ignored. In this study, UV-Vis-NIR absorption spectroscopy with the aid of an integrating sphere in a double beam spectrometer, as described in Section 3.1.2, is employed which enables an estimation of the scattering contribution of the extinction and a more accurate evaluation of the SWNTs absorption. The absorption of the dispersion is monitored as a function of sonication time for *o*-DCB, indicating efficient sonication is required for preparing stable SWNT dispersions. Concentration dependent absorption studies are employed to identify transitions from dispersions of bundles to isolated tubes and enable a critical comparison of the chosen solvents.

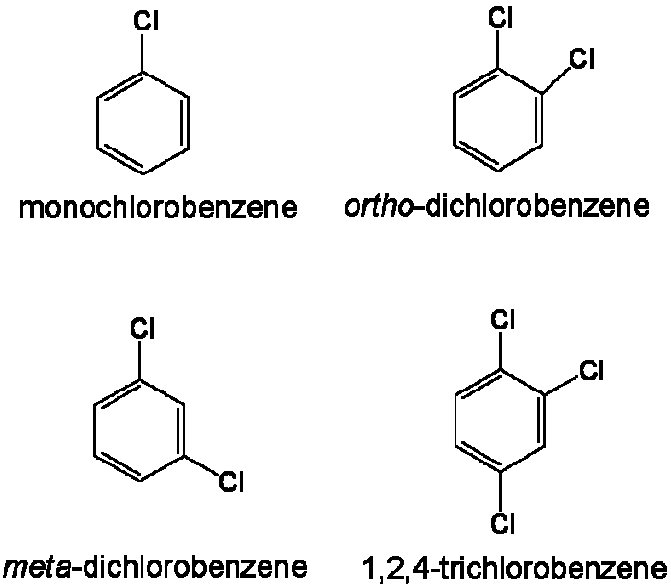

Figure 4. 2 Molecular structures of the chlorinated aromatic solvents

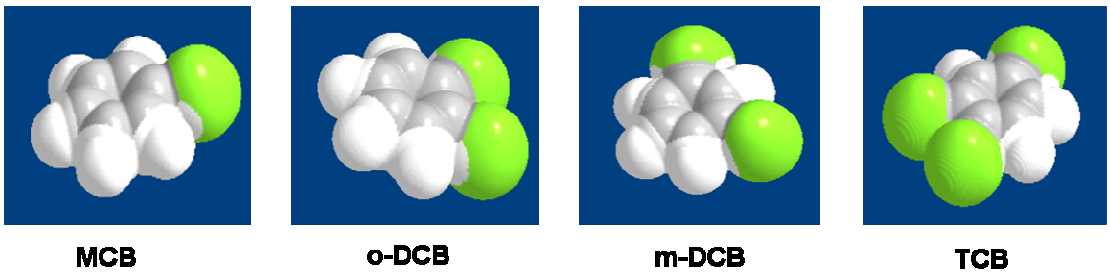

Figure 4.3 3-D surface structures of the solvents. Colour coding of atoms: C, gray; H, white, Cl, green.

4.2 Experimental

Singe-walled carbon nanotubes (HiPco) were purchased from Carbon Nanotechnologies Inc., and used as supplied (batch no. PO341). MCB, *o*-DCB, *m*-DCB, and TCB were obtained from Sigma-Aldrich Ireland Ltd, and used as received.

4.2.1 Sonication time

o-DCB was chosen as solvent for the optimisation of the sonication time. 1.6 mg SWNTs was dispersed in 40ml *o*-DCB (0.04 mg/ml). This initial dispersion was sonicated for 20s using a high-power ultrasonic tip processor (Ultrasonic processor VCX 750 W) at 26% as the power output. The dispersion was then immediately divided into 8 bottles, each sample containing 5 ml. The samples were then sonicated to make a series with different sonication times from 20s to 160s. The samples were allowed to settle for 2 days, and then the supernatant was carefully withdrawn for characterization by UV-Vis-NIR spectroscopy.

4.2.2 SWNT-solvent dispersions preparation

Dispersions of pristine HiPco nanotubes were prepared in all solvents at a maximum nanotube concentration of ~ 0.21 mg/ml. The initial dispersions were tip sonicated for 20 s using the same tip processor at 26% power output and then immediately serially diluted to produce a range of dispersions with concentrations from 0.21 ~ 0.001 mg/ml. Then all the samples were sonicated for another 100 s (the determination of this time will be discussed in Section 4.3), so each sample received the same sonication treatment. Immediately before measurement all samples were vigorously shaken such that the effect of the sonication process on the dispersion of bundles and also the effectiveness of the integrating sphere in removing the contribution of scattering could be

assessed. All dispersions were subsequently centrifuged at 3000 rpm (~945 g) (ECONOSPIN Sorvall Instruments) for 60 minutes. The supernatant was then carefully extracted for measurement.

In all cases, it is difficult to assess the actual final concentration of the sample. For the purposes of optimisation of preparation techniques and comparison of solvents, consistent with previous works [2, 5, 14, 15], as prepared concentrations are quoted.

4.2.3 Optical absorption spectroscopy

Before centrifugation, UV-Vis-NIR absorption (Perkin Elmer Lambda 900, equipped with an integrating sphere, Spectralon as inner coating) measurements were performed in both the normal chamber and integrating sphere as described in Section 3.1.2. After centrifugation, the supernatant was again characterized in the normal chamber. 10 mm quartz cuvettes were used for all the measurements.

4.3 Results and discussion

In order to investigate the effect of sonication time on the dispersion of SWNTs in organic solvents, a series of samples with the same initial concentration but different sonication times was prepared.

Shown in Figure 4.4 (a) is a picture of the dispersions of SWNTs in o-DCB at a prepared concentration of 0.04mg/ml with different sonication times. The corresponding optical absorbance of the supernatant at 660 nm was plotted as a function of sonication time, and is represented in Figure 4.4 (b). The optical absorption spectrum of SWNT samples spans the UV-Vis-NIR and 660 nm was chosen for comparison with other works [2, 5]. Peak intensities were read directly from the as measured absorption spectrum.

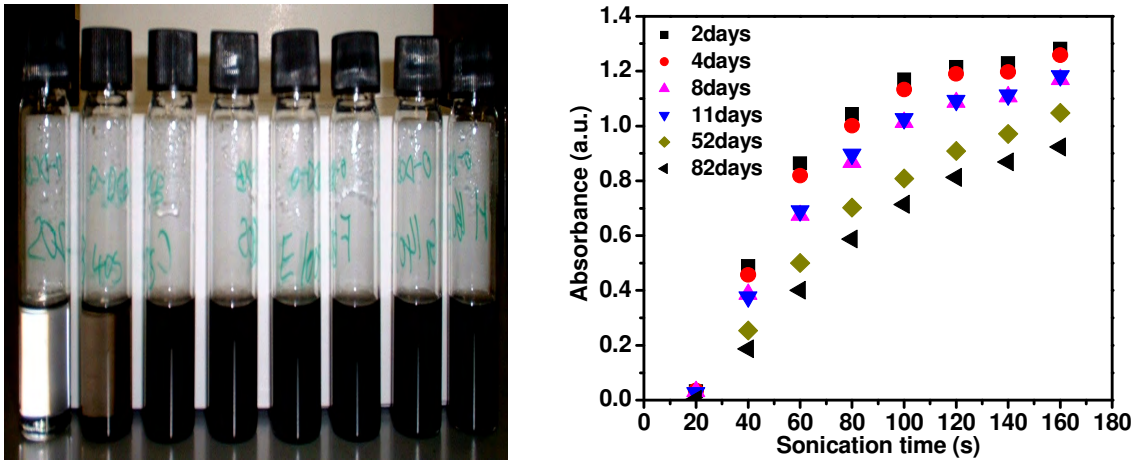

Figure 4.4 (a) Picture of 0.04 mg/ml SWNT/o-DCB dispersions with different sonication time, left to right, 20 s, 40 s, 60 s, 80 s, 100 s, 120 s,140 s and 160 s. (b) Sonication time dependence of the absorption of SWNT/o-DCB dispersions (supernatant) at 660 nm.

The supernatant of the dispersion which was only sonicated for 20 s was colourless and the optical absorption was extremely low, indicating that most of the SWNTs precipitated from the dispersion. It is assumed that insufficient sonication did not provide enough energy to disperse the SWNTs bundles into isolated tubes or even small ropes. As the sonication time was increased, the colour of the supernatant became progressively brown, dark brown and black.

The increasing absorption indicates increasing dispersion of the SWNTs. However, the absorption of the dispersion did not change dramatically after sonication for 120 s, indicating that the supernatant was saturated. Although the sonication time was only optimized in *o*-DCB, for all subsequent measurements in all solvents, 120 s total sonication time was used for preparing all the samples.

Figure 4.4 (b) also shows that the initial supernatant was not a stable solution. After a certain time, the larger bundles precipitated. Most bundles precipitate from the supernatant within the first 8 days after dilution and the sedimentation rate is significantly reduced although precipitation continues up to 82 days.

As the solution phase dispersions of SWNTs normally contain large bundles, the scattering of light cannot be ignored. It has been reported that the use of an integrating sphere is an effective technique of measuring the scattering by the bundles in SWNT/surfactant aqueous systems yielding an accurate absorption of the SWNT dispersions [2].

The double beam UV-Vis-NIR spectrometer which was used in this study (Section 3.1.2) is equipped with an integrating sphere, by which the scattered light can be collected, giving a more accurate estimate of the absorption of light by the sample material (Figure 3.6). It has been demonstrated to be effective in minimizing the contribution of scattering to the total extinction without the need for centrifugation [2].

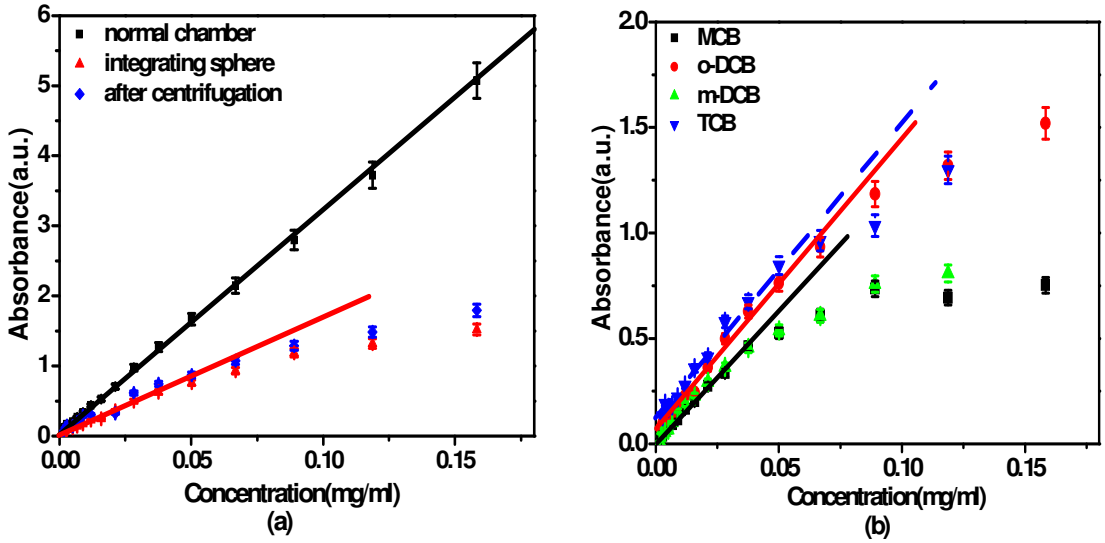

Figure 4.5 (a) Plot of the absorbance at 660nm in SWNT/o-DCB dispersion versus concentration. (b) Concentration dependence of the absorbance in the integrating spheres (data from Figure 4.5 (a)).

Figure 4.5 (a) shows the concentration dependence of the absorbance of SWNT/*o*-DCB dispersions. The absorbance measured in the normal chamber is almost linearly dependent on the concentration over the whole studied range, which is in agreement with the Beer-Lambert law. However, the absorbance measured in the integrating sphere demonstrates linearity only up to a concentration of ~ 0.07 mg/ml indicating the dominance of scattering above this concentration.

The data measured in the integrating sphere are similar to the absorption after centrifugation, indicating that the integrating sphere is an effective technique for removing the scattering effect of bundles and measures the true absorbance of the dispersions. Both of the plots show agreement with the Beer-Lambert law at low concentrations.

Shown in Figure 4.5 (b) are the plots of the absorbance in the integrating sphere in the four solvents. The straight lines are guides to the eye. The deviation from linearity is assumed to be due to the π-π stacking interaction of SWNTs, as commonly occurs in organic molecules [16]. In o-DCB dispersions, aggregation takes place at a concentration of ~ 0.07 mg/ml, whereas in the cases of MCB and *m*-DCB, the data deviates from linearity at a concentration of ~ 0.04 mg/ml, and at ~ 0.05 mg/ml in TCB dispersions.

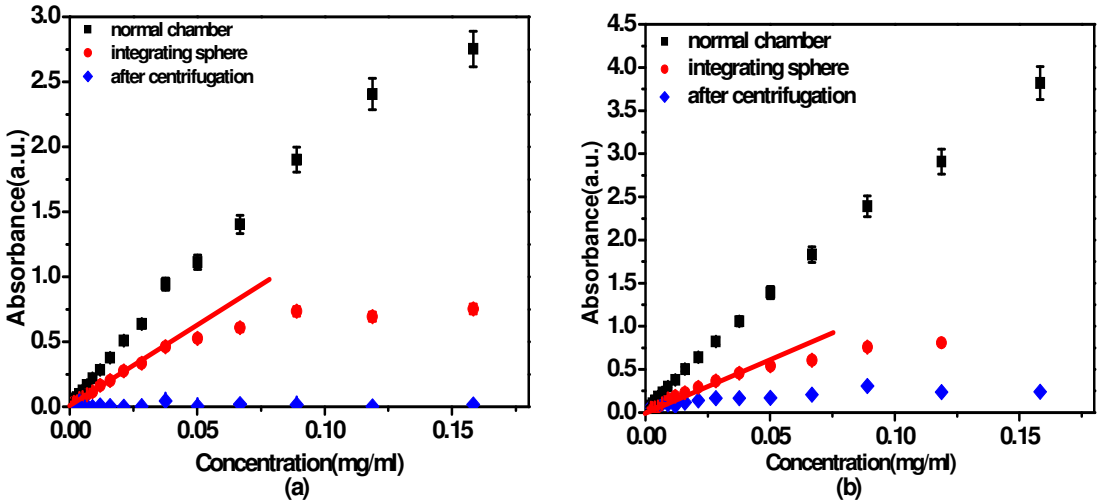

Figure 4.6 Plot of the absorbance at 660nm versus concentration in (a) MCB and (b) *m*-DCB dispersion.

Figure 4.6 shows the concentration dependence of the absorbance of MCB and *m*-DCB dispersions. Comparing the data before and after centrifugation in Figure 4.6 (a), it can be clearly seen that although the deviation from linearity takes place at a concentration of ~0.04 mg/ml, the dispersion formed is not stable. Very few SWNTs stay in suspension after centrifugation, giving an extremely low absorbance.

The absorbance in the integrating sphere is much higher than that after centrifugation, indicating that sonication dispersed the SWNTs into small ropes or even isolated tubes. However, the interaction between SWNTs and MCB molecules is not sufficient to keep the tubes in the dispersion and centrifugation accelerates the aggregation and sedimentation.

In the cases of *m*-DCB and TCB, similar behaviour was observed, but the difference between the data in the integrating sphere and after centrifugation is smaller, indicating that these two solvents are more effective than MCB, but less than *o*-DCB. The absorbance measured in the normal chamber comes from the absorption of SWNTs as well as the scattering of the bundles. In the integrating sphere the scattered light is collected and the measured absorbance is due to absorption only. The fraction of the scatter, $\chi_{scatter}$, can be calculated by the following equation:

$$\chi_{scatter} = \frac{A_{nor} - A_{\mathrm{int}}}{A_{nor}} \qquad \text{Equation 4.1}$$

where A_{nor} and A_{int} are the absorbance at 660nm in the normal chamber and the integrating sphere, respectively.

Giordani *et al.* reported a method to determine the dispersion limit by the calculation of the mass fraction of aggregates [5]. From the difference between the absorbance before and after centrifugation, the mass fraction of aggregates as a function of concentration can be estimated from

$$\chi_{agg} = \frac{A_{before} - A_{after}}{A_{before}} \qquad \text{Equation 4.2}$$

where A_{before} is the absorbance at 660nm in the normal chamber before centrifugation, (*i.e.* A_{nor}), and A_{after} is the data measured from the supernatant after centrifugation.

The mass fractions of the scattering and aggregation are plotted as a function of the prepared concentration, and are shown in Figure 4.7.

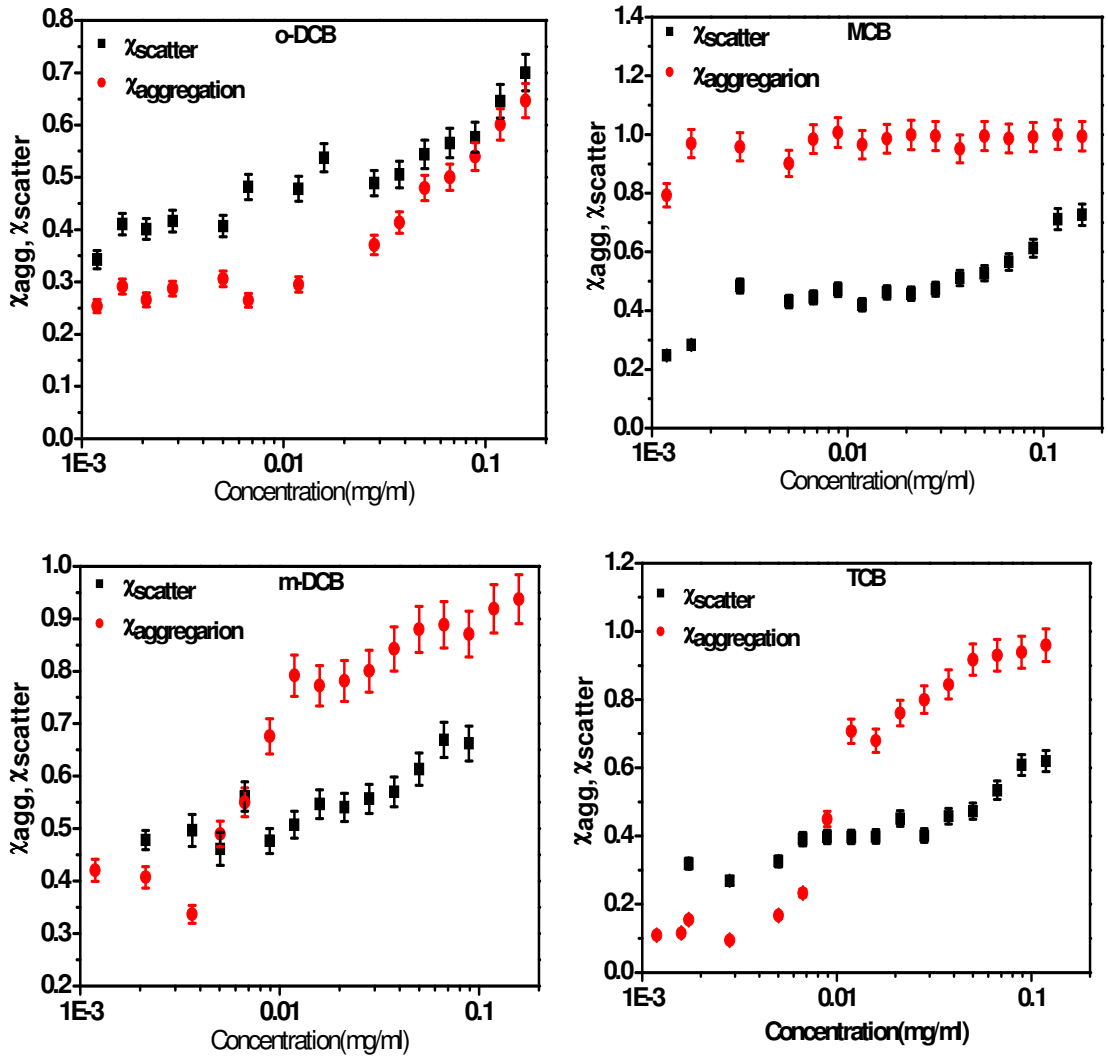

Figure 4.7 Scattering fraction and aggregation mass fraction in different solvents

In the aggregation mass fraction plot, the concentration at which the aggregation dominates the dispersion is considered to be the dispersion limit [5].

In the case of *o*-DCB, it shows that the aggregation takes place at ~ 0.015 mg/ml. The scattering plot for *o*-DCB shows the same trend and the value is very close to the aggregation fraction. This behaviour indicates that both the integrating sphere and centrifugation perform the same function in removing the effect of bundles in *o*-DCB dispersion, which is demonstrated to be a good dispersion agent for SWNTs. However, the aggregation mass fraction plot for MCB shows that nearly all the tubes stay in bundles over the whole concentration range studied. There is also a significant difference between the scattering fraction and aggregation mass fraction, indicating the instability of SWNT/MCB dispersions. From the plot of aggregation mass fraction, the dispersion limit of SWNTs in MCB is found to be lower than 0.001 mg/ml.

In the cases of *m*-DCB and TCB, similar behaviour is observed and the dispersion limit can be concluded to be around 0.004 mg/ml and 0.005 mg/ml respectively. The dispersion limits in the four solvents as determined from the aggregation mass fraction plots have a sequence of o-DCB (0.015 mg/ml) > TCB (0.005 mg/ml) > *m*-DCB (0.004 mg/ml) >>MCB (<0.001 mg/ml), and vary over a wide range.

It is expected that the π-orbital interaction between the SWNT side wall and aromatic solvents plays a significant role in obtaining stable dispersions [7], but this interaction should not differ significantly among the solvent family used here, indicating that π-π stacking interactions between SWNTs and the solvent molecules is not the only consideration for obtaining stable dispersions.

A simple model supported by experiment results suggests that successful solvents for SWNTs are those with surface tensions close to that of graphite, ~

40 mJ/m^2 [15]. The dispersion limits of SWNTs in the solvents in this study do not conform to such a model, however. The dispersion limit of SWNTs in *o*-DCB (surface tension: 36.61 mJ/m^2) is much higher than that in *m*-DCB (surface tension: 36.01 mJ/m^2), indicating that the dispersion limit of SWNTs is not simply related to surface tension of the solvent.

The Hildebrand solubility parameter which correlates to the sum total cohesive energy density is not significantly different for the four solvents (*o*-DCB: 20.5 $MPa^{1/2}$, TCB: 20.3 $MPa^{1/2}$, *m*-DCB: 20.1 $MPa^{1/2}$, MCB: 19.4 $MPa^{1/2}$) [17]. However, the components that make up those individual totals are different (dielectric constant: *o*-DCB: 10.36, TCB: 4.15, *m*-DCB: 5.16, MCB: 5.74) [17]. The slight disparities in polar contributions may be one of the factors responsible for the considerable differences in solubility behaviour. As the solvent Hansen solubility parameters tell the different components of the total cohesive energy density, their use might be more appropriate to investigate the dispersiblity of SWNTs in organic solvents.

Comparing the deviation points from the data measured in the integrating sphere and the dispersion limit in each sample concluded from the aggregation mass fraction, a significant offset is observed. For example, the absorbance in *o*-DCB deviates from the Beer Lambert law at a concentration of ~0.07 mg/ml, whereas the dispersion limit is found to be ~0.015 mg/ml. This phenomenon is also apparent in Reference [5], but no explanation was offered. The reason for this offset might be due to the different effect of aggregation on scattering and absorption. For example, when two SWNTs are present in a bundle, the size is doubled and the scattering cross-section increased. However the tangential

overlap of the π electron clouds is small and the effect on the absorption should be minimal. The maximum change in absorbance of an individual nanotube is reached when all nearest neighbour positions in a bundle are occupied.

Therefore, use of the integrating sphere is a more accurate means to calculate the absorption coefficient of SWNTs in solvent. However, centrifugation is more applicable to obtain the dispersion limit of SWNTs in different solvents.

4.4 Summary

The capability of a series of chlorinated aromatic solvents to disperse and solubilise HiPco SWNTs has been evaluated. Stable dispersions of SWNTs have been demonstrated in some of these solvents. Although the effect of sonication time was only investigated in one solvent, the result shows that it is of great importance in the preparation of stable SWNT dispersions.

A UV-Vis-NIR spectrometer equipped with an integrating sphere enables the measurement of the contribution of scattering, which is due to the suspended bundles in the solution. Significant difference in the efficacy of the solvents measured to disperse SWNTs was observed. No clear structure-property relationships are apparent. The similarity in structure between SWNTs and the aromatic solvent molecules is not the dominant factor and no correlation with surface energies is observed, and a more in depth analysis of solubility parameters is warranted.

4.5 References

1. Matarredona, O.; Rhoads, H.; Li, Z.R.; Harwell, J.H.; Balzano, L.; Resasco, D.E. Dispersion of single-walled carbon nanotubes in aqueous solutions of the anionic surfactant NaDDBS. Journal of Physical Chemistry B, 2003, **107**, 13357-13367.
2. Priya, B.R.; Byrne, H.J. Investigation of Sodium Dodecyl Benzene Sulphonate Assisted Dispersion and Debundling of Single Wall Carbon Nanotubes. J. Phys. Chem. C, 2008, **112**, 332-337.
3. Hamon, M.A.; Chen, J.; Hu, H.; Chen, Y.S.; Itkis, M.E.; Rao, A.M.; Eklund, P.C.; Haddon, R.C. Dissolution of single-walled carbon nanotubes. Adv. Mater., 1999, **11**, 834-840.
4. Kuzmany, H.; Kukovecz, A.; Simon, F.; Holzweber, A.; Kramberger, C.; Pichler, T. Functionalization of carbon nanotubes. Synthetic metals, 2004, **141**, 113-122.
5. Giordani, S.; Bergin, S.D.; Nicolosi, V.; Lebedkin, S.; Kappes, M.M.; Blau, W.J.; Coleman, J.N. Debundling of single-walled nanotubes by dilution: Observation of large populations of individual nanotubes in amide solvent dispersions. Journal of Physical Chemistry B, 2006, **110**, 15708-15718.
6. Kim, D.S.; Nepal, D.; Geckeler, K.E. Individualization of single-walled carbon nanotubes: Is the solvent important? Small, 2005, **1**, 1117-1124.
7. Landi, B.J.; Ruf, H.J.; Worman, J.J.; Raffaelle, R.P. Effects of alkyl amide solvents on the dispersion of single-wall carbon nanotubes. Journal of Physical Chemistry B, 2004, **108**, 17089-17095.

8. Bahr, J.L.; Mickelson, E.T.; Bronikowski, M.J.; Smalley, R.E.; Tour, J.M. Dissolution of small diameter single-wall carbon nanotubes in organic solvents? Chem. Commun., 2001193-194.

9. Detriche, S.; Zorzini, G.; Colomer, J.F.; Fonseca, A.; Nagy, J.B. Application of the Hansen Solubility Parameters Theory to Carbon Nanotubes. Journal of Nanoscience and Nanotechnology, 2008, **8**, 6082-6092.

10. Fagan, S.B.; Girao, E.C.; Mendes, J.; Souza, A.G. First principles study of 1,2-dichlorobenzene adsorption on metallic carbon nanotubes. International Journal of Quantum Chemistry, 2006, **106**, 2558-2563.

11. Fagan, S.B.; Souza, A.G.; Lima, J.O.G.; Mendes, J.; Ferreira, O.P.; Mazali, I.O.; Alves, O.L.; Dresselhaus, M.S. 1,2-dichlorobenzene interacting with carbon nanotubes. Nano Letters, 2004, **4**, 1285-1288.

12. Chiang, I.W.; Brinson, B.E.; Huang, A.Y.; Willis, P.A.; Bronikowski, M.J.; Margrave, J.L.; Smalley, R.E.; Hauge, R.H. Purification and characterization of single-wall carbon nanotubes (SWNTs) obtained from the gas-phase decomposition of CO (HiPco process). Journal of Physical Chemistry B, 2001, **105**, 8297-8301.

13. Attal, S.; Thiruvengadathan, R.; Regev, O. Determination of the concentration of single-walled carbon nanotubes in aqueous dispersions using UV-visible absorption spectroscopy. Analytical Chemistry, 2006, **78**, 8098-8104.

14. Giordani, S.; Bergin, S.; Nicolosi, V.; Lebedkin, S.; Blau, W.J.; Coleman, J.N. Fabrication of stable dispersions containing up to 70% individual

carbon nanotubes in a common organic solvent. Physica Status Solidi B-Basic Solid State Physics, 2006, **243**, 3058-3062.

15. Bergin, S.D.; Nicolosi, V.; Streich, P.V.; Giordani, S.; Sun, Z.Y.; Windle, A.H.; Ryan, P.; Niraj, N.P.P.; Wang, Z.T.T.; Carpenter, L.; Blau, W.J.; Boland, J.J.; Hamilton, J.P.; Coleman, J.N. Towards solutions of single-walled carbon nanotubes in common solvents. Advanced Materials, 2008, **20**, 1876-1881.

16. Gazit, E. A possible role for pi-stacking in the self-assembly of amyloid fibrils. Faseb Journal, 2002, **16**, 77-83.

17. Abboud, J.L.M.; Notario, R. Critical compilation of scales of solvent parameters. Part I. Pure, non-hydrogen bond donor solvents - Technical report. Pure and Applied Chemistry, 1999, **71**, 645-718.

CHAPTER 5
SOLVENT SOLUBILITY PARAMETERS AND SWNTS

Adapted from "**Effect of Solvent Solubility Parameters on the Dispersion of Single-Walled Carbon Nanotubes**" ***J. Phys. Chem. C* 2008, *112*, 20154**.

Authors: Qiaohuan Cheng, Sourabhi Debnath, Elizabeth Gregan, Hugh J. Byrne

5.1 Introduction

In Chapter 4, the capability of a series of chlorinated aromatic solvents to disperse and solubilise HiPco SWNTs was evaluated. The significant difference in the efficacy of the different aromatic solvents in solubilizing as-produced SWNTs indicates that the similarity of the structure of SWNTs and the aromatic solvent molecules is not the dominant factor and no correlation with surface energies is observed. It is to be noticed that some of the physical parameters, such as dielectric constant, polarity etc. vary significantly between these solvents. In order to further investigate the correlation between SWNTs dispersibility and solvent characteristics, a further 4 solvents, toluene [1], chloroform [2], 1, 2-dichloroethane (DCE) [3] and dimethylformamide (DMF) [4, 5], previously reported as dispersion agents for SWNTs, are included. The molecular structures of the solvents are shown in Figure 5.1. A concentration dependence of absorbance in the normal chamber and the integrating sphere

enables the total extinction coefficient and absorbance coefficient of SWNTs in each solvent to be calculated. A correlation between the extinction / absorption coefficient and Hildebrand and Hansen solvent parameters is established, indicating that polar interactions and hydrogen bonding dominate.

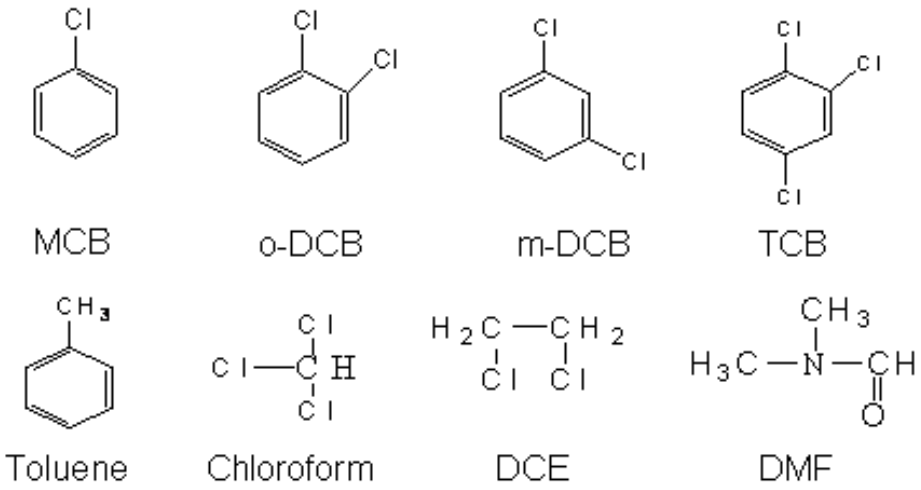

Figure 5.1 Molecular structures of the solvents.

The Hildebrand solubility parameter (δ) is a numerical estimate of the total intermolecular interactions within a solvent or solution. The value is defined as the square root of the cohesive energy density, as described in Equation 5.1 [6]:

$$\delta = \sqrt{c} = \sqrt{\frac{\Delta H - RT}{V_m}} \qquad \text{Equation 5.1}$$

where:

c is the cohesive energy density,

ΔH is the enthalpy of vaporization,

R is the gas constant,

T is the temperature,

V_m is molar volume.

As the cohesive energy density is a direct reflection of the degree of interaction holding the molecules of the liquid together, the value of the Hildebrand solubility parameter of a solvent is a measure of the intermolecular attractive forces which have to be overcome in dispersion processes [6]. When the intermolecular interactions of two different materials are close to each other, they are more likely to be miscible.

The total energy of vaporization of a solvent consists of several individual parts. These arise from (atomic) dispersion forces (δ_D), (molecular) permanent dipole-permanent dipole forces (δ_P), and (molecular) hydrogen bonding (δ_H) [6, 7]. It may happen that the solvent and solute have similar Hildebrand parameters, dominated by one of these components, but are not miscible at all [6]. Three dimensional Hansen solubility parameters give a numerical estimate of the different interactions and provide a clearer idea of the dominant component of the total cohesive energy of a solvent and therefore the physical origin of the interaction. Materials having similar Hansen solubility parameters have a high affinity for each other.

The relationship between the Hildebrand solubility parameters and three-dimensional Hansen solubility parameters is shown in equation 5.2 [6, 7]:

$$\delta^2 = \delta_D{}^2 + \delta_P{}^2 + \delta_H{}^2 \qquad \text{Equation 5.2}$$

where:

δ is the Hildebrand solubility parameter,

δ_D, δ_P, δ_H are the three dimensional Hansen solubility parameters.

In order to differentiate absorption from scattering, a concentration dependent study of the absorption in the normal chamber and the integrating sphere according to the Beer-Lambert law enables the calculation of the total extinction coefficient and absorption coefficient of SWNTs in each solvent.

The dispersibility of SWNTs in different solvents is quantitatively assessed in terms of the absorption and scattering parameters and their correlation with the Hildebrand solubility and three-dimensional Hansen solubility parameters is investigated with the aim of establishing structure property relationships governing the solubilising process.

5.2 Experimental section

Singe-walled carbon nanotubes (HiPco) were purchased from Carbon Nanotechnologies Inc., and used as supplied (batch no. PO341). MCB, o-DCB, *m*-DCB, TCB, Toluene and DMF were obtained from Sigma-Aldrich Ireland Ltd. DCE was purchased from ACROS ORGANICS and Chloroform was obtained from Fisher Scientific Ireland. All the solvents were used as received.

Dispersions of pristine HiPco nanotubes were prepared in all solvents at a maximum nanotube concentration of ~0.21 mg/ml. The initial dispersions were tip sonicated for 20 s using a high-power ultrasonic tip processor (Ultrasonic processor VCX 750 W) at 26% of the power output and then immediately serially diluted to produce a range of dispersions with concentrations from 0.21 ~ 0.001 mg/ml. All the samples were sonicated for another 100 s [8], so each

sample received the same sonication treatment. Immediately before measurement, all samples were vigorously shaken such that the effect of the sonication process on the dispersion of bundles and also the effectiveness of the integrating sphere in removing the contribution of scattering could be assessed.

UV-Vis-NIR absorption (Perkin Elmer Lambda 900, equipped with an integrating sphere, Spectralon as inner coating) measurements were performed in both the normal chamber and integrating sphere. 10 mm quartz cuvettes were used for all the measurements.

5.3 Results and Discussion

Immediately before measurement, all the samples were vigorously shaken and measured in the normal chamber and in the integrating sphere. The optical absorption spectrum of SWNT samples spans the UV-Vis-NIR and the absorbance at 660nm was chosen as a measure of SWNT content for comparison with other works [9, 10]. Peak intensities were read directly from the as measured absorption spectrum. The concentration dependences of the absorbance of all samples in the normal chamber (a) and the integrating sphere (b) are plotted in Figure 5.2. The pattern of linear dependence of the absorbance at low concentrations followed by deviation for higher concentrations has been demonstrated for NMP [9] and water based surfactant dispersions [11]. At the high concentrations, above the so-called dispersion limit,

the extinction is dominated by scattering and absorption from large bundles. Below the dispersion limit, the absorbance shows a linear dependence on concentration in accordance with the Beer-Lambert law, and the scattering is minimized. The SWNTs are dispersed into isolated tubes or small bundles and in the linear region, the absorption coefficient is a measure of the number of dispersed SWNTs and so the solubility or dispersibility. The concentration dependences of both the total extinction and the absorption coefficient were fitted with a Beer-Lambert linear dependence in the low concentration range and the calculated total extinction coefficient and absorption coefficient for all solvents are listed in Table 5.1. The values compare with the reported values of NMP of 3264 ml·mg^{-1}m^{-1} (at 660 nm) [9] and water of 215 ml·mg^{-1}m^{-1} (at 600 nm) [11].

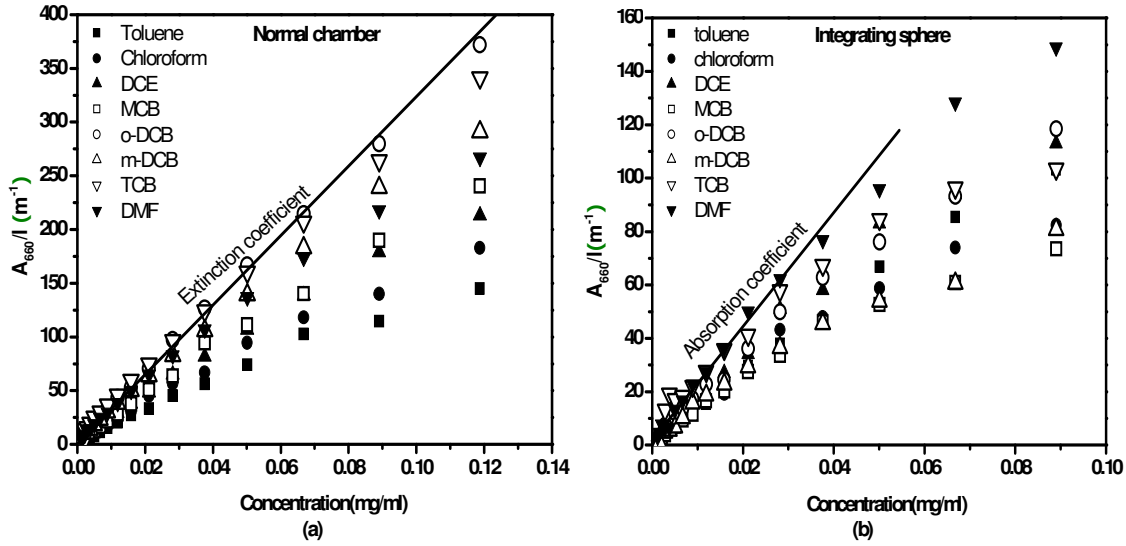

Figure 5.2 Concentration dependence of the absorbance of SWNT dispersions in various solvents, (a) in the normal chamber, (b) in the integrating sphere.

Table 5.1 The Hildebrand solubility parameter and Hansen solubility parameters of the solvents and the total Extinction coefficient and Absorption coefficient of SWNTs in different solvents.

Name	Molecular formula	δ_D[7] ($MPa^{1/2}$)	δ_P[7] ($MPa^{1/2}$)	δ_H[7] ($MPa^{1/2}$)	δ[12] ($MPa^{1/2}$)	Extinction coefficient ($ml \cdot mg^{-1}m^{-1}$)	Absorption coefficient ($ml \cdot mg^{-1}m^{-1}$)
Chloroform	$CHCl_3$	17.8	3.1	5.7	18.9	1572	1424
DCE	CH_2ClCH_2Cl	19.0	7.4	4.1	20.3	1884	1724
DMF	$HCON(CH_3)_2$	17.4	13.7	11.3	24.0	2312	2220
Toluene	C_7H_8	18.0	1.4	2.0	18.2	1271	1349
MCB	C_6H_5Cl	19.0	4.3	2.0	19.4	2058	1196
o-DCB	$C_6H_4Cl_2$	19.2	6.3	3.3	20.5	3132	1650
m-DCB	$C_6H_4Cl_2$	19.7	5.1	2.7	20.1	2525	1313
TCB	$C_6H_3Cl_3$	20.2	4.2	3.2	20.3	2835	1658

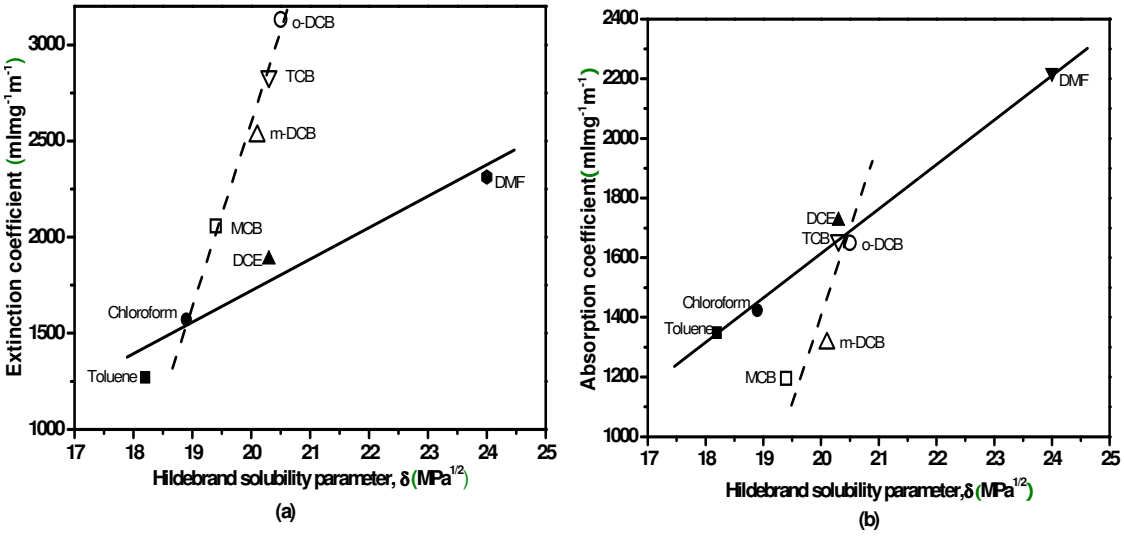

Figure 5.3 (a) Relationship between the total Extinction coefficient of SWNTs in each solvent with the Hildebrand solubility parameters; (b) Relationship between the Absorption coefficient of SWNTs in each solvent with the Hildebrand solubility parameters.

Figure 5.3 shows the relationship between the (a) extinction coefficient and (b) absorption coefficient and Hildebrand solubility parameter of the solvents. For the chlorinated aromatic solvents, the extinction coefficient appears to be

reasonably systematically correlated with the Hildebrand solubility parameter, and the outlying DMF and DCE along with toluene and chloroform may be similarly linearly correlated. The absorption coefficient appears less well correlated however, although the trend in the chlorinated aromatic solvents is similarly systematic and the other solvents can be seen to follow a separate linear trend.

It is worth noting, comparing the total extinction and absorption coefficient of SWNTs in different solvents, that in chlorinated aromatic solvents, the absorption coefficient is approximately 50% of the total extinction coefficient, indicating that half of the absorbance as measured in the normal chamber is due to the effect of scattering from the bundles even at low concentrations. However, in the other solvents no significant difference between the two is observed. At low concentrations, as shown in Figure 5.4 for the case of DCE, the scattering contribution goes to almost zero below the dispersion limit, as is the case for dispersions in water based surfactants [11] and NMP [9]. For *o*-DCB, however, there is still a significant amount of scatter present below the dispersion limit. This suggests that the bundles are only partially dispersed below the dispersion limit for the chlorinated aromatic solvents and that the ability to suspend bundles for short periods is not the same as that to debundle and suspend isolated tubes. In measurements which do not differentiate total extinction from absorption, o-DCB therefore registers as a relatively good solvent (large total extinction) for SWNTs (Figure 5.3 (a)), whereas Figure 5.3 (b) indicates that it is moderate.

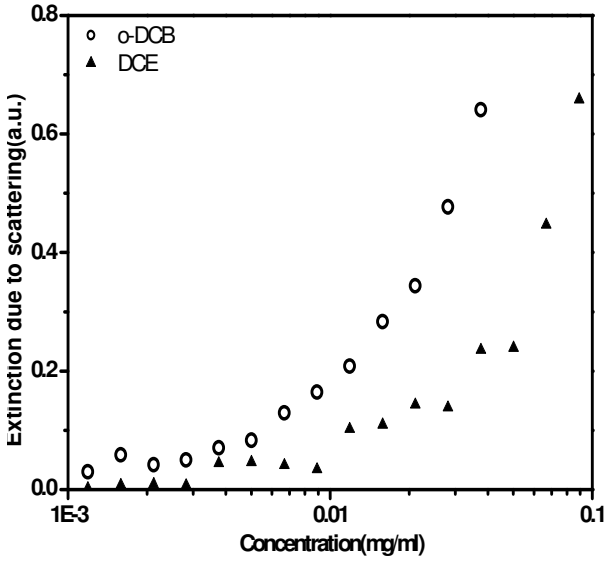

Figure 5.4 Extinction due to scattering in o-DCB and DCE dispersions

The relationship of the SWNTs extinction and absorption parameters with each of the three Hansen solubility parameters were plotted, and are shown in Figure 5.5 (a) - (f). The dispersion component seems not the dominant factor for dispersing SWNTs as no correlation is observed for either the total extinction or the absorption coefficient. The correlation between extinction / absorption coefficient with δ_P and δ_H is seen to be similar to that of the total Hildebrand parameter indicating that polarity and hydrogen bonding are important factors for obtaining SWNT dispersions. The best correlation between absorbance coefficient and solubility parameters is found for δ_P. The lack of correlation with δ_D is somewhat surprising as it may be expected that the phenyl ring would π stack well onto the graphitic sidewall of the nanotubes. δ_P and δ_H are however the dominant interactions in surfactant based dispersions. It should be noted, however, that δ_P is not a universal solubility parameter as the trend demonstrated for the non chlorinated aromatics is not followed by the reference solvents measured.

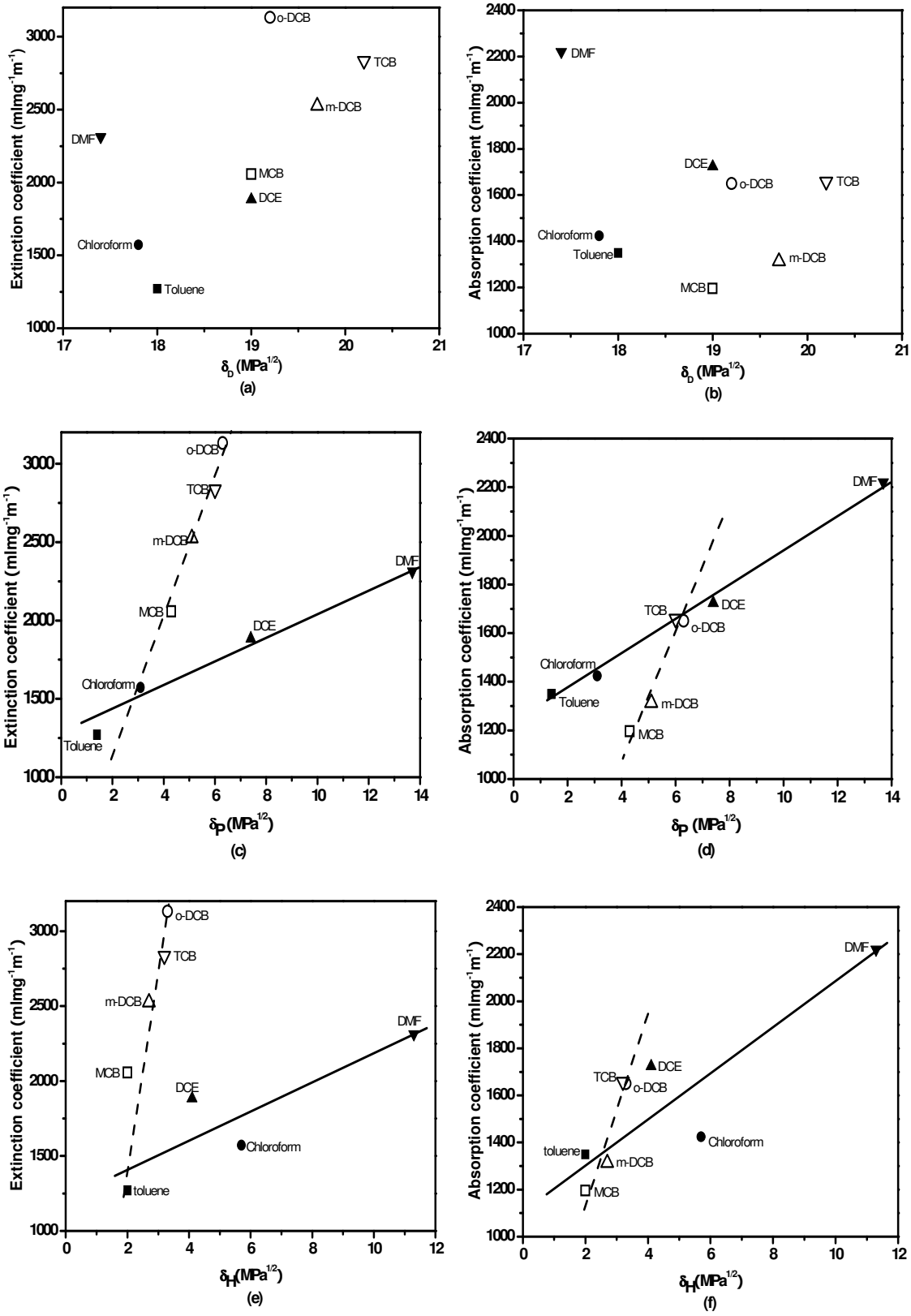

Figure 5. 5 (a) total Extinction coefficient *vs* dispersion component (δ_D) ; (b) Absorption coefficient *vs* dispersion component (δ_D) ; (c) total Extinction coefficient *vs* Polar component (δ_P) ; (d) Absorption coefficient *vs* Polar component (δ_P) ; (e) total Extinction coefficient *vs* Hydrogen bonding component (δ_H) ; (f) Absorption coefficient *vs* Hydrogen bonding component (δ_H).

5.4 Summary

The capability of a series of organic solvents to disperse and solubilise as-produced HiPco SWNTs has been evaluated in this chapter. Although the samples contain catalytic particles and other impurities, for many applications dispersion of as-produced samples is desirable. Stable dispersions of SWNTs have been demonstrated in some of these solvents. In assessing the characteristics of the suspension by absorption spectroscopy, it is of critical importance to differentiate between extinction due to scattering and due to true absorption as the ability to suspend bundles for a short time is not the same as the ability to debundle and suspend individual tubes. For chlorinated aromatic solvents, scattering from bundles is about 50% of the total extinction. For other solvents investigated, no significant difference between the two is observed, however, indicating efficient debundling below the dispersion limit.

In terms of the Hildebrand solubility parameter, the solubilisation in chlorinated aromatic solvents varies systematically but the trend is independent of that of the other reference solvents. Similar correlation with Hansen solubility parameter is observed for δ_{P} and δ_{H}. No correlation is observed for either total extinction coefficient or absorption coefficient with δ_{D} however.

The systematic study has therefore helped to elucidate some of the structure property relationships governing dispersion of SWNTs and further studies should seek to extend the basis set. However, although the other reference solvents show a similar correlation with δ_{P}, the trendline is different and so it is

not a universal solubility parameter. An understanding of the underlying physical origin of the different trends may however lead to the determination of such a universal parameter.

5.5 References

1. Hedderman, T.G.; Keogh, S.M.; Chambers, G.; Byrne, H.J., Solubilization of SWNTs with organic dye molecules. Journal of Physical Chemistry B, 2004, **108**, 18860-18865.
2. Bahr, J.L.; Mickelson, E.T.; Bronikowski, M.J.; Smalley, R.E.; Tour, J.M., Dissolution of small diameter single-wall carbon nanotubes in organic solvents? Chemical Communications, 2001,193-194.
3. Kim, K.K.; Bae, D.J.; Yang, C.M.; An, K.H.; Lee, J.Y.; Lee, Y.H., Nanodispersion of single-walled carbon nanotubes using dichloroethane. Journal of Nanoscience and Nanotechnology, 2005, **5**,1055-1059.
4. Furtado, C.A.; Kim, U.J.; Gutierrez, H.R.; Pan, L.; Dickey, E.C.; Eklund, P.C., Debundling and dissolution of single-walled carbon nanotubes in amide solvents. Journal of the American Chemical Society, 2004, **126**, 6095-6105.
5. Landi, B.J.; Ruf, H.J.; Worman, J.J.; Raffaelle, R.P., Effects of alkyl amide solvents on the dispersion of single-wall carbon nanotubes. Journal of Physical Chemistry B, 2004, **108**, 17089-17095.
6. Burke, J., Solubility parameters: theory and application. The Book and paper group annual 1984, **3**: 13-58.

7. Hansen, C.M., Hansen Solubility Parameters: A User's Handbook. 1999, CRC Press.

8. Cheng, Q.H.; Debnath, S.; Gregan, E.; Byrne, H.J., Effects of chlorinated aromatic solvents on the dispersion of HiPco SWNTs. Physica Status Solidi B-Basic Solid State Physics, 2008, **245**, 1947-1950.

9. Giordani, S.; Bergin, S.D.; Nicolosi, V.; Lebedkin, S.; Kappes, M.M.; Blau, W.J.; Coleman, J.N., Debundling of single-walled nanotubes by dilution: Observation of large populations of individual nanotubes in amide solvent dispersions. Journal of Physical Chemistry B, 2006, **110**, 15708-15718.

10. Hasan, T.; Scardaci, V.; Tan, P.H.; Rozhin, A.G.; Milne, W.I.; Ferrari, A.C., Stabilization and "Debundling" of single-wall carbon nanotube dispersions in N-Methyl-2-pyrrolidone (NMP) by polyvinylpyrrolidone (PVP). Journal of Physical Chemistry C, 2007, **111**, 12594-12602.

11. Priya, B.R.; Byrne, H.J., Investigation of Sodium Dodecyl Benzene Sulphonate Assisted Dispersion and Debundling of Single Wall Carbon Nanotubes. Journal of Physcial Chemistry C, 2008, **112**, 332-337.

12. Abboud, J.L.M.; Notario, R., Critical compilation of scales of solvent parameters. Part I. Pure, non-hydrogen bond donor solvents - Technical report. Pure and Applied Chemistry, 1999. **71**,4, 645-718.

CHAPTER 6
STRUCTURAL ASSIGNMENT OF SWNTS

*Adapted from "***Vibrational mode assignments for bundled single-wall carbon nanotubes using Raman spectroscopy at different excitation energies***" **Applied Physics A,* submitted (January 2010).**

Authors: Qiaohuan Cheng, Sourabhi Debnath, Elizabeth Gregan, Hugh J. Byrne

6.1 Introduction

The two different apparent linear correlations of extinction/absorption coefficient and solvent solubility parameters indicated for the set of chlorinated aromatic solvents and the "other" solvents in Chapter 5 suggests that there may be a selective interaction of the different classes of solvents with different types of nanotubes. Differentiation of solutions of metallic and semiconducting tubes should be observable via utilization of UV-Vis-NIR absorption spectroscopy. However, as the solubilities of SWNTs in the solvents were rather low, this was not possible and Raman spectroscopy was employed as an alternative.

As described in Chapter 3, resonance Raman spectroscopy is one of the most important techniques in the characterization of SWNTs and their composites [1-5]. Compared to other techniques of SWNT structural assignments [1, 6-9], Raman spectroscopy is the most convenient and rapid technique to determine the structural indices (n, m) of both semiconducting and metallic nanotubes [5,

10-12]. Based on the relationship between ω_{RBM}, d and (n, m) described in Chapter 2 and Chapter 3 (Equation 2.2 ($d = \sqrt{3(n^2 + m^2 + mn)}b/\pi$) and Equation 3.8 ($\omega_{RBM} = A/d + B$)), the task of determining nanotube diameters and thus assigning structural indices and deducing the electrical properties of the examined tubes appears simple. However, in practice this is not so easy, as many different combinations of A and B in Equation 3.8 can be found in literature. Due to the differences in the tube growth methods, diameter distribution, dispersion conditions or even the substrates and surfactants, the reported values have been found to vary over a significant range [1, 10-12, 17-24]. For example, Thomsen *et al.* and Telg *et al.* reported A = 214 ± 2 cm^{-1}·nm and B = 19 ± 2 cm^{-1} [12, 13] for surfactant stabilised HiPco SWNTs (d ≈ 0.7-1.2nm) in D_2O solution. The values of A and B were fitted to be 217.8 ± 0.3 cm^{-1} nm and 15.7 ± 0.3 cm^{-1} for as-grown vertically aligned CVD SWNTs with a diameter range of 0.7- 2.3 nm. The sample consisted of isolated nanotubes and very small bundles on quartz substrates [14]. A Raman study of HiPco SWNTs with a small diameter range (d ≈ 0.6-1.2 nm) was carried out by Bachilo and Strano et al. By the combination of fluorimetric and Raman results, the values for *A* and *B* were fitted to be A = 223.5 cm^{-1}·nm, B = 12.5 cm^{-1} [1, 15] for tubes dispersed in aqueous medium by SDS. In Yu's study of shortened laser vaporization SWNTs (d ≈ 1.05 - 1.6 nm), values of A = 223.75 cm^{-1} ·nm, B = 15 cm^{-1} were employed for calculating the diameter from the RBM frequencies of DMF dispersed SWNT bundles on a -NH_2 functionalized glass coverslip [16]. The values of A and B were also reported to be different for metallic and semiconducting tubes. Fantini *et al* reported two pairs of values, A = 223 cm^{-1} ·nm, B = 10 cm^{-1} for semiconducting tubes and A = 218 cm^{-1} ·nm, B = 17 cm^{-1}

for metallic tubes respectively [10] in the case of HiPco SWNTs wrapped by SDS in aqueous solution. Furthermore, A = 234 cm^{-1}·nm and B = 10 cm^{-1} are well accepted for SWNT bundles with a diameter range 1.5 ± 0.2 nm [17]. This variation makes the structural assignments of SWNTs complex and confusing.

In order to investigate any potential selectivity of nanotube type by the examined solvents, an entire Raman investigation of the SWNT sample used in this study is required. In this chapter, an investigation of the pristine SWNT sample with 4 different laser energies (2.62 eV, 2.33 eV, 1.88 eV and 1.58 eV) is described. Structural assignments are made according to a more generic fitting approach to assignment of nanotube chiralities based on RBMs frequencies, developed during this project. The values of A and B, obtained by the best fit of a linear regression between ω_{RBM} and $1/d$, were found to vary significantly for different laser frequencies. The RBMs obtained from SWNTs dispersed from different solvents at 660nm were then compared with that of the original sample in order to examine any chirality or electrical property selectivity.

6.2 Experimental

HiPco Single-walled carbon nanotubes were purchased from Carbon Nanotechnologies Inc., and used as supplied (batch no. PO341).

The Raman sample of the prinstine SWNTs was prepared as follow: the SWNT powder was first dispersed in chloroform (0.2 mg/ml), and the dispersion was sonicated for 20 s using a high-power ultrasonic tip processor (VCX 750 W).

The suspension obtained has previously been demonstrated to be temporarily dispersed and the nanotubes exist as large bundles (Chapter 4) [18]. Immediately after sonication, a few drops of SWNT-chloroform dispersion were drop-cast onto a quartz substrate. The sample was allowed to dry at room temperature.

Raman samples for SWNT/solvent were prepared by dropcasting a few drops of supernatant after centrifugation onto cleaned quartz substrate. Raman measurements were performed with a LabRAM HR800 Raman Microscope (Horiba Jobin Yvon) at laser energies 1.58 eV (785 nm, 12.2 mW), 1.88 eV (660 nm, 8.4 mW), 2.33 eV (532 nm, 30.6 mW) and 2.62 eV (473 nm, 0.3 mW). The laser powers were measured by a power meter at the sample stage. A 50× objective lens was used for all the measurements. Using the mapping option of the instrument, 50 spectra of SWNT bundles were obtained and analysed for each laser line.

6.3 Results and discussions

As described in Chapter 3, according to the resonance theory, only when the excitation energy, *i.e.* the laser energy, is close enough to E_{ii}, will the tube be resonant and give a strong Raman signal [11, 19].

Figure 6.1 presents the typical RBM spectra of the HiPco SWNT bundles at the 4 different excitation energies and the corresponding G-band regions. As

expected, it was observed that at different laser energies, different RBM peaks dominate. Each peak corresponds to a carbon nanotube in resonance with the excitation energy thereby indicating that different tubes are resonant at different laser energies. The spectrum taken using the 1.58 eV laser as source shows a broad intense RBM band at 260 - 270 cm^{-1} and this feature is expected to arise from the medium diameter tubes. It is predicted that only semiconducting tubes are resonant at 1.58 eV and this can be confirmed by the observation of a typical semiconducting lineshape of the G-band. Comparing to other laser energies, the spectrum taken at 1.88 eV shows a strong Raman signal below 200 cm^{-1} which corresponds to the larger diameter tubes in the sample. A G-band of semiconducting character was also observed at this laser line. The spectrum taken at 2.33 eV shows a few very close but intense RBM signals between 250 – 280 cm^{-1} and they are predicted to arise from the E_{11}^{M} (Equation 3.8) transitions. A very broad and downshifted G^{-} feature is seen, with a characteristic metallic BWF lineshape. The spectrum taken at 2.62 eV shows a strong RBM feature at ~ 230 cm^{-1} followed by a few medium strength bands at both lower and higher frequency. As the 2.62 eV laser intersects both E_{11}^{M} and E_{33}^{S} bands in the Kataura plot (Figure 3.13), the corresponding G-band contains both semiconducting and metallic features.

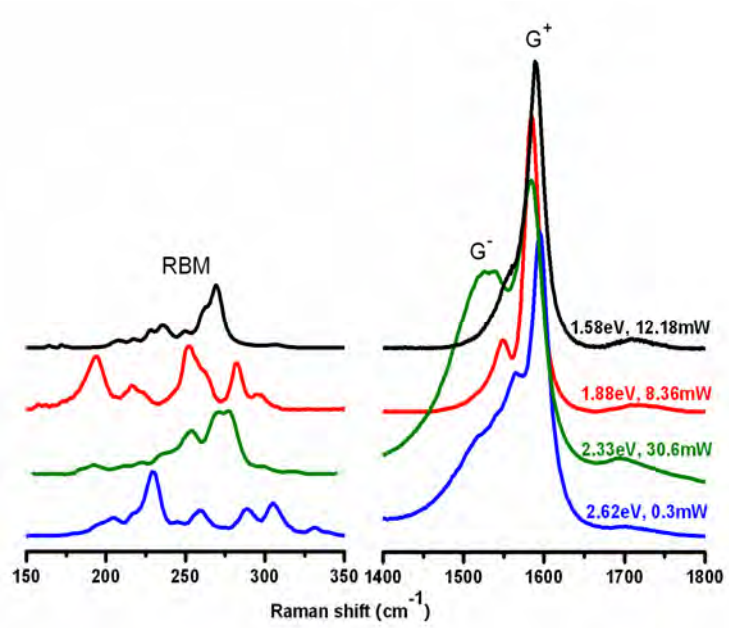

Figure 6.1 RBM frequencies (normalised to the most intense peak) of bundled HiPco SWNTs dispersed on quartz substrate at different excitation energies and the corresponding G-band (normalized to the G^+ peak).

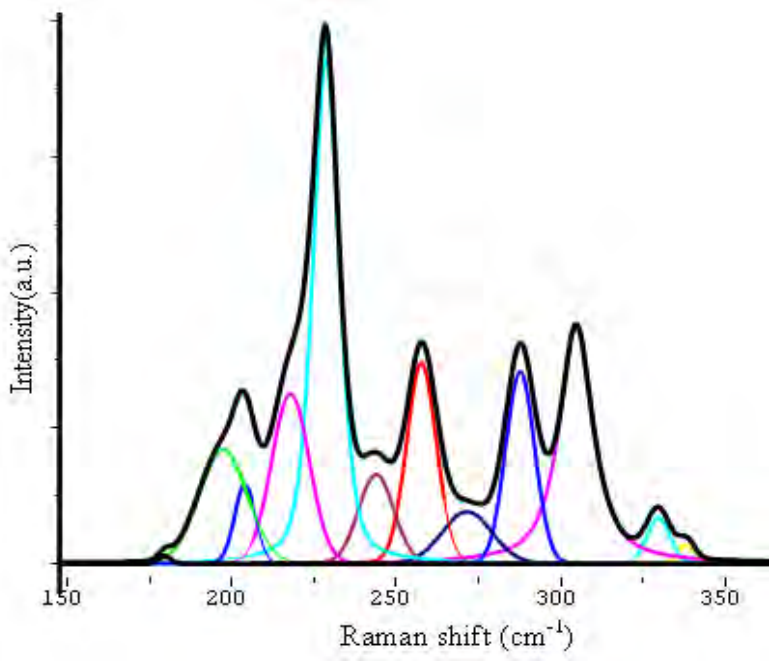

Figure 6.2 Radial breathing modes obtained from the HiPco SWNT bundles with 2.62 eV excitation energy. The peaks are fitted by 12 Gauss/Lorentz curves.

Figure 6.2 presents the RBM region of the spectrum taken at 2.62 eV. It can be fitted by 12 Gauss/Lorentz curves. The most intense peak appears at 229 cm^{-1}, followed by 5 medium intensity peaks at 196 cm^{-1}, 218 cm^{-1}, 258 cm^{-1}, 288 cm^{-1} and 305 cm^{-1}. In order to calculate the corresponding diameter and establish the possible (n, m) assignments, a linear regression of the plot of ω_{RBM} versus $1/d$ was performed. The fitting method is described below:

(1) The possible diameter range was calculated with the equation $\omega_{RBM} = A/d + B$, where values of A = (214 + 2) = 216 cm^{-1}·nm, B = (19 – 2) = 17 cm^{-1} [13, 22] and A = 234 cm^{-1}·nm, B = 10 cm^{-1} are chosen from the literature [25], such that the widest variation in diameter range can be calculated.

(2) The Kataura plot was then employed to identify which nanotubes within the diameter range are close to resonance at the laser frequency and to establish whether they are metallic or semiconducting.

(3) The possible diameters from the Kataura plot were chosen and the inverse of these diameters were plotted against the experimentally determined ω_{RBM}. The best fit is constrained by the features which are uniquely assigned and the points which are closest to this linear regression for other RBM frequencies were chosen to refine the values of A and B.

Table 6.1 lists the frequencies of the RBMs at 2.62 eV, the diameters calculated according to the literature values of the parameters A and B, their electronic character and refined diameters as determined from the Kataura plot. For this case, a best fit yields values of A = 213.7 ± 0.6 cm^{-1} nm and B = 22.7 ± 0.7 cm^{-1} (Figure 6.3). It should be noted that the diameter of the tubes is calculated using Equation 3.8, so the value of the *C-C* bond length (0.142 nm or 0.144 nm)

also affects the results. In this study, a value of $a_{C\text{-}C}$ = 0.144nm is used for all the calculations.

Table 6.1 Experimental ω_{RBM} at 2.62 eV and calculated diameter range d_1 (A = 216, B = 17) and d_2 (A = 234, B = 10), electronic property (M: metallic; S: semiconducting) together with the possible diameters (ω_{RBM}: mean value from 50 spectra)

ω_{RBM} (cm^{-1})	d_1(nm)	d_2(nm)	M or S	Possible diameters (nm)			
180.9	1.317	1.369	S	1.321336	1.335578	1.349653	1.355664
196.0	1.207	1.258	S	1.201409	1.232483	1.240133	1.247733
204.8	1.149	1.201	S	1.144998	1.153226	1.169508	1.185566
218.5	1.072	1.122	M	1.073986	1.091451	1.100079	1.125567
229.3	1.018	1.067	M	1.038174			
244.5	0.949	0.998	M	0.952696	0.962569	0.991598	
258.4	0.895	0.942	M	0.901712			
271.1	0.850	0.896	M	0.858749			
288.2	0.796	0.841	S	0.825059	0.836440	0.805734	
305.5	0.749	0.792	S	0.757345	0.781914	0.793914	
330.5	0.689	0.730	S	0.692118	0.705646		
338.7	0.671	0.712	S	0.678320	0.692118	0.705646	

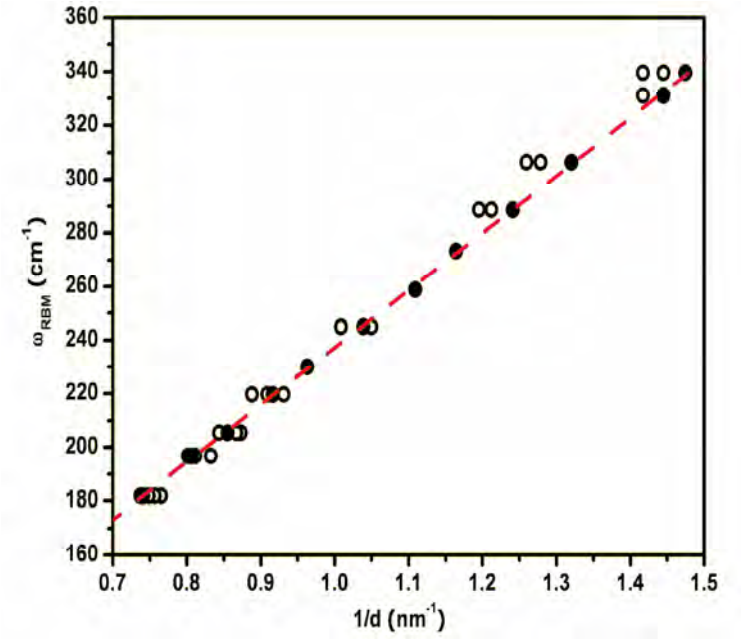

Figure 6.3 Observed RBM frequencies at 2.62 eV as a function of inverse diameter. The filled circles fall into the best linear fitting line (the dashed line) with smallest error. A = 213.7 ± 0.6 cm^{-1} ·nm and B = 22.7 ± 0.7cm^{-1}.

Similarly the linear regression between the RBM frequencies and inverse nanotube diameters measured at the other laser frequencies were carried out and the values of A and B obtained from the linear regression, together with the deduced assignments are listed in Table 6.2. The identities of the assigned tubes observed in this study at different laser energies are indicated in the Kataura plot, shown in Figure 6.4. It was seen that most of the tubes sit in the E_{22}^{S} and E_{11}^{M} branches and only 5 tubes from E_{33}^{S} are observed here, 3 tubes resonant at 2.62 eV and 2 at 2.33 eV.

Table 6.2 RBM shifts and the corresponding structure assignments ($\omega_{RBM:}$ Mean value from 50 spectra)

Laser energy	ω_{RBM} (cm^{-1})	Diameter (nm)	Assignment	S or M	A/cm^{-1}·nm & B/ cm^{-1}
1.58 eV 785 nm	207.6	1.14500321	(12,4)	S	A= 221.5± 1.6 B= 14.4 ± 1.7
	217.7	1.10293712	(9,7)	S	
	227.7	1.0320876	(8,7)	S	
	236.5	0.99476752	(12,1)	S	
	249.6	0.93601408	(10,3)	S	
	261.4	0.89469446	(7,6)	S	
	269.9	0.87330143	(11,0)	S	
	307.1	0.75734626	(6,5)	S	
1.88 eV 660 nm	180.2	1.37509969	(10,10)	M	A = 207.5± 0.8 B = 29.1 ± 0.8
	186.2	1.32610166	(15,3)	M	
	193.6	1.26030298	(12,6)	M	
	216.1	1.1114816	(10,6)	S	
	224.0	1.0681022	(11,4)	S	
	243.0	0.9658383	(8,6)	S	
	250.0	0.93601408	(10,3)	S	
	254.7	0.91558323	(11,1)	S	
	262.4	0.88406386	(10,2)	S	
	281.8	0.82887124	(7,5)	S	
	294.93	0.78191585	(8,3)	S	
2.33 eV 532 nm	182.4	1.3355771	(13,6)	S	A = 233.0± 1.1 B = 8.5 ± 1.1
	192.5	1.27026066	(16,0)	S	
	213.7	1.12556841	(11,5)	M	
	222.5	1.09145283	(12,3)	M	
	233.2	1.03817364	(9,6)	M	
	244.8	0.99160114	(10,4)	M	
	254.0	0.95269852	(12,0)	M	
	268.3	0.90171326	(8,5)	M	
	278.0	0.8587524	(9,3)	M	
	295.9	0.80573685	(9,2)	S	
	317.2	0.75734626	(6,5)	S	
2.62 eV 473 nm	180.9	1.34965516	(17,0)	S	A= 213.7 ± 0.6 B= 22.7 ± 0.7
	196.0	1.240133	(10,8)	S	
	204.8	1.16950857	(13,3)	S	
	218.5	1.09145283	(12,3)	M	
	229.3	1.03817364	(9,6)	M	
	244.5	0.96256582	(7,7)	M	
	258.4	0.90171326	(8,5)	M	
	271.1	0.8587524	(9,3)	M	
	288.2	0.80573685	(9,2)	S	
	305.5	0.75734626	(6,5)	S	
	330.5	0.69211816	(6,4)	S	
	338.7	0.67832021	(8,1)	S	

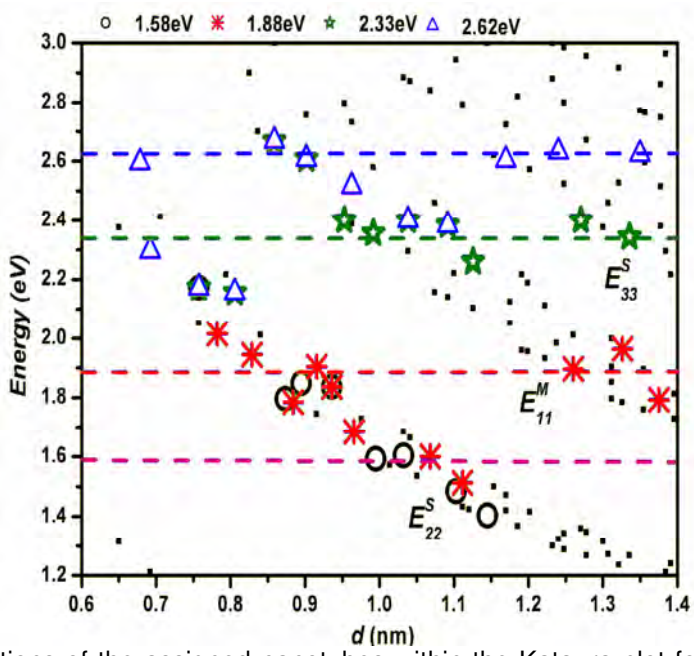

Figure 6.4 Locations of the assigned nanotubes within the Kataura plot for the different laser energies.

The energy difference between E_{ii} and E_{laser} (ΔE) as a function of the nanotube diameter is plotted in Figure 6.5. 76% of the assigned nanotubes are within ± 0.2 eV of the source laser energy, indicating the spectral width of the resonance enhancement. This is consistent with the reported resonance window of bundled HiPco SWNTs [10]. It is also evident that ΔE is larger for smaller diameter tubes, which have been found to have broadened absorption bands compared to those of larger tubes [19] and that for the larger diameter tubes (1.15-1.40 nm), it was found that $|\Delta E| < 0.1$ eV, which is in good agreement with the reported resonance window [11, 20]. This trend does not however differentiate between metallic and semiconducting resonances as has been previously reported [21].

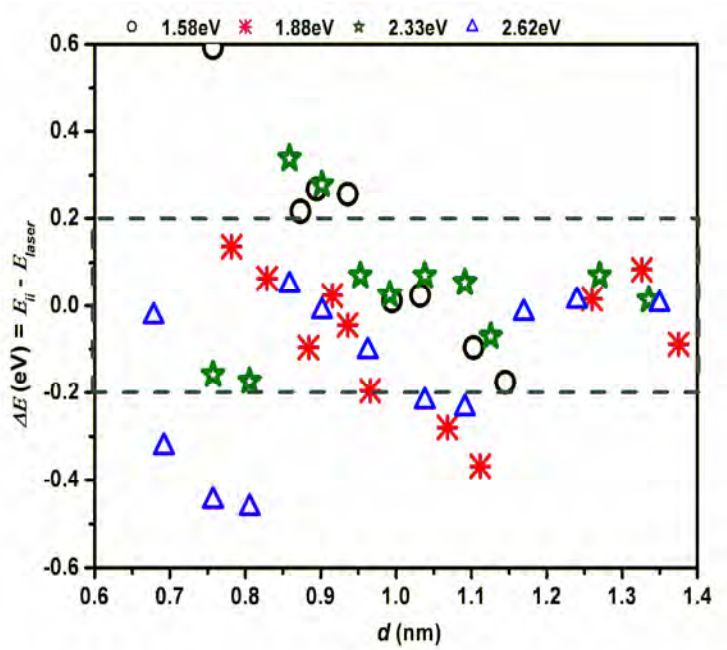

Figure 6.5 Energy differences between E_{ii} and E_{laser} (ΔE) as a function of nanotube diameter.

A histogram of the diameter distributions from the four laser energies is plotted in Figure 6.6, which shows a good agreement with the reported HiPco SWNTs diameter distribution [22].

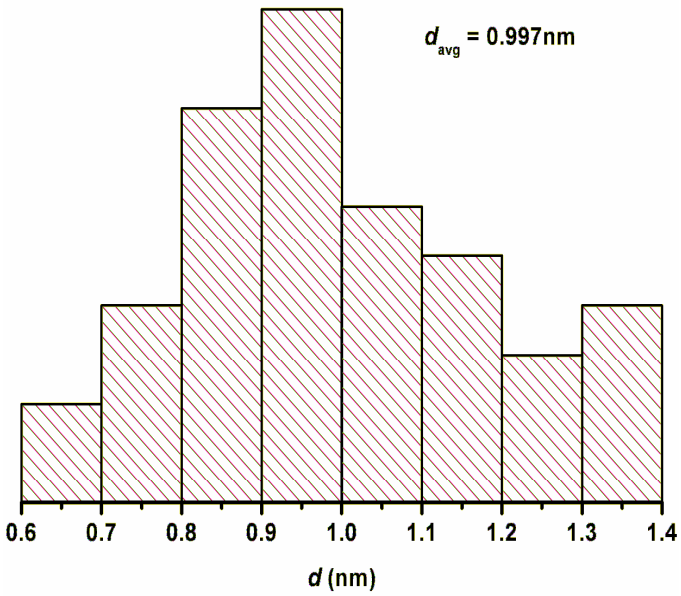

Figure 6.6 Histogram of the diameter distribution from the assignment results for four laser energies

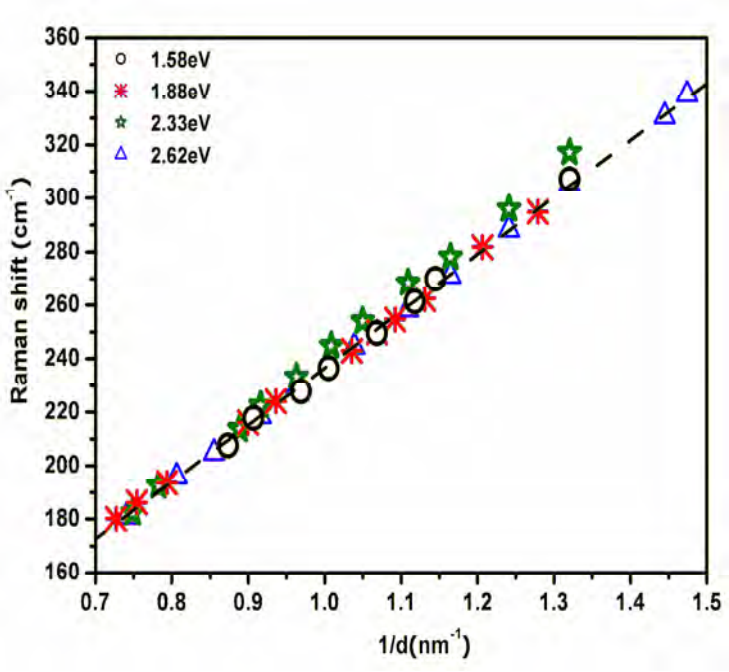

Figure 6.7 Observed RBM frequencies as a function of inverse possible diameters at all laser lines. The dashed line is a linear fitting of the points from 2.62 eV, 1.88 eV and 1.58 eV, A= 213.1 ± 1.3 cm^{-1} · nm and B = 23.7 ± 1.4 cm^{-1}.

The fitting parameters A and B for different laser energies were found to vary significantly with excitation energy. However, as shown in Figure 6.7, the points from the three laser lines at 2.62 eV, 1.88 eV and 1.58 eV can be well fitted with one linear correlation, with A = 213.1 cm^{-1} ·nm and B = 23.7 cm^{-1}. However the points from 2.33 eV deviate significantly from this fit.

The laser power at 2.33 eV is notably higher than that for the other laser lines. Although a local heating effect for individual suspended SWNTs, causing a down shift of the RBM frequencies with increasing laser power, has been reported [23], no observable shift of RBM frequencies was observed for the laser powers utilized here. Furthermore, compared to the spectra for other laser energies, the RBM frequencies at 2.33 eV are upshifted in Figure 6.7 rather

than downshifted. Therefore, frequency shifting as a result of laser heating cannot account for the deviation observed for 2.33 eV.

It should be noted that the nanotubes resonant at this laser energy are predominantly metallic, whereas semiconducting nanotubes dominate the Raman spectra at the other laser lines. It can thus be concluded that the difference in the fit parameters is attributed to the different electronic character of the dominant resonant nanotubes. A similar difference has been reported by Fantini *et al* [10]. However within the nanotubes identified for a given laser line, no differentiation is discernible between the best fits for semiconducting and metallic.

Having characterized the pristine SWNT sample used in this work, a comparative study of the SWNTs dispersed in DMF and o-DCB was conducted. The solvents were chosen as they are on the extremes of the apparently different linear trends of Figure 5.3 and Figure 5.5.

Figure 6.8 (a) and (b) show the single-point Raman spectra of pristine SWNTs and the tubes dispersed in DMF at a concentration of 0.001 mg/ml (which will be confirmed to be well debundled by the AFM study in Chapter 7), obtained with excitation energies at 2.33 eV and 1.88 eV respectively. These two laser energies were chosen because the spectra are dominated by metallic and semiconducting nanotubes respectively, as indicated in Table 6.2. Compared to the RBM profile of pristine SWNTs, the number of RBMs in the DMF solution at 0.001 mg/ml was decreased significantly, particularly in the low frequency region. This indicates that most of the larger diameters tubes precipitate from

the solution, only the smaller diameter tubes being suspended. In the case of o-DCB solution at 0.001 mg/ml, a similar behaviour is observed.

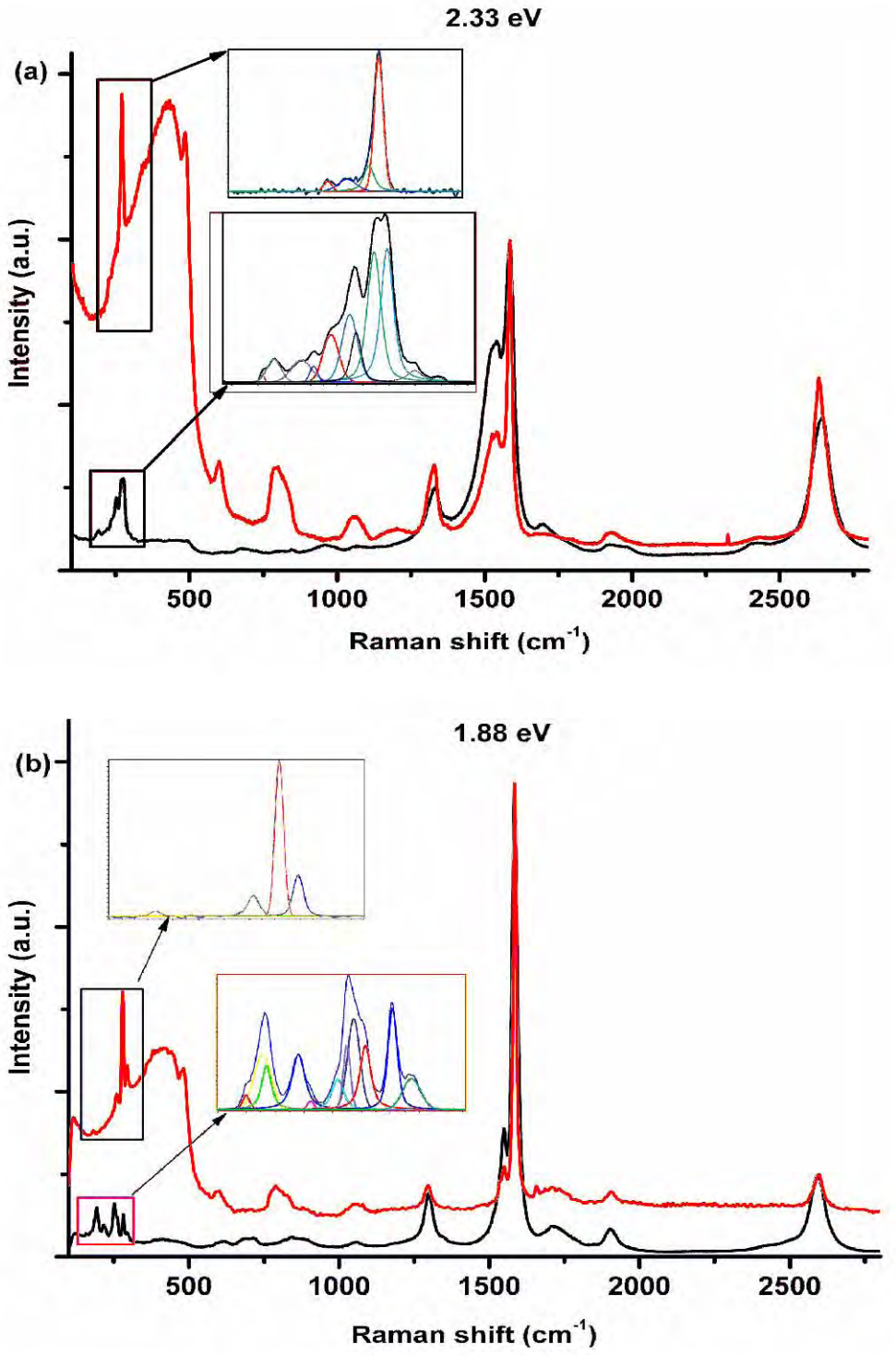

Figure 6.8 Raman spectra of Pristine SWNTs and SWNTs dispersed in DMF at 0.001 mg/ml. The insets are the corresponding RBMs with curve fitting. (a) 2.33 eV, (b) 1.88 eV.

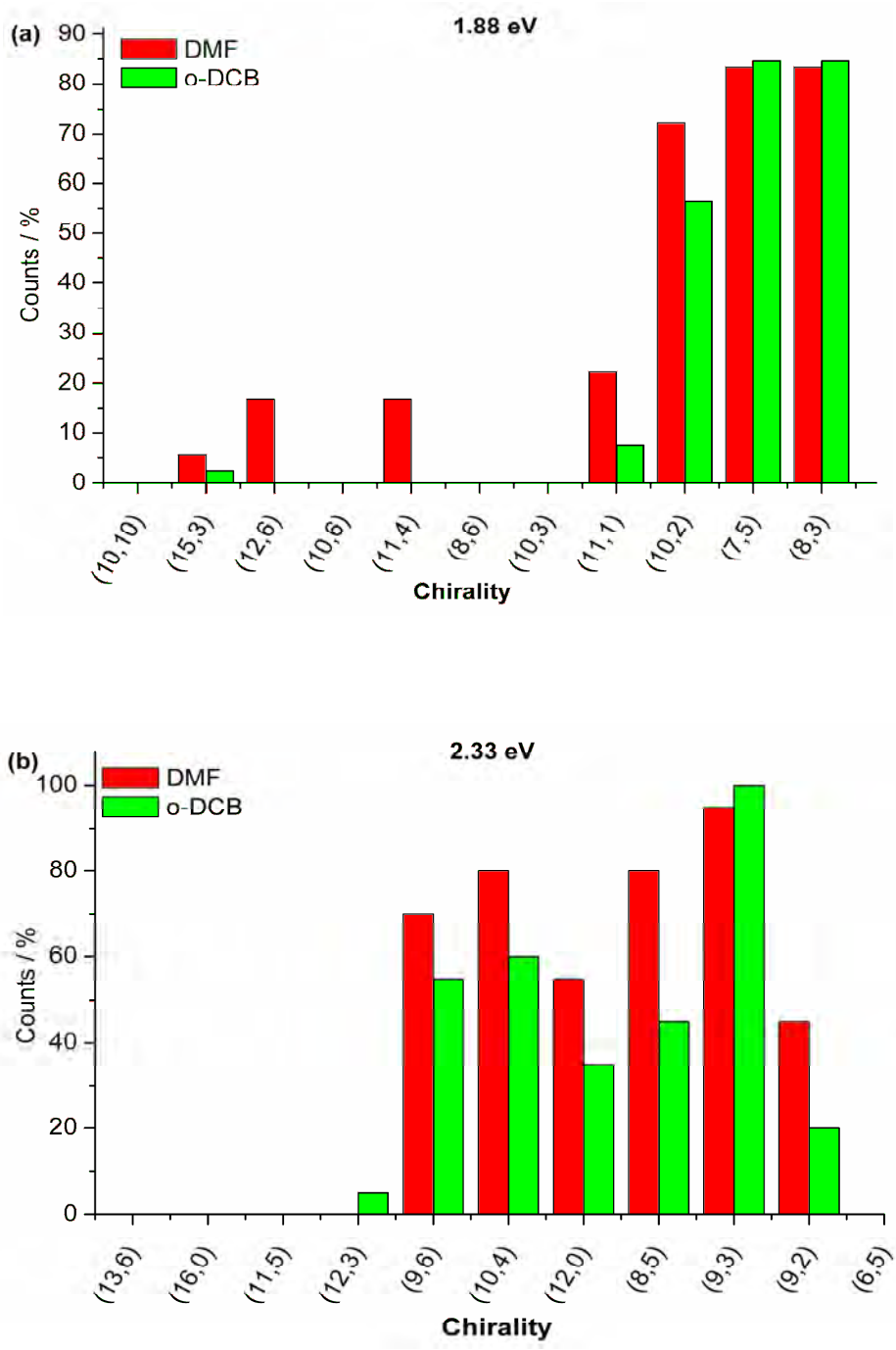

Figure 6.9 Histogram of occurrence of identified SWNTs in DMF and *o*-DCB solutions, (a) 1.88 eV, (b) 2.33 eV.

Assuming that the SWNTs identified in the solutions are present in the pristine sample, histograms of occurrence of identified SWNTs in DMF and *o*-DCB were constructed, as shown in Figure 6.9. Up to 20 different spots were examined

with 2.33 eV and 1.88 eV for each sample. The x-axis indicates the chirality of the nanotubes identified in the pristine SWNT sample. The tubes are located from left to right according to their diameters, larger to smaller. Comparing the SWNTs identified at 1.88 eV, in both of the solvents, smaller diameter tubes dominate the solutions. A similar behaviour is observed at 2.33 eV for both solvents.

Most notably, no obvious selectivity can be identified for the two solvents, as they both show similar trends compared to the pristine sample. Thus, although amongst the solvents selected for examination in Chapter 5, there appeared to be two distinct classes, there is no obvious differentiation between the solvents classes in terms of selective solubilisation of the SWNTs.

6.4 Summary

Structural assignments of bundled SWNTs were carried out based on the linear correlation between ω_{RBM} and $1/d$. The linear correlation parameters between ω_{RBM} *vs* $1/d$ were found to vary significantly with the laser energy. Although the points from the semiconducting tubes-dominated spectra can be fitted by a single straight line, the points from metallic-dominated spectra deviate from the fitting. This deviation is attributed to the difference between semiconducting and metallic tubes. The resonance bandwidths were plotted against nanotube diameter and a difference was observed between large and small diameter tubes. It is apparent that, rather than being well defined parameters, A and B

are strongly dependent on the character of the nanotubes, and by extrapolation any perturbation of that character due to the local environment.

The comparison Raman study of the tubes dispersed in DMF and *o*-DCB, which appeared to be located on different trend lines of the extinction/absorption coefficient *vs* solvent parameters plot in Chapter 5, indicates there is no specific selectivity, which may indicate different mechanisms of interaction, of the examined solvents. In order to further investigate the correlation between solvent parameters and solubility, more solvents, according to their solubility parameters, are required.

6.5 References

1. Bachilo, S.M.; Strano, M.S.; Kittrell, C.; Hauge, R.H.; Smalley, R.E.; Weisman, R.B. Structure-assigned optical spectra of single-walled carbon nanotubes. Science, 2002, **298**, 2361-2366.
2. Dresselhaus, M.S.; Dresselhaus, G.; Jorio, A. Raman spectroscopy of carbon nanotubes in 1997 and 2007. Journal of Physical Chemistry C, 2007, **111**, 17887-17893.
3. Dresselhaus, M.S.; Dresselhaus, G.; Saito, R.; Jorio, A. Raman spectroscopy of carbon nanotubes. Physics Reports-Review Section of Physics Letters, 2005, **409**, 47-99.
4. Thomsen, C.; Reich, S. Raman scattering in carbon nanotubes. Light Scattering in Solids Ix, 2007, **108**, 115-235.

5. Yu, Z.H.; Brus, L.E. (n, m) structural assignments and chirality dependence in single-wall carbon nanotube Raman scattering. Journal of Physical Chemistry B, 2001, **105**, 6831-6837.

6. Meyer, J.C.; Paillet, M.; Michel, T.; Moreac, A.; Neumann, A.; Duesberg, G.S.; Roth, S.; Sauvajol, J.L. Raman modes of index-identified freestanding single-walled carbon nanotubes. Physical Review Letters, 2005, **95**, 217401.

7. Odom, T.W.; Huang, J.L.; Kim, P.; Lieber, C.M. Atomic structure and electronic properties of single-walled carbon nanotubes. Nature, 1998, **391**, 62-64.

8. Wildoer, J.W.G.; Venema, L.C.; Rinzler, A.G.; Smalley, R.E.; Dekker, C. Electronic structure of atomically resolved carbon nanotubes. Nature, 1998, **391**, 59-62.

9. Zhu, H.W.; Suenaga, K.; Hashimoto, A.; Urita, K.; Iijima, S. Structural identification of single and double-walled carbon nanotubes by high-resolution transmission electron microscopy. Chemical Physics Letters, 2005, **412**, 116-120.

10. Fantini, C.; Jorio, A.; Souza, M.; Strano, M.S.; Dresselhaus, M.S.; Pimenta, M.A. Optical transition energies for carbon nanotubes from resonant Raman spectroscopy: Environment and temperature effects. Physical Review Letters, 2004, **93**.

11. Jorio, A.; Saito, R.; Hafner, J.H.; Lieber, C.M.; Hunter, M.; McClure, T.; Dresselhaus, G.; Dresselhaus, M.S. Structural (n, m) determination of isolated single-wall carbon nanotubes by resonant Raman scattering. Physical Review Letters, 2001, **86**, 1118-1121.

12. Thomsen, C.; Telg, H.; Maultzsch, J.; Reich, S. Chirality assignments in carbon nanotubes based on resonant Raman scattering. Physica Status Solidi B-Basic Solid State Physics, 2005, **242**, 1802-1806.

13. Telg, H.; Maultzsch, J.; Reich, S.; Hennrich, F.; Thomsen, C. Chirality distribution and transition energies of carbon nanotubes. Physical Review Letters, 2004, **93**, 177401.

14. Araujo, P.T.; Doorn, S.K.; Kilina, S.; Tretiak, S.; Einarsson, E.; Maruyama, S.; Chacham, H.; Pimenta, M.A.; Jorio, A. Third and fourth optical transitions in semiconducting carbon nanotubes. Physical Review Letters, 2007, **98**, 067401.

15. Strano, M.S.; Doorn, S.K.; Haroz, E.H.; Kittrell, C.; Hauge, R.H.; Smalley, R.E. Assignment of (n, m) Raman and optical features of metallic single-walled carbon nanotubes. Nano Letters, 2003, **3**, 1091-1096.

16. Yu, Z.H.; Brus, L. Rayleigh and Raman scattering from individual carbon nanotube bundles. Journal of Physical Chemistry B, 2001, **105**, 1123-1134.

17. Milnera, M.; Kurti, J.; Hulman, M.; Kuzmany, H. Periodic resonance excitation and intertube interaction from quasicontinuous distributed helicities in single-wall carbon nanotubes. Physical Review Letters, 2000, **84**, 1324-1327.

18. Cheng, Q.H.; Debnath, S.; Gregan, E.; Byrne, H.J. Effects of chlorinated aromatic solvents on the dispersion of HiPco SWNTs. Physica Status Solidi B-Basic Solid State Physics, 2008, **245**, 1947-1950.

19. Kataura, H.; Kumazawa, Y.; Maniwa, Y.; Umezu, I.; Suzuki, S.; Ohtsuka, Y.; Achiba, Y. Optical properties of single-wall carbon nanotubes. Synthetic Metals, 1999, **103**, 2555-2558.

20. Jorio, A.; Fantini, C.; Dantas, M.S.S.; Pimenta, M.A.; Souza, A.G.; Samsonidze, G.G.; Brar, V.W.; Dresselhaus, G.; Dresselhaus, M.S.; Swan, A.K.; Unlu, M.S.; Goldberg, B.B.; Saito, R. Linewidth of the Raman features of individual single-wall carbon nanotubes. Physical Review B, 2002, **66**, 115411.

21. Nair, N.; Usrey, M.L.; Kim, W.J.; Braatz, R.D.; Strano, M.S. Estimation of the (n,m) concentration distribution of single-walled carbon nanotubes from photoabsorption spectra. Analytical Chemistry, 2006, **78**, 7689-7696.

22. Gregan, E.; Keogh, S.M.; Maguire, A.; Hedderman, T.G.; Neill, L.O.; Chambers, G.; Byrne, H.J. Purification and isolation of SWNTs. Carbon, 2004, **42**, 1031-1035.

23. Zhang, Y.Y.; Son, H.; Zhang, J.; Kong, J.; Liu, Z.F. Laser-heating effect on Raman spectra of individual suspended single-walled carbon nanotubes. Journal of Physical Chemistry C, 2007, **111**, 1988-1992.

CHAPTER 7
SOLVENT PARAMETERS AND DISPERSION LIMIT OF SWNTS

*Adapted from "***Systematic study of the dispersion of SWNTs in organic solvents***" J. Phys. Chem. C* **2010, 114, 4857.**

Authors: Qiaohuan Cheng, Sourabhi Debnath, Luke O'Neill, Theresa G. Hedderman, Elizabeth Gregan, Hugh J. Byrne

7.1 Introduction

The capability of a series of organic solvents to disperse and solubilise as-produced HiPco SWNTs in terms of the extinction/absorption coefficients has been evaluated in Chapter 5. As the extinction/absorption coefficients are calculated from the absorbance of the suspension/solution, the values reflect the amount of tubes suspended/dispersed in the solution. Based on the extinction/absorption coefficients observed for the range of solvents, polar forces and hydrogen bonding have previously been found to be dominant compared to dispersion forces both for chlorinated aromatic solvents and other solvents, although the correlation appeared to differ for the two sets of solvents [1]. In Chapter 6, however, no differentiation was observed between the structural profile of the nanotubes dispersed by *o*-DCB and DMF, the extremes of the two sets identified in Chapter 5. In order to more fully understand the

behaviour of SWNTs in a chosen solvent, a further parameter, the dispersion limit or critical debundling concentration, should be considered. The dispersion limit is a measure of the ease of dispersion of SWNTs in a solvent.

As has been mentioned in Chapter 5, the dispersion limit of SWNTs in a solvent can be obtained by plotting the aggregation fraction as a function of concentration. The concentration at which the aggregation ceases to dominate the dispersion as a result of exfoliation or debundling upon dilution is considered to be the dispersion limit (D_L) of SWNTs in the respective solvent [2]. The same method was adopted in this work to monitor the dispersibility of SWNTs in the employed solvents.

In this Chapter, the dispersion limit of as-produced HiPco SWNTs in a range of organic solvents was monitored and plotted as a function of the respective solvent Hildebrand and Hansen solubility parameters. Thirteen organic solvents were employed in this study. In order to further investigate the correlation between the dispersion limit and solvent Hildebrand and Hansen solubility parameters, based on the eight solvents investigated in Chapter 5, five additional solvents, 1, 2-dibromoethane (DBE), N-methyl-2-pyrrolidone (NMP), nitromethane, acetonitrile and dimethyl sulfoxide (DMSO), were added according to their solubility parameters.

AFM studies were employed to confirm that the centrifuged samples are dominated by isolated tubes and/or very small bundles at concentrations below the dispersion limit. Correlations between the dispersion limit and solvent solubility parameters are explored, demonstrating that SWNTs are easily dispersed in solvents with a Hildebrand solubility parameter range from ~22-24

$MPa^{1/2}$ and Hansen polarity component (δ_P) around ~12-14 $MPa^{1/2}$. Similar to the relationships previously determined for the extinction/absorption coefficients, the effect of dispersion force (δ_D) is not evident. However, whereas the extinction was previously observed to be correlated with the hydrogen bonding parameter (δ_H), no clear δ_H dependence of dispersion limit is observed here. Comparing to similar studies in literature, good agreement in terms of Hildebrand solubility parameters is seen here [3], but not in terms of Hansen solubility parameters. This disparity of the results reported here from those in literature is shown to be at least in part due to sonication conditions employed during sample preparation, which affect the degree of solubilisation but also the physical and/or chemical properties of the SWNTs themselves, bringing into question the validity of universal solubility parameters and suggesting the need for a systematic study of the sonication process and its dependence on solubility parameters.

7.2 Experimental Section

MCB, o-DCB, *m*-DCB, TCB, toluene, DMF, nitromethane, acetonitrile and DMSO were obtained from Sigma-Aldrich Ireland Ltd. DCE, and DBE were purchased from ACROS ORGANICS and Chloroform was obtained from Fisher Scientific Ireland. All the solvents were used as received.

HiPco SWNT (Carbon Nanotechnologies Inc., batch number PO341) dispersions were produced by sonicating in each solvent using a high power

ultrasonic tip processor (Ultrasonic processor VCX 750 W) at 26 % (195 W) output for 20 s, followed by serial dilution to produce a range of dispersions with concentrations from 0.21 mg/ml to 0.001 mg/ml. The volume of each sample was 5 ml. All samples were then sonicated for an additional 100 s [4] to make sure each sample received the same sonication treatment. All the dispersions were subsequently centrifuged at 3000 rpm (~945 g) (ECONOSPIN Sorvall Instruments) for 60 mins.

UV-Vis-NIR measurements were carried out on the whole sample before centrifuge (immediately before measurement all samples were vigorously shaken) but only the supernatant after centrifugation, so that the mass fraction of aggregates can be estimated (see Equation 4.2). All samples were allowed to settle for 2 days before centrifugation, to minimize the effects of solvent density and/or viscosity. The absorption coefficient for SWNTs in each solvent was calculated from the slope of the absorbance obtained in the integrating sphere as a function of as prepared concentration [1].

Raman measurements were performed with a LabRAM HR800 Raman Microscope (Horiba Jobin Yvon) at a laser energy of 2.33 eV (532 nm) on dispersions drop cast onto quartz substrates. A x50 objective lens was used for all the measurements. Up to ten spectra were taken randomly for each sample. The intensities of the D band and G^+ were taken after base line correction and the ratios of I_D/I_{G^+} were calculated for all spectra and averaged.

The samples for AFM were prepared by drop casting the supernatant onto cleaned quartz substrates. AFM images were acquired on a MFP-3D-BIOTM Atomic Force Microscope (Asylum Research) in tapping mode.

7.3 Results and Discussion

Figure 7.1 shows the concentration dependence of the aggregation fraction (calculated with the absorption at 660nm) for SWNTs in MCB, TCB and DMF dispersions. In TCB, the aggregate fraction after centrifugation is reduced to ~ 0.1, indicating almost complete debundling at concentrations below ~ 0.005 mg/ml, and an absorbance which is almost unaffected by centrifugation. However, in the dispersions of MCB, aggregates dominate the dispersion over the whole range of the concentration studied and are entirely removed by centrifugation. In this case, the dispersion limit of SWNTs in the corresponding solvent is considered to be <0.001 mg/ml.

It should be noted that, although the dispersion limit of SWNTs in DMF can be considered to be 0.022 mg/ml, the aggregation fraction below this limit is as high as 0.5. Nevertheless, the exfoliation of the SWNT bundles with dilution can be confirmed by AFM. Figure 7.2 shows the AFM images of the dispersion at ~ 0.0375 mg/ml and 0.0067 mg/ml in DMF. It is clearly seen that the bundle size decreases with decreasing concentration until, below the dispersion limit, the SWNTs exist as isolated tubes or very small bundles (2 - 3 nm).

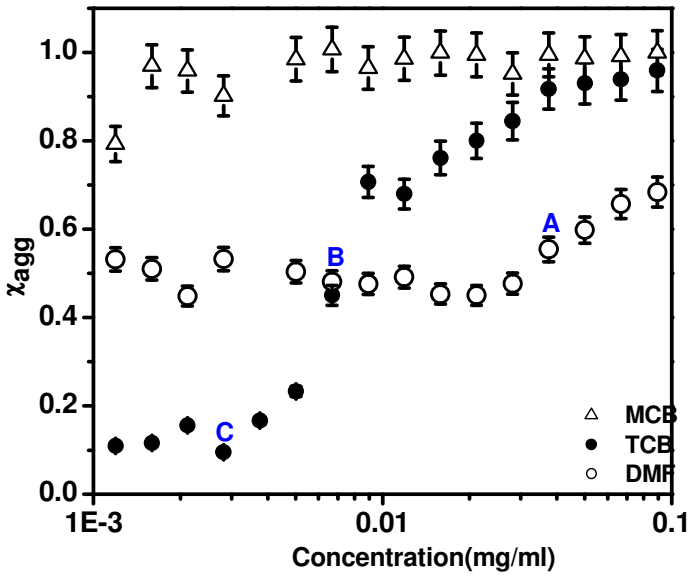

Figure 7.1 Fraction of the nanotube aggregates in MCB, TCB and DMF dispersions as a function of prepared concentration. Two samples of SWNT/DMF dispersions with concentration of 0.0375 mg/ml (A) and 0.0067 mg/ml (B) and one sample of SWNT/TCB dispersion at concentration of 0.00282 mg/ml (C) were studied by AFM.

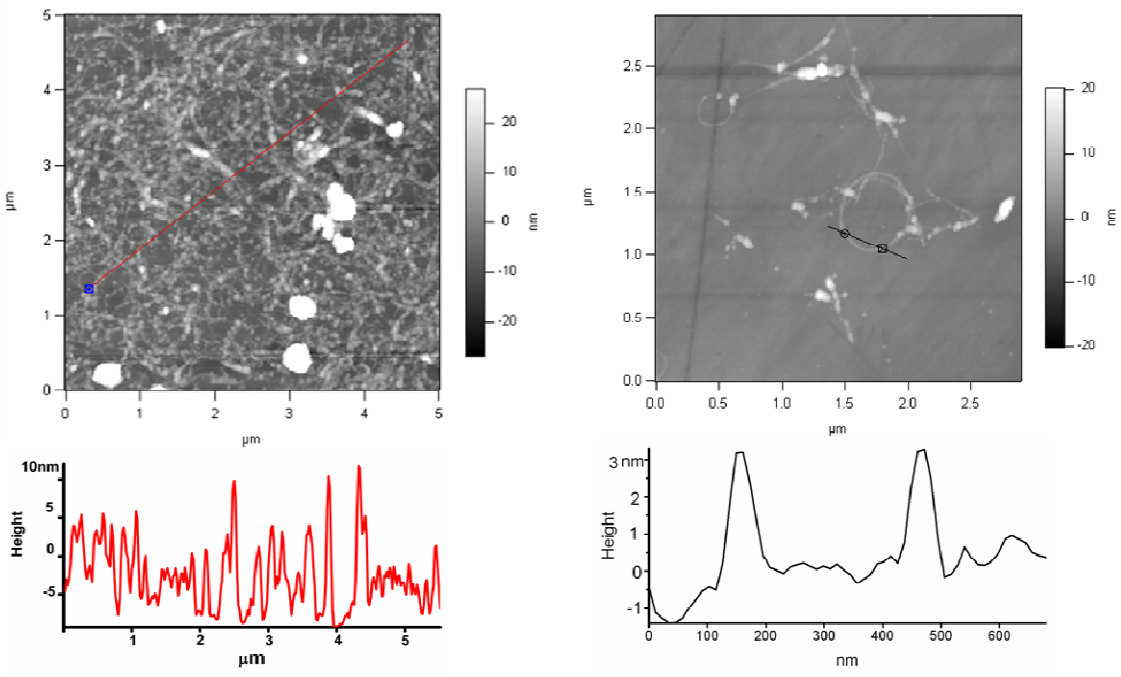

(a) (b)

Figure 7.2 AFM images of SWNT/DMF dispersions after centrifugation, (a) 0.0375 mg/ml, (b) 0.0067 mg/ml.

Table 7.1 The Hildebrand solubility parameter and Hansen solubility parameters of the solvents and the dispersion limits (D_L) of SWNTs in different solvents, together with the aggregation fraction (χ_{agg}) below dispersion limit in each solvent and absorption coefficient.

Name	Molecular formula	δ_D[5] (MPa$^{1/2}$	δ_P[5] MPa$^{1/2}$	δ_H[5] MPa$^{1/2}$	δ[6] MPa$^{1/2}$	D_L mg/ml	χ_{agg} below D_L	Absorption coefficient mlmg^{-1}m^{-1}
Chloroform	$CHCl_3$	17.8	3.1	5.7	18.9	0.001	0.4	1424
DCE	CH_2ClCH_2Cl	19.0	7.4	4.1	20.3	0.007	0.6	1724
DMF	$HCON(CH_3)_2$	17.4	13.7	11.3	24.0	0.022	0.5	2220
Toluene	C_7H_8	18.0	1.4	2.0	18.2	<0.001	0.95	1349
MCB	C_6H_5Cl	19.0	4.3	2.0	19.4	<0.001	0.9	1196
o-DCB	$C_6H_4Cl_2$	19.2	6.3	3.3	20.5	0.015	0.25	1650
m-DCB	$C_6H_4Cl_2$	19.7	5.1	2.7	20.1	0.004	0.4	1313
TCB	$C_6H_3Cl_3$	20.2	6.0	3.2	20.3	0.005	0.1	1658
DBE	CH_2BrCH_2Br	17.8	6.4	7.0	21.3	0.010	0.25	2593
Nitromethane	CH_3NO_2	15.8	18.8	5.1	25.8	<0.001	0.9	911
NMP	C_5H_9NO	18.0	12.3	7.2	22.8	0.020*	0.1*	3264*
Acetonitrile	CH_3CN	15.3	18.0	6.1	24.2	<0.001	0.98	641
DMSO	$(CH3)_2SO$	18.4	16.4	10.2	26.6	0.006	0.65	1785

* Data from reference [2].

The dispersion limit of SWNTs in each solvent is listed in Table 7.1, together with the solvent solubility parameters of the respective solvent and the aggregation fraction below the dispersion limit. Figure 7.3 shows the location of the solvents employed in Hansen parameter space, the size of the spheres indicating the dispersion limit of SWNTs in the corresponding solvent. It is seen that the solvents employed occupy a wide range of polarity and hydrogen bonding values. However, it should be noted that the dispersion force values do not vary significantly over the range of solvents used, most values being located between 17 MPa$^{1/2}$ to 20 MPa$^{1/2}$. Although several successful solvents appear

in this range, it is not an appropriate parameter for defining a “good” solvent of SWNTs, as many solvents with similar values of δ_D are “poor” solvents.

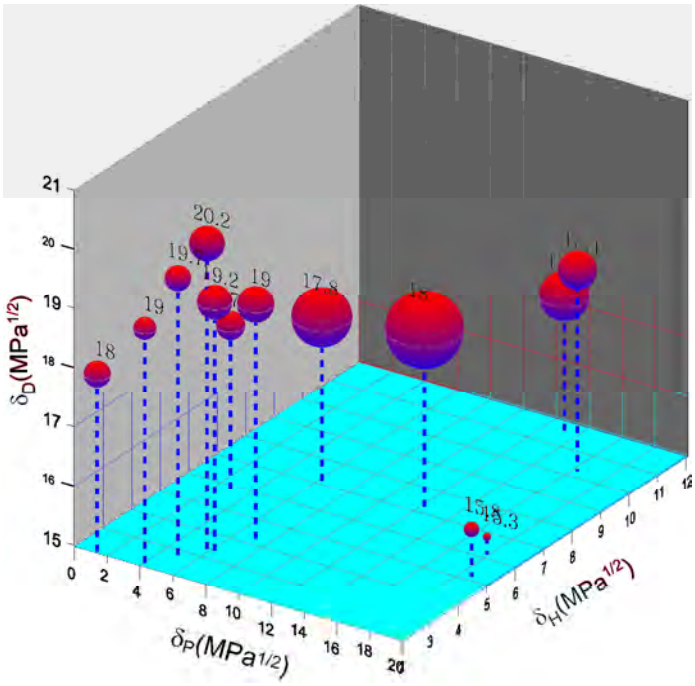

Figure 7.3 Position of the employed solvents in Hansen parameter space, the size of the sphere indicates the ease of dispersion of SWNTs (dispersion limit) in the corresponding solvent. For the dispersion limit below 0.001 mg/ml, 0.0005 mg/ml is used to indicate the sphere size.

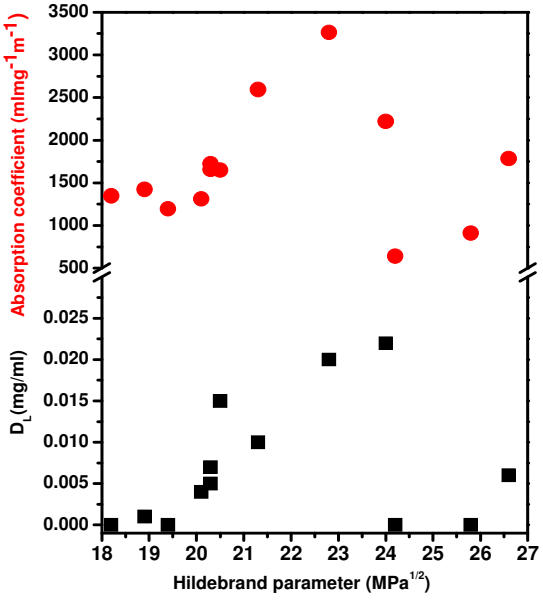

Figure 7.4 Absorption coefficients and Dispersion limits as a function of Hildebrand parameter.

For comparison, the absorption coefficients [1] and the dispersion limits of SWNTs in different solvents are plotted against the solvent solubility parameters in one plot. Figure 7.4 shows the absorption coefficient and dispersion limit of SWNTs in the solvents as a function of the corresponding Hildebrand solubility parameter. It is seen that the results of the absorption measurements match well with those of the dispersion limit. It was reported in a previous study of the absorption coefficient *vs* Hildebrand solubility parameter that the chlorinated aromatic solvents and others can be fitted by two different trends (Chapter 5, [1]). When more solvents are included, however, it appears more appropriate to consider that both the absorption coefficient and dispersion limit are sharply peaked within a specific Hildebrand range, ~22-24 $MPa^{1/2}$. This value agrees very well with the theoretical calculation of the Hildebrand solubility parameters, which was found to be 23 $MPa^{1/2}$ for SWNTs of 1 nm diameter [7]. Bergin *et al.* also reported the Hildebrand solubility parameter for HiPco SWNTs to be sharply peaked at 21 $MPa^{1/2}$ [3], which is comparable to that indicated here. Solvents which have lower or higher Hildebrand solubility parameter have inferior dispersibility of bundled HiPco SWNTs and notably acetonitrile, with a value of δ = 24.2, shows very poor dispersion of SWNTs. The narrow range of the distribution can be attributed to the general requirement that the Hildebrand parameter of the solvent match that of the solute [8]. There is considerable spread and indeed asymmetry in the results of Figure 7.4, however, suggesting that the Hildebrand parameter is not specific enough to describe the interaction between the solvent and SWNTs, and that the interaction may better be understood by examining correlations with the more specific Hansen parameters.

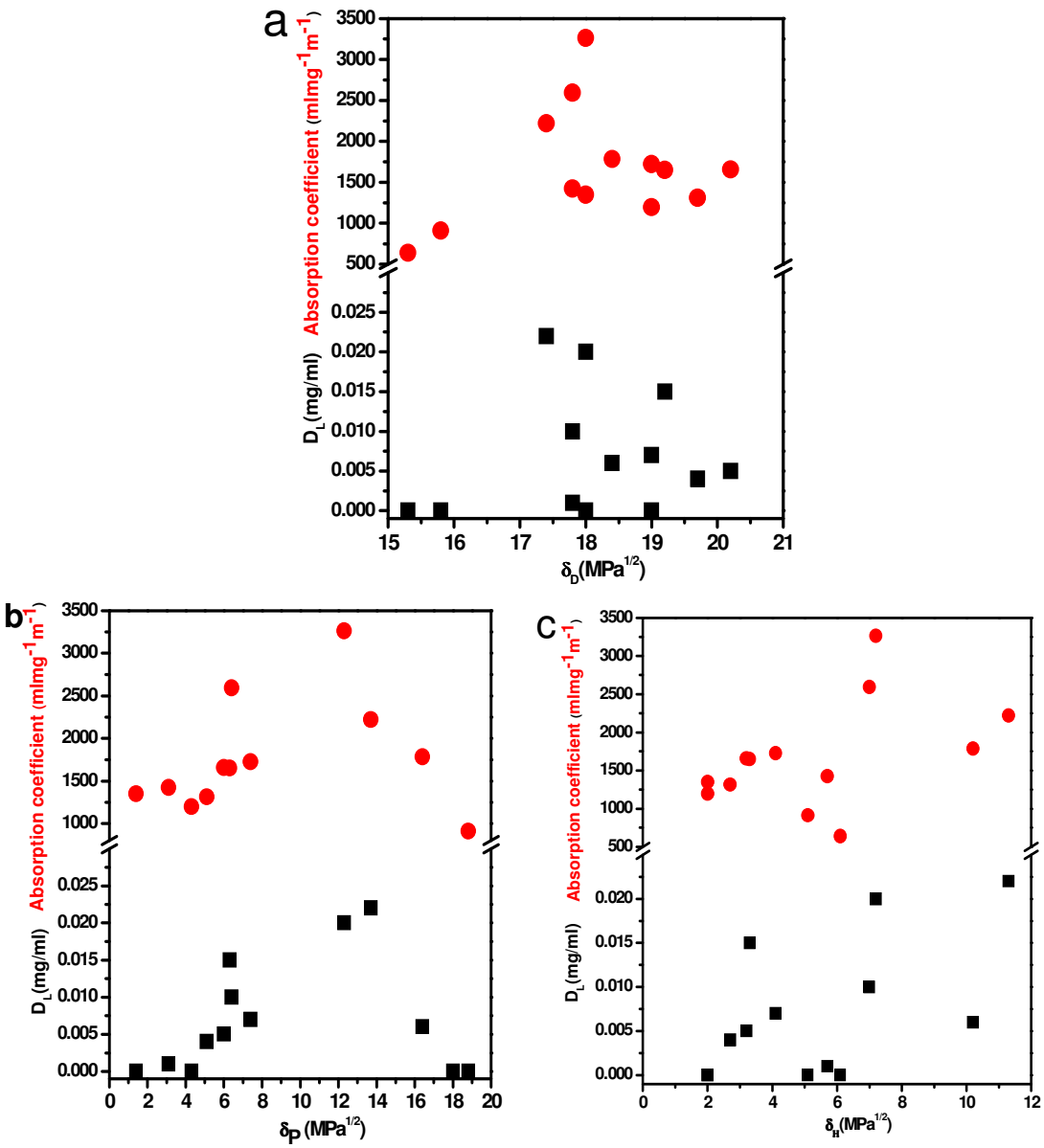

Figure 7.5 Absorption coefficients and Dispersion limits of SWNTs in each solvent *vs* (a) dispersion component (δ_D), (b) polar component (δ_P), and (c) hydrogen-bonding component (δ_H).

The correlations between absorption coefficient and dispersion limit and each of the three-dimensional Hansen solubility parameters are plotted and shown in Figure 7.5. Figure 7.5 (a) shows the distribution of the points as a function of δ_D, and no clear correlation is observed between the absorption coefficients and dispersion limits. Although several successful solvents appear in the range ~ 17 - 19 $MPa^{1/2}$, some solvents with δ_D within this range do not give good SWNT

dispersions, and therefore it is deemed that this factor is not an adequate parameter to predict a "good" solvent for SWNTs. Figure 7.5 (b) indicates the correlation between the absorption coefficient and dispersion limit *vs* the dipole-dipole force of the solvents (δ_P). It is clearly seen that among the employed solvents, both the absorption coefficient and dispersion limit show a maximum in the δ_P range from ~ 12 - 14 $MPa^{1/2}$. This range is quite different to the value reported in the study of Bergin *et al*., in which a peak of dispersion limit was observed at $\delta_P \approx 7.5$ $MPa^{1/2}$ [3], although there does appear to be a local maximum at ~ 6.5 $MPa^{1/2}$ [9]. The distribution of the points as a function of the Hydrogen-bonding force (δ_H) is shown in Figure 7.5(c). The consistency of dispersion limit and absorption is less apparent compared to the plot of δ_P. Although the solvents with $\delta_H \approx 7$ $MPa^{1/2}$ show better solubility of SWNTs compared to other solvents, no clear correlation between dispersion limit and absorption coefficient was observed for the employed solvents.

Although the results of Figure 7.4 agree well with previous reports in terms of the optimum range of the Hildebrand parameter, there is significant discrepancy in terms of the optimal values of the Hansen parameters which should indicate the mechanisms underlying, and lead to a greater understanding of, the solubilisation process.

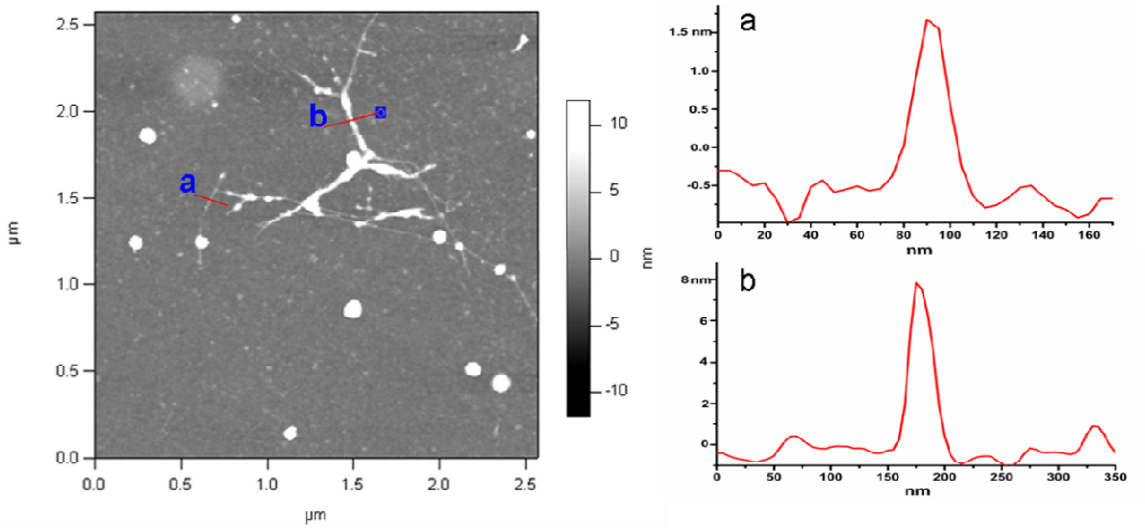

Figure 7.6 AFM image of DMF dispersion at ~ 0.003 mg/ml precentrifugation.

A critical consideration in the intercomparison of studies is the sample preparation conditions. It is clear that, in Figure 7.1, although DMF shows the highest dispersion limit of the employed solvents at ~ 0.022 mg/ml, the aggregation fraction below the dispersion limit is as high as 0.5, indicating that only partial debundling has occurred. Indeed, the AFM image shown in Figure 7.6 shows that, precentrifugation, the sample contains a significant number of bundles at a concentration of ~0.003 mg/ml. In Table 7.1, it can be seen that the aggregation fractions below the dispersion limit of SWNTs in different solvents vary significantly and do not correlate with their ability to disperse SWNTs (dispersion limits). In order to explore this, a further two sets of SWNT/DMF dispersions were sonicated for 4 mins and 6 mins respectively. The aggregation fractions for different sonication times were plotted as a function of prepared concentration, and compared to those presented in Figure 7.1, and are shown in Figure 7.7. It is clear that the degree of debundling below the dispersion limit is critically dependent on sonication time. The estimated dispersion limit however appears to be unaffected by the degree of sonication

indicating that it may be determined by the solvent parameters rather than the sonication treatment.

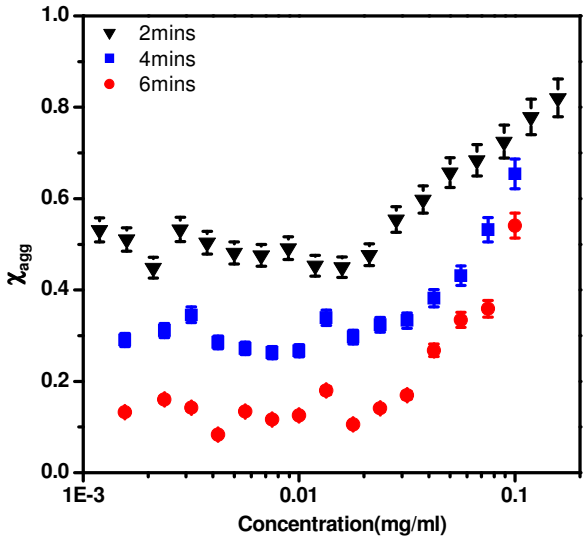

Figure 7.7 Aggregation mass fractions of SWNTs in DMF at different sonication time (volume 5ml, without temperature control).

Furthermore, it has been established that sonication not only helps to exfoliate the nanotube bundles, but also results in a cutting of the SWNTs or the introduction of defects on their side walls. Damage of the tubes can be monitored by the intensity of the D band of the Raman spectrum compared to that of the corresponding G^+ band, the $I_D/I_G{}^+$ ratio [10]. Raman spectra of SWNTs extracted from DMF dispersion, sonicated for different times, were taken and the ratio $I_D/I_G{}^+$ was calculated and plotted as a function of sonication time.

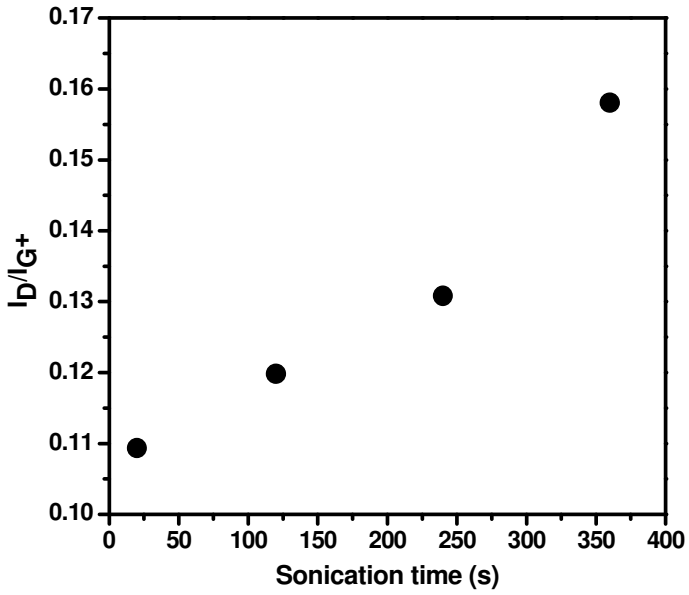

Figure 7.8 I_D/I_G^+ ratio as a function of sonication time for SWNT/DMF samples.

As shown in Figure 7.8, the I_D/I_G^+ ratio increases significantly as the sonication time is increased, indicating that, although longer sonication time increases the debundling of SWNTs in solution, this is at the expense of alteration of the physical and/or chemical properties of the tubes themselves and that damage to the SWNTS is evident even at lower sonication times. Thus, the very nature of the SWNTs and therefore their solubility, is also dependent on the sonication time and the identification of a characteristic and unique set of solubility parameters is difficult. In the study of Bergin *et al*. [3], each sample was sonicated for 30 mins with ice cooling, whereas in the work of Detriche *et al***.** [9, 11], each sample was sonicated for 2 mins by a tip sonicator. In their study of HiPco nanotubes from Unidym, Bergin *et al*. identified optimal solubilisation for solvent Hildebrand parameters in the range 19 < δ < 24 $MPa^{1/2}$, with a maximum at 21 $MPa^{1/2}$. The corresponding optimal ranges for the Hansen parameters were, δ_D : 17 < δ_D < 19 $MPa^{1/2}$, δ_P: 5 < δ_P < 14 $MPa^{1/2}$, δ_H : 3 < δ_H

<11 $MPa^{1/2}$, and the estimated parameters for SWNTs were δ_D = 17.8 $MPa^{1/2}$, δ_P = 7.5 $MPa^{1/2}$, δ_H = 7.6 $MPa^{1/2}$. In the study of Detriche *et al.* of CVD SWNTs (with average diameter of 2 nm), no details of sonication conditions are given, but the samples are additionally purified by concentrated HCl. The optimal Hildebrand range is $20 < \delta < 22 MPa^{1/2}$, with Hansen parameters δ_D : $19 < \delta_D < 21$ $MPa^{1/2}$, δ_P : $4 < \delta_P < 7$ $MPa^{1/2}$, δ_H: $3 < \delta_H < 5$ $MPa^{1/2}$, and the estimated parameters for SWNTs were: δ_D = 19.4 $MPa^{1/2}$, δ_P = 6.0 $MPa^{1/2}$, δ_H = 4.5 $MPa^{1/2}$. A further study by Ham *et al.* utilized purified HiPco SWNTs sonicated for 20 hrs and identified δ_D the most important parameter with values in the range $17 < \delta_D < 18$ $MPa^{1/2}$, δ_P as having an upper limit of 14 $MPa^{1/2}$, and δ_H an upper limit of 12 $MPa^{1/2}$. There is thus considerable discrepancy between the studies already reported in literature and it is notable that the types of nanotubes and the preparation conditions vary significantly between studies.

Sonication can also affect changes to the solvent characteristics, further complicating any correlation to solubility parameters. As shown in Figure 7.9, in the TCB dispersion, a foreign coating on the SWNTs is evident, as previously reported in *o*-dichlorobenzene SWNT/*o*-DCB dispersions [12], although the sonication time in this study is only 2 mins compared to that of 3 mins- 60mins in reference [12]. It was reported that in *o*-DCB dispersions, sonication caused the decomposition and polymerization of *o*-DCB and the sonopolymer coated on the tubes was proposed to contribute to the stabilization of SWNT in *o*-DCB suspension [12]. Similarly, the observation of the sonopolymer in SWNT/TCB samples might be responsible for the low aggregation fraction in TCB and the high dispersion limit of SWNTs in *o*-DCB. However, MCB, which has a similar

structure to that of *o*-DCB and TCB, is a poor solvent for SWNTs and so correlations of such effects to solvent molecular structure are difficult.

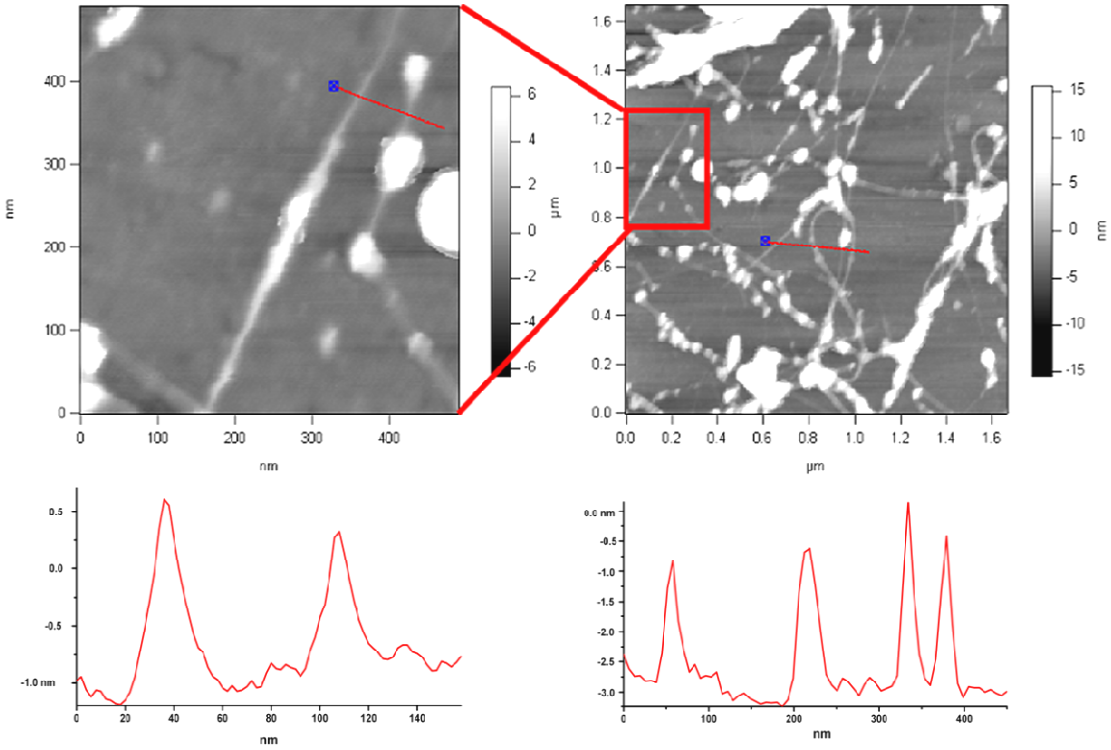

Figure 7.9 AFM images of SWNTs dispersed in TCB at 0.00282 mg/ml.

7.4 Summary

Systematic studies of the interaction of SWNTs with organic solvents are critical to developing an understanding of solubilisation mechanisms and thus an optimisation of processing protocols. Good agreement with literature is demonstrated here in terms of Hildebrand parameters, but not in terms of the Hansen solubility parameters. It has been demonstrated that the degree of dispersion is critically dependent on sample preparation conditions, in particular

sonication. Prolonged sonication clearly causes progressive physical and/or chemical modification of the SWNTs, however, and given that the material to be solubilised is ill defined, it is difficult to justify a universal or characteristic solubility parameter. The results indicate that further systematic investigation of the sonication process is merited in order to differentiate the solubilising effects from the results of physical and/or chemical modification of the samples themselves.

7.5 References

1. Cheng, Q.H.; Debnath, S.; Gregan, E.; Byrne, H.J. Effect of Solvent Solubility Parameters on the Dispersion of Single-Walled Carbon Nanotubes. Journal of Physical Chemistry C, 2008, **112**, 20154-20158.
2. Giordani, S.; Bergin, S.D.; Nicolosi, V.; Lebedkin, S.; Kappes, M.M.; Blau, W.J.; Coleman, J.N. Debundling of single-walled nanotubes by dilution: Observation of large populations of individual nanotubes in amide solvent dispersions. Journal of Physical Chemistry B, 2006, **110**, 15708-15718.
3. Bergin, S.D.; Sun, Z.Y.; Rickard, D.; Streich, P.V.; Hamilton, J.P.; Coleman, J.N. Multicomponent Solubility Parameters for Single-Walled Carbon Nanotube-Solvent Mixtures. Acs Nano, 2009, **3**, 2340-2350.
4. Cheng, Q.H.; Debnath, S.; Gregan, E.; Byrne, H.J. Effects of chlorinated aromatic solvents on the dispersion of HiPco SWNTs. Physica Status Solidi B-Basic Solid State Physics, 2008, **245**, 1947-1950.

5. Hansen, C. Hansen Solubility Parameters: A User's Handbook. 1999, CRC Press.

6. Abboud, J.L.M.; Notario, R. Critical Compilation of Scales of Solvent Parameters. Part I, Pure, non-Hydrogen bond Donor Solvents. Pure Applied Chemistry, 1999, **71**, 645-718.

7. Maiti, A.; Wescott, J.; Kung, P. Nanotube-polymer composites: insights from Flory-Huggins theory and mesoscale simulations. Molecular Simulation, 2005, **31**, 143-149.

8. Hildebrand, J. H.; Prausnitz, J. M.; Scott, R.L. Regular and related solutions. 1970, Van Nostrand Reinhold Company.

9. Detriche, S.; Zorzini, G.; Colomer, J.F.; Fonseca, A.; Nagy, J.B. Application of the Hansen Solubility Parameters Theory to Carbon Nanotubes. Journal of Nanoscience and Nanotechnology, 2008, **8**, 6082-6092.

10. Giordani, S.; Bergin, S.; Nicolosi, V.; Lebedkin, S.; Blau, W.J.; Coleman, J.N. Fabrication of stable dispersions containing up to 70% individual carbon nanotubes in a common organic solvent. Physica Status Solidi B-Basic Solid State Physics, 2006, **243**, 3058-3062.

11. Detriche, S.; Nagy, J.B.; Mekhalif, Z.; Delhalle, J. Surface State of Carbon Nanotubes and Hansen Solubility Parameters. Journal of Nanoscience and Nanotechnology, 2009, **9**, 6015-6025.

12. Niyogi, S.; Hamon, M.A.; Perea, D.E.; Kang, C.B.; Zhao, B.; Pal, S.K.; Wyant, A.E.; Itkis, M.E.; Haddon, R.C. Ultrasonic dispersions of single-walled carbon nanotubes. Journal of Physical Chemistry B, 2003, **107**, 8799-8804.

CHAPTER 8
ULTRASOUND-ASSISTED SWNT DISPERSION IN SOLVENTS

*Adapted from "***Ultrasound-assisted SWNTs dispersion: effects of sonication parameters and solvent properties***" J. Phys. Chem. C* **2010, 114, 8821.**

Authors: Qiaohuan Cheng, Sourabhi Debnath, Elizabeth Gregan, Hugh J. Byrne

8.1 Introduction

Chapter 7 described the systematic study of the correlation between the dispersion limit of SWNTs in different solvents as a function of solvent solubility parameters. It was found that SWNTs are easily dispersed in solvents with Hildebrand solubility parameter ranges from ~22-24 $MPa^{1/2}$ and Hansen polarity components (δ_P) ~12-14 $MPa^{1/2}$. No clear correlation between dispersion limits and the dispersion force (δ_D) or hydrogen bonding force (δ_H) were evident [1].

There is considerable discrepancy between the studies reported here and those already reported in literature and it is notable that the types of nanotubes and the preparation conditions vary significantly between studies. Notably, ultrasonication is universally employed to assist the dispersion and stabilization of SWNTs [1-7]. However, there is no standard procedure for the sonication process, different groups applying different sonication treatment to their

samples. Table 8.1 summarizes some of the sonication parameters which have been used for dispersing and stabilizing SWNTs in liquids. It is clearly seen that the sonication conditions vary significantly, including sonicator types, sonication times and temperature control. For example, the sonication times vary from 2 mins to 30 mins for tip sonication and 30 mins to 20 hrs for bath sonication.

Table 8.1 Different sonication conditions for dispersing SWNTs in liquid

Sonicator type	Solvent	Sonication time	Reference
Bath & Tip Sonicators	Water (surfactant)	1min (tip) + 20s (tip) +3hrs (bath)	[8]
Bath sonicator	Organic solvents & water (surfactant)	20hrs	[9]
Tip Sonicator	Organic solvents	30mins (ice cooling)	[6]
Tip sonicator	Organic solvents	2mins	[10]
Tip Sonicator	Organic solvents	2 mins	[11]
Bath sonicator	Amide Solvents	4hrs	[2]
Bath & Tip Sonicators	N-methyl-2-pyrrolidone	2mins (tip) + 4hrs (bath) +1min (tip)	[3]
Bath sonicator	Alkyl Amide Solvents	30mins (40°C)	[5]
Bath sonicator	ortho-dichlorobenzene	1 hr	[12]

The strong shear force which can exfoliate the SWNT bundles during sonication comes from the cavitation process, which entails bubble formation, growth and collapse. This process is intimately dependant on many factors [13], including: (a) The nature of the solvent, notably the solvent viscosity, surface tension, vapour pressure, gas solubility and type of active intermediates or radicals formed.

(b) The nature of gas solubilised in the liquid which can change the number of cavitation events and gas content.

(c) Ambient liquid temperature and pressure. As many of the solvent parameters are temperature dependent, a change of temperature will affect the liquid properties and the gas solubility.

(d) Applied intensity. The intensity of ultrasound influences the size of cavitation and therefore the probability of cavitation events per unit volume. The larger the intensity the larger will be the acoustic amplitude and collapse pressure and hence the faster and more violent the collapse.

(e) Ultrasound frequency. While the acoustic frequency is increased, the size of the cavitation bubble decreases, which will influence the cavitation threshold. An increase in frequency means shorter acoustic periods, lower maximum bubble size, and thus less cavitation intensity.

(f) The sonication time which determines the total energy input. Many of these parameters are interrelated, as for instance, most of the solvent parameters are also temperature dependent, therefore, increasing the complexity of the study.

To further complicate the issue, it has been reported that strong sonication cannot only exfoliate the SWNT bundles but also induce defects and even scission of the tubes [14]. The damage of the SWNTs is normally monitored by Raman spectroscopy, an increase of the intensity of the defect or D band compared to the corresponding graphitic or G band intensity being considered to be a measure of damage to the tubes [3, 15].

In this Chapter, a study of the effect on the debundling of SWNTs in different solvents is conducted. In the plot of aggregation fraction as a function of as-

prepared concentration, the debundling and dispersion process, as characterised by the dispersion limit and the aggregation fraction, is seen to correlate well with the solvent parameters associated with sonication suggesting that these rather than the solubility parameters govern the dispersion process. Raman spectroscopy of *o*-DCB and DMF dispersions demonstrates significant damage to the SWNTs which is well correlated with the increased solubility suggesting that the use of universal solubility parameters is not appropriate.

8.2 Experimental Section

HiPco SWNTs from Carbon Nanotechnologies Inc., batch number PO341, were used as received.

All the sonication treatments in this study were carried out using an Ultrasonic processor VCX 750W (SONICS & MATERIALS, INC.), of frequency 20 kHz with the output power set at 26% (195 W).

4.2 mg SWNTs were added into 20 ml solvent. The initial dispersion was produced by sonicating for 20 s, whereupon it was serially diluted to produce a range of dispersions with concentrations from 0.21 mg/ml to 0.001 mg/ml. The volume of each sample was 5 ml. All samples were then sonicated for an additional 100 s [16] to make sure each sample received the same sonication treatment. All the dispersions were subsequently centrifuged at 3000 rpm (~ 945 g) (ECONOSPIN Sorvall Instruments) for 60 mins. An identical procedure was performed in all the employed solvents.

In order to investigate the effect of sonication time and output power of the sonicator, dispersions in two solvents, *o*-DCB and DMF, were chosen. 3.2 mg SWNTs were added to 80 ml *o*-DCB and DMF respectively (0.04 mg/ml). This initial dispersion was sonicated for 20 s with the output power of the sonicator set as 26% (195W). The dispersion was then immediately divided into 16 bottles, each sample containing 5 ml. 6 samples of each solvent were chosen for the study of output power of the sonicator. The output power of the sonicator was varied between 21% (157.5W) and 38% (285W). The remaining 10 samples were used to investigate the effect of sonication time from 20 s to 220 s, in 20 s intervals for each sample. All the samples were allowed to settle for 2 days before a mild centrifugation was carried out to remove large aggregates.

UV-Vis-NIR absorption measurement (Perkin-Elmer Lambda 900) measurements were performed both before and after centrifugation. Before centrifugation samples were vigorously shaken before measurement for accurate assessment of A_{before} (Equation 4.2). All samples were then allowed to settle for 2 days before centrifugation, to minimize the effects of solvent density and/or viscosity. The supernatant was then extracted for centrifugation and characterization by UV-vis-NIR absorption spectroscopy to evaluate A_{after}. The mass fraction of aggregates was then estimated according to Equation 4.2. 10-mm quartz cuvettes were used for all the measurements. The absorbance at a wavelength of 660 nm was used for all the calculations [3, 10, 16].

Raman measurements were performed with a LabRAM HR800 Raman Microscope (Horiba Jobin Yvon) at laser energy 2.33 eV (532 nm) on the

supernatant of each sample (after centrifuge) drop cast onto glass substrates. A ×50 objective lens was used for all the measurements. The spot size and laser power at the sample were approximately 2 μm and 30.6 mW respectively. Up to ten spectra were taken randomly for each sample. The intensities of the D and G^+ bands were taken after base line correction and the ratios of I_D/I_{G^+} were calculated for all spectra and averaged.

8.3 Results and Discussion

As has been described in Chapter 7 (Figure 7.1), for the range of solvents, in addition to the variation of the dispersion limit, the aggregation fractions below D_L also vary significantly for the different solvents, but the two are not correlated. By comparing the dispersion limit and aggregation fraction below D_L for 3 sets of SWNT/DMF dispersions sonicated for 2 mins, 4 mins and 6 mins respectively, it was found that the estimated dispersion limit appears to be largely unaffected by the degree of sonication, although, sonication is critical to the degree of debundling (Chapter 7). The dispersion limit and aggregation fraction of SWNTs below D_L in each solvent are listed in Table 8.2, together with some of the physical parameters of the solvents, including molecular weight, viscosity, vapour pressure, density and surface tension.

Table 8.2 The dispersion limits of SWNTs and aggregation fraction below D_L in different solvents together with the solvents physical parameters (all the samples get 2 mins sonication).

Name	D_L (mg/ml)	χ_{agg} below D_L	Mw (g/mol)	Viscosity (mPa·s)	Vapour pressure (mm Hg)	Surface tension (mN/m)	Density (g/cm^3)
Chloroform	0.001	0.4	119.38	0.57*	159*	26.67**	1.48
DCE	0.007	0.6	98.96	0.84*	65.2*	24.07**	1.253
DMF	0.022	0.5	73.09	0.92*	2.7*	36.4**	0.944
Toluene	<0.001	0.95	92.14	0.59*	22*	27.93**	0.8669
MCB	<0.001	0.9	112.56	0.80*	11.8**	32.99**	1.11
o-DCB	0.015	0.25	147.01	1.324**	1.2*	37*	1.30
m-DCB	0.004	0.4	147.01	1.023***	2.145**	35.43**	1.288
TCB	0.005	0.1	181.45	1.611***	0.3**	****	1.50
DBE	0.010	0.25	187.86	1.629***	11*	39.55**	2.17
Nitromethane	<0.001	0.9	61.04	0.61**	27.8*	36.53**	1.138
Acetonitrile	<0.001	0.98	41.05	0.3443**	73*	28.66**	0.786
DMSO	0.006	0.65	78.13	1.996*	0.417*	42.92**	1.1004

* Data at 20 ℃, ** data at 25 ℃, *** data at 30 ℃, **** Not found in literature

In order to further investigate the effect of sonication time on the dispersion of SWNTs, a series of 0.04 mg/ml SWNTs in *o*-DCB and DMF dispersions were made with sonication times varying from 20 s to 220 s. The absorbance of each sample after centrifugation was measured by UV-Vis-NIR spectroscopy and plotted as a function of the sonication time (t), and is shown in Figure 8.1. It is clearly seen that increased sonication time increases the dispersion of SWNTs in both solvents. In *o*-DCB, the absorbance appears to reach a plateau in the region 120-160 s, whereas in DMF the absorbance continues to increase upon sonication up to ~ 200 s.

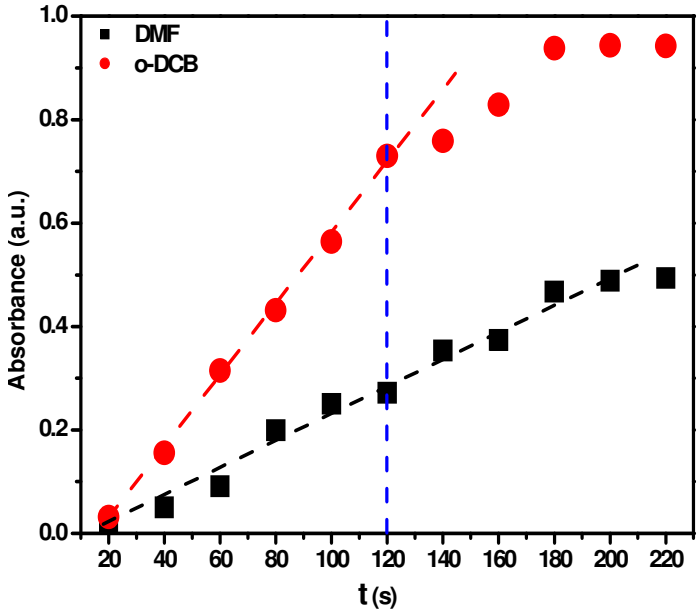

Figure 8.1 Absorbance of 0.04 mg/ml SWNTs in o-DCB and DMF after centrifugation as a function of sonication time (t) (the vertical blue line indicates the sonication time applied in previous studies [8, 21], Chapter 4. The Red and Black lines are guide to the eye).

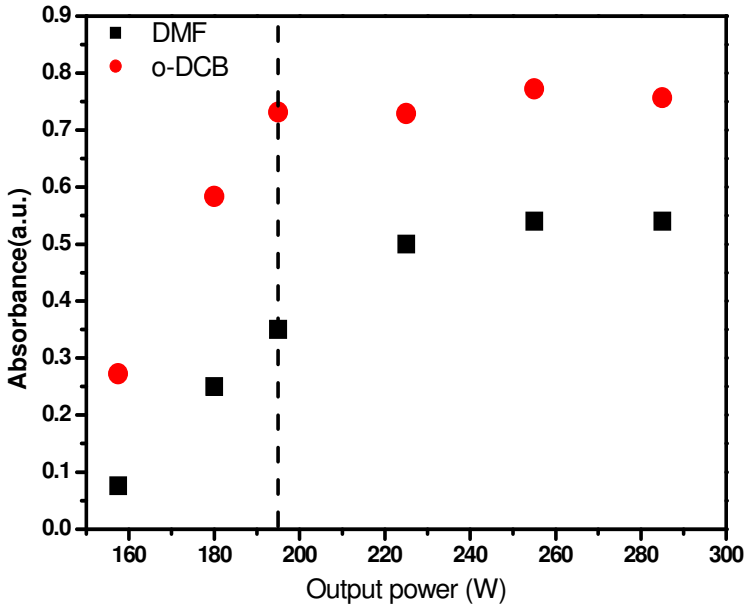

Figure 8.2 Absorbance of 0.04 mg/ml DMF and *o*-DCB dispersions after centrifuge as a function of sonicator output power (the vertical line indicates the output power used in previous studies [8, 21], Chapter 4).

Figure 8.2 shows the absorbance of the SWNT dispersions in *o*-DCB and DMF at 0.04 mg/ml as a function of sonication power for a fixed time of 120 s. The absorbance of *o*-DCB solution reaches a maximum for an output power of 26% (195 W). However, for the DMF solution, the optimum output power was found to be 30% (225 W). The sonication conditions of 120 s and 26% (195 W) output power were established in the previous study for *o*-DCB, wherein it was observed that the absorbance before centrifugation was seen to be maximized (Chapter 4). Clearly this is not quite the case for the dispersions after sonication, but most importantly, the optimal sonication conditions are solvent dependent.

According to the theory of ultrasonic processes, the cavitation effect is strongly dependent on solvent parameters, notably the solvent vapour pressure, viscosity and surface tension [13]. The aggregation fractions of the dispersions of SWNTs in different solvents, sonicated for 2 mins at 26% (195 W) output power, were plotted as a function of the solvent vapour pressures, shown in Figure 8.3. There is clearly a correlation between the aggregation fraction of SWNTs in each solvent and the solvent vapour pressure although a number of “outliers” are apparent. The aggregation fraction drops significantly when the vapour pressure of the solvent is below 10 mm Hg, indicating that sonication in solvents with lower vapour pressure more effectively debundles and disperses the SWNT aggregates. In low vapour pressure solvents, more energy is require to induce cavitation, and consequently more energy is released upon bubble collapse. This energy is then available to aid in the dispersion of SWNTs [13].

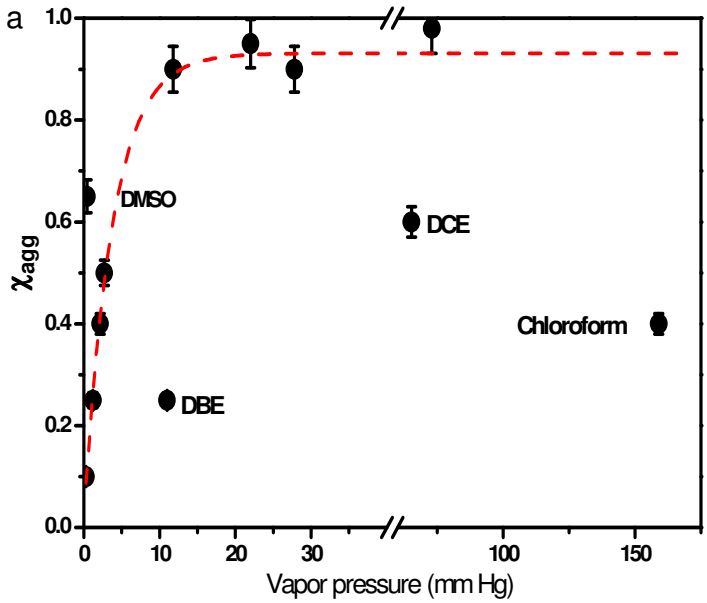

Figure 8.3 Aggregation fractions of SWNTs below the dispersion limits in each solvent as a function of the solvent vapour pressure. The dashed line is a fit of an exponential dependence of (1- χ_{agg}) on the solvent vapour pressure.

In sonochemistry, the variation of the decomposition rate of, for example, $Fe(CO)_5$ in organic solvents is strongly dependent on the vapour pressure, a linear correlation between ln (k), where k is the decomposition rate constant, and solvent vapour pressure being observed [17]. If the debundling process of nanotube aggregates is comparable to the decomposition of $Fe(CO)_5$, a similar correlation should be observed. The dashed line of Figure 8.3 is a model of an exponential dependence of (1- χ_{agg}), representing the debundling rate, on the solvent vapour pressure. Excluding the “outliers”, an excellent correspondence is observed indicating that the debundling process can be modelled according to the principles of sonochemistry.

Figure 8.4 shows the aggregation fraction below the dispersion limit in each solvent as a function of solvent viscosity. Again a good correlation is observed, as indicated by the trend line, again with some “outliers”. Notably, the outliers

are also outliers in Figure 8.3. Lower aggregation fraction and therefore better dispersion is observed in higher viscosity solvents. Although viscous solvents are known to increase the threshold of the cavitation [18], the effects resulting from cavitation collapse in viscous liquids are stronger than collapse in less viscous liquid, resulting in more efficient debundling of SWNTs [18].

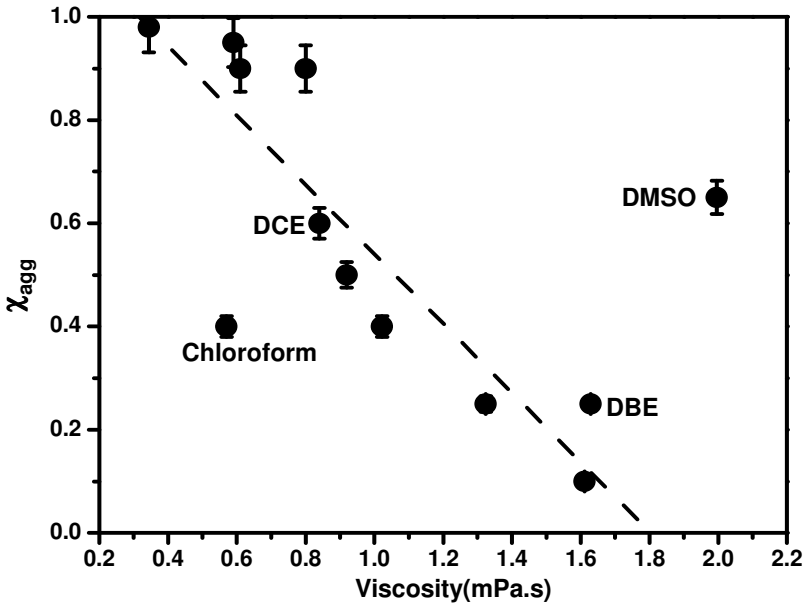

Figure 8.4 Aggregation fractions of SWNTs below the dispersion limits in each solvent as a function of the solvent viscosity. The dashed line is a guide to the eye.

Figure 8.5 shows the aggregation fraction as a function of solvent surface tension. If DMSO, DCE, and chloroform are again assumed to be anomalous, then a reasonable correlation between the aggregation fraction and the solvent surface tension may be inferred. As is the case for viscosity, the initiation of the cavitation process requires more energy in viscous solvents and therefore more energy is released upon collapse, resulting in more efficient dispersion of the SWNT aggregates.

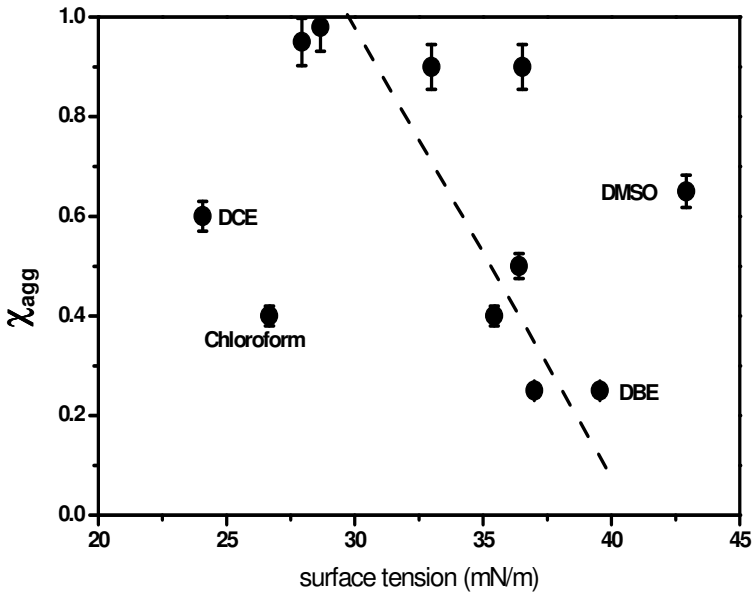

Figure 8.5 Aggregation fractions of SWNTs below the dispersion limits in each solvent as a function of the solvent surface tension. The dashed line is a guide to the eye.

Over the range of solvents, therefore, a good correlation of the solvent parameters governing the sonication process is observed, indicating that this process, rather than conventional solubilisation, is predominant in the dispersion of nanotubes. Notably, it might be expected that parameters such as those described by Hildebrand or Hansen might be more relevant in the regime of high dispersion (i.e. low aggregation fraction). However, the correlation with the sonication parameters appears to extend to this region.

Given the many factors involved in the sonication process, it is not surprising that there is a significant spread, beyond the measured experimental uncertainty, observed in all the plots. It is noted, however, that certain solvents are consistently observed as outliers. DMSO is known to readily absorb water from the environment [19], which might be the reason it behaves anomalously. The deviation of the aggregation fractions in chloroform and DCE is probably

due to the degradation of the solvents themselves and the formation of Cl_2 and HCl during sonication [20]. It is notable, however, that the chlorinated aromatic solvents reported to polymerise under sonication [20, 21], do not appear as outliers. The outlying behaviour of DBE might similarly be due to solvent degradation or alternatively to the extremely high density of DBE compared to other solvents.

For all solvents, parameters such as viscosity are intimately related to the solvent density and thus it is reasonable to expect that the efficiency of the sonication process can be correlated to the solvent density. This is indeed the case, as shown in Figure 8.6. Furthermore, if a constant value for the molecular volume can be simplistically assumed, one would therefore expect a correlation between solvent molecular weight and dispersion efficiency. This is indeed the case as shown in Figure 8.7, suggesting a relatively simple solution to the optimisation of the solubilisation process.

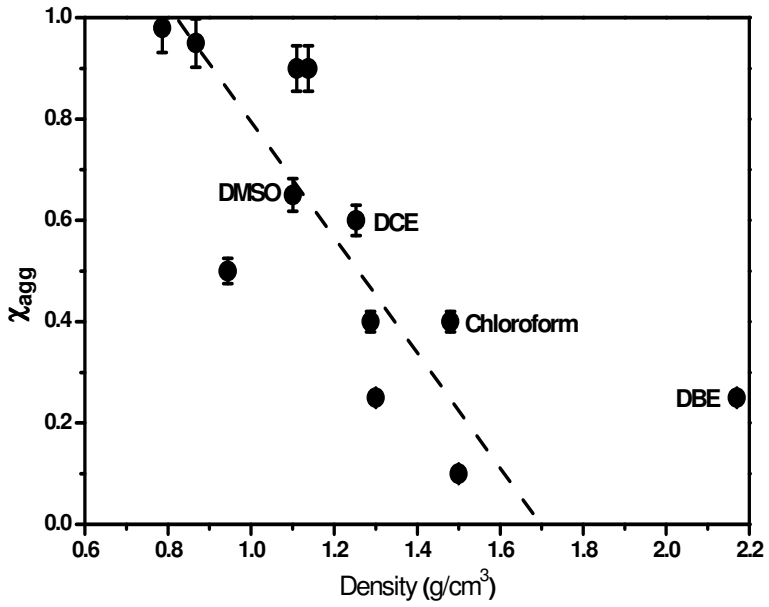

Figure 8.6 Aggregation fractions below the dispersion limit in each solvent as a function of the solvent density. The dashed line is a guide to the eye.

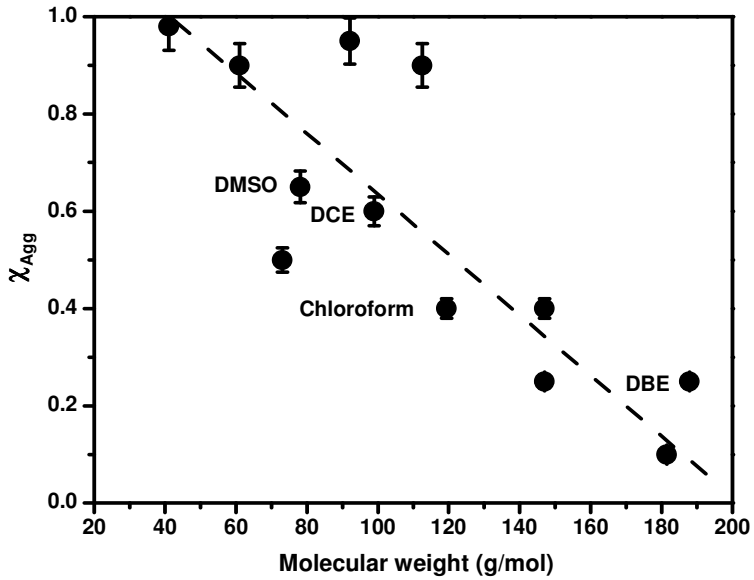

Figure 8.7 Aggregation fractions below the dispersion limit in each solvent as a function of the solvents molecular weight. The dashed line is a guide to the eye.

However, ultrasonication not only affects the exfoliation of the SWNT bundles, it also induces defects and even scission of the tubes [14, 22]. The process is commonly monitored via the ratio of the intensities of the D and G bands of the Raman spectrum, I_D/I_{G+} [3, 15]. It has been demonstrated that changes in the I_D/I_{G+} ratio as a result of sonication are predominately due to nanotube scission [22], and that the ratio scales inversely with the average nanotube length.

Figure 8.8 plots the I_D/I_{G+} ratio in drop cast deposits of *o*-DCB and DMF dispersions which had been sonicated for varying times. Clearly there is a significant change in the ratio, and therefore the average nanotube length, as a result of sonication. It has also been shown that sonication-induced cutting results in the mean tube length decaying as $t^{-1/2}$ [14]. This suggests that I_D/I_{G+} should increase as $\sqrt{t}$, as indicated by the modeled dashed lines of the plot. In both cases, the degradation rate is highest over the first 60-80 s, whereupon it

approaches a plateau. In *o*-DCB, the ratio has increased by a factor of 1.7, while in DMF it has increased by 1.4. This implies a reduction of the average SWNT length by factors of 0.6 and 0.7 respectively. A similar behaviour is seen as a function of sonication power, as shown in Figure 8.9.

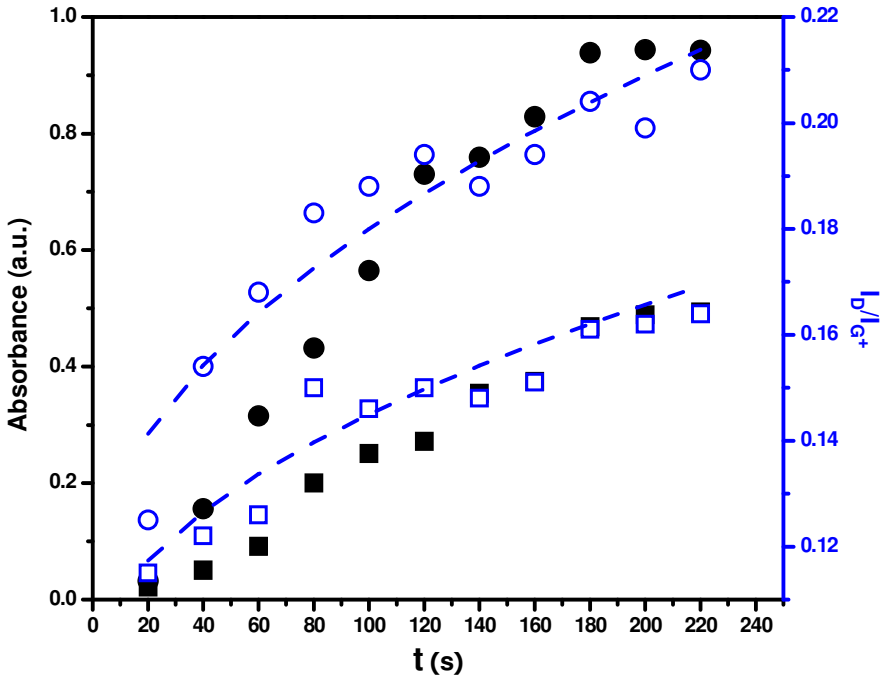

Figure 8.8 Absorbance and I_D/I_{G+} ratio as a function of sonication time. Filled squares: absorbance of DMF solutions; Filled circles: absorbance of *o*-DCB solutions; Open squares: I_D/I_{G+} ratios for DMF solutions; Open circles: I_D/I_{G+} ratios for *o*-DCB solutions; the dashed lines indicate a $\sqrt{t}$ dependence of the I_D/I_{G+} ratio.

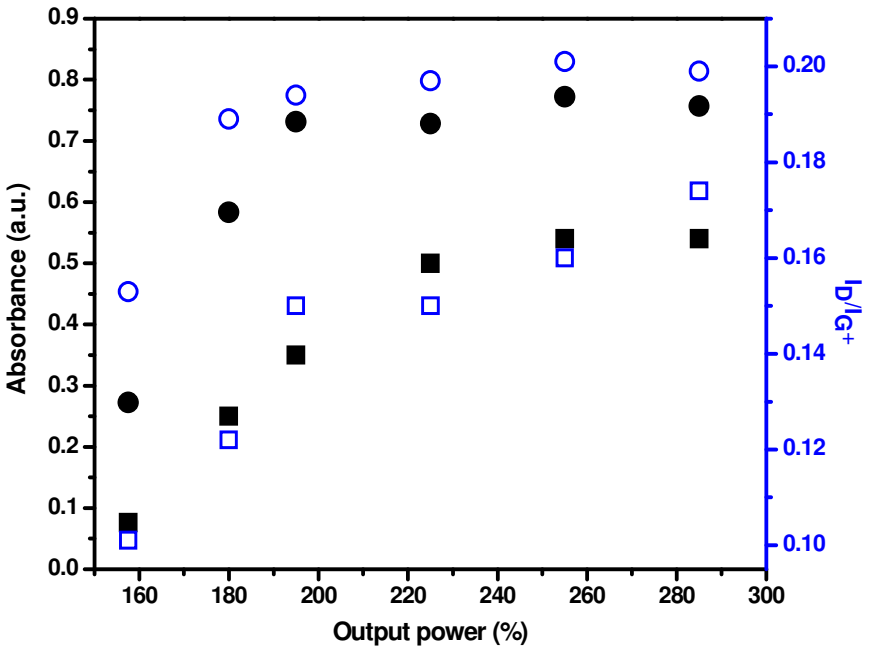

Figure 8.9 Absorbance and I_D/I_{G+} ratio as a function of sonicator output power. Filled squares: absorbance of DMF solutions; Filled circles: absorbance of *o*-DCB solutions; Open squares: I_D/I_{G+} ratios for DMF solutions; Open circles: I_D/I_{G+} ratios for *o*-DCB solutions.

Most significantly, for both solvents, as a function of sonication time and power, the variations of the I_D/I_{G+} ratios correlate well with the absorbance values of Figures 8.1 and 8.2. The absorbance values after sonication for a fixed period, and therefore the aggregation fraction, are thus correlated with the degree of damage to the nanotubes as a result of sonication. In literature, however, these values are taken as a measure of the solubility of SWNTs in the respective solvents. It is unclear as yet whether the susceptibility of SWNTs to degradation, or the degradation rates, are dependent on nanotube chirality or diameter. To date, however, in terms of variations of I_D/I_{G+} ratios and length study of SWNTs by AFM as a function of sonication time, the process has been observed in SWNTs produced by HiPco [14] and pulsed laser vaporization [3, 15], suggesting that it is a relatively universal phenomenon.

8.4 Summary

The dispersion and debundling of SWNTs in organic solvents is critically dependent on the sonication process which is closely dependent on many of the physical parameters of the solvent, including vapour pressure, viscosity, surface tension, density and molecular weight. It appears that these parameters, rather than solubility parameters, govern the dispersion process. The dispersion limit, defined as the concentration at which aggregates cease to dominate the (centrifuged) dispersion appears to be largely independent of sonication conditions, whereas the absorbance of the SWNT dispersions, often used to characterise the degree of solubilisation, increases with the sonication time and the output power of the sonicator. It is furthermore clear that sonication results in damage to the nanotubes and choice of solvent should be guided by minimisation of sonication requirements.

8.5 References

1. Cheng, Q.; Debnath, S.; O'Neill, L.; Hedderman, T. G.; Gregan, E.; Byrne, H. J. Systematic study of the dispersion of SWNTs in organic solvents Journal of physical Chemistry C, 2009, **114**, 4857-4863 .
2. Furtado, C.A.; Kim, U.J.; Gutierrez, H.R.; Pan, L.; Dickey, E.C.; Eklund, P.C. Debundling and dissolution of single-walled carbon nanotubes in

amide solvents. Journal of the American Chemical Society, 2004, **126**, 6095-6105.

3. Giordani, S.; Bergin, S.D.; Nicolosi, V.; Lebedkin, S.; Kappes, M.M.; Blau, W.J.; Coleman, J.N. Debundling of single-walled nanotubes by dilution: Observation of large populations of individual nanotubes in amide solvent dispersions. Journal of Physical Chemistry B, 2006, **110**, 15708-15718.
4. Bahr, J.L.; Mickelson, E.T.; Bronikowski, M.J.; Smalley, R.E.; Tour, J.M. Dissolution of small diameter single-wall carbon nanotubes in organic solvents? Chemical Communications, 2001, 193-194.
5. Landi, B.J.; Ruf, H.J.; Worman, J.J.; Raffaelle, R.P. Effects of alkyl amide solvents on the dispersion of single-wall carbon nanotubes. Journal of Physical Chemistry B, 2004, **108**, 17089-17095.
6. Bergin, S.D.; Sun, Z.Y.; Rickard, D.; Streich, P.V.; Hamilton, J.P.; Coleman, J.N. Multicomponent Solubility Parameters for Single-Walled Carbon Nanotube-Solvent Mixtures. Acs Nano, 2009, **3**, 2340-2350.
7. Bergin, S.D.; Nicolosi, V.; Streich, P.V.; Giordani, S.; Sun, Z.Y.; Windle, A.H.; Ryan, P.; Niraj, N.P.P.; Wang, Z.T.T.; Carpenter, L.; Blau, W.J.; Boland, J.J.; Hamilton, J.P.; Coleman, J.N. Towards solutions of single-walled carbon nanotubes in common solvents. Advanced Materials, 2008, **20**, 1876-1881.
8. Priya, B.R.; Byrne, H.J. Investigation of sodium dodecyl benzene sulfonate assisted dispersion and debundling of single-wall carbon nanotubes. Journal of Physical Chemistry C, 2008, **112**, 332-337.
9. Ham, H.T.; Choi, Y.S.; Chung, I.J. An explanation of dispersion states of single-walled carbon nanotubes in solvents and aqueous surfactant

solutions using solubility parameters. Journal of Colloid and Interface Science, 2005, **286**, 216-223.

10. Cheng, Q.H.; Debnath, S.; Gregan, E.; Byrne, H.J. Effect of Solvent Solubility Parameters on the Dispersion of Single-Walled Carbon Nanotubes. Journal of Physical Chemistry C, 2008, **112**, 20154-20158.
11. Detriche, S.; Nagy, J.B.; Mekhalif, Z.; Delhalle, J. Surface State of Carbon Nanotubes and Hansen Solubility Parameters. Journal of Nanoscience and Nanotechnology, 2009, **9**, 6015-6025.
12. Usrey, M.L.; Chaffee, A.; Jeng, E.S.; Strano, M.S. Application of Polymer Solubility Theory to Solution Phase Dispersion of Single-Walled Carbon Nanotubes. Journal of Physical Chemistry C, 2009, **113**, 9532-9540.
13. Shah, Y.T.; Pandit, A.B.; Moholkar, V.S. Cavitation reaction engineering. 1999, Kluwer Academic/Plenum Publishers: New York.
14. Hennrich, F.; Krupke, R.; Arnold, K.; Stutz, J.A.R.; Lebedkin, S.; Koch, T.; Schimmel, T.; Kappes, M.M. The mechanism of cavitation-induced scission of single-walled carbon nanotubes. Journal of Physical Chemistry B, 2007, **111**, 1932-1937.
15. Bergin, S.D.; Sun, Z.; Streich, P.; Hamilton, J.; Coleman, J.N. New Solvents for Nanotubes: Approaching the Dispersibility of Surfactants Journal of Physical Chemistry C, 2010, **114**, 231-237.
16. Cheng, Q.; Debnath, S.; Gregan, E.; Byrne, H.J. Effects of chlorinated aromatic solvents on the dispersion of HiPco SWNTs. Physica Status Solidi B-Basic Solid State Physics, 2008, **245**, 1947-1950.
17. Mason, T.J.; Lorimer, J.P. Sonochemistry: Theory, applications and uses of ultrasound in chemistry. 1988, Ellis Horwood Limited.

18. Mason, T.J.; Lorimer, J.P. Applied sonochemistry: the uses of power ultrasound in chemistry and processing. 2002, Wiley VCH.

19. Ellson, R.; Stearns, R.; Mutz, M.; Brown, C.; Browning, B.; Harris, D.; Qureshi, S.; Shieh, J.; Wold, D. In situ DMSO hydration measurements of HTS compound libraries. Combinatorial Chemistry & High Throughput Screening, 2005, **8**, 489-498.

20. Moonoosawmy, K.R.Kruse, P. To dope or not to dope: The effect of sonicating single-wall carbon nanotubes in common laboratory solvents on their electronic structure. Journal of the American Chemical Society, 2008, **130**, 13417-13424.

21. Niyogi, S.; Hamon, M.A.; Perea, D.E.; Kang, C.B.; Zhao, B.; Pal, S.K.; Wyant, A.E.; Itkis, M.E.; Haddon, R.C. Ultrasonic dispersions of single-walled carbon nanotubes. Journal of Physical Chemistry B, 2003, **107**, 8799-8804.

22. Lucas, A.; Zakri, C.; Maugey, M.; Pasquali, M.; van der Schoot, P.; Poulin, P. Kinetics of Nanotube and Microfiber Scission under Sonication. Journal of Physical Chemistry C, 2009, **113**, 20599-20605.

CHAPTER 9
SUMMARY

9.1 Summary of the results

The aim of this work was to perform a systematic study of the dispersion of as-produced HiPco SWNTs in a series of organic solvents, and to establish the parameters which govern the dispersion/debundling process.

Motivated by the high solubility of SWNTs in *o*-DCB and MCB reported in literature, a systematic study of the solubility of as-produced HiPco SWNTs was conducted in Chapter 4 across a series of chlorinated aromatic solvents. Although the samples contain catalytic particles and other impurities, for many applications dispersion of as-produced samples is desirable. Stable dispersions of SWNTs have been demonstrated in some of these solvents. Although the effect of sonication time was only investigated in one solvent, the result shows that this process is of great importance in the preparation of stable SWNT dispersions.

A UV-Vis-NIR spectrometer equipped with an integrating sphere enables the measurement of the contribution of scattering, which is due to the suspended bundles in the solution. Significant difference in the efficacy of the solvents measured to disperse SWNTs was observed. No clear structure-property relationships are apparent. The similar structure between SWNTs and the aromatic solvent molecules is not the dominant factor and no correlation with

surface energies is observed. The results indicated a more in depth analysis of solubility parameters is necessary.

In order to further investigate the effect of solvents solubility parameters on the dispersion of SWNTs, 4 more solvents reported as dispersive agents of SWNTs, namely toluene, chloroform, DCE and DMF, were included in Chapter 5.

In most cases, however, it is more appropriate to consider SWNT dispersions to be “suspensions” rather than “solutions” and due to the presence of large bundles, the scattering of the light cannot be ignored. In assessing the characteristics of the suspension by absorption spectroscopy, it is of critical importance to differentiate between extinction due to scattering and due to true absorption as the ability to suspend bundles for a short time is not the same as the ability to debundle and suspend individual tubes. For chlorinated aromatic solvents, scattering from bundles is about 50% of the total extinction. For other solvents investigated, no significant difference between the two is observed however indicating efficient debundling below the dispersion limit.

In terms of the Hildebrand solubility parameter, the solubilisation of SWNTs in chlorinated aromatic solvents varies systematically but the trend is independent of that of the other reference solvents. Similar correlation with Hansen solubility parameters is observed for δ_{P} and δ_{H}. Both the extinction and absorption coefficients appeared to increase within the investigated range of δ_{P} and δ_{H}. No correlation was observed for either total extinction coefficient or absorption coefficient with δ_{D} however.

The systematic study therefore helped to elucidate some of the structure property relationships governing dispersion of SWNTs and further studies

should seek to extend the basis set. However, although the other reference solvents show a similar correlation with δ_P, the trend line is different and so it is not a universal solubility parameter. An understanding of the underlying physical origin of the different trends could however lead to the determination of such a universal parameter.

The two different linear correlations of extinction/absorption coefficient and solvent solubility parameters between chlorinated aromatic solvents and others observed in Chapter 5 indicated that there might be a selectivity of different types of tubes by different solvents. As the solubilities of SWNTs in some of the solvents are quite low, it limited the utilization of UV-Vis-NIR absorption spectra for differentiating metallic and semiconducting tubes.

In order to investigate any selectivity of the examined solvents on different electrical properties of SWNTs, an entire Raman investigation of the SWNT sample used in this study was conducted in Chapter 6. Structural assignments of pristine SWNTs were carried out based on the linear correlation between ω_{RBM} and $1/d$. The linear correlation parameters between ω_{RBM} *and* $1/d$ were found to vary significantly with the laser energy. The SWNTs dispersed in DMF and *o*-DCB were examined with Raman spectroscopy and compared with pristine SWNTs. The results showed that, in both solvents, smaller diameter SWNTs dominated the solutions. However, no chirality or electrical property selectivity was observed with the two solvents, although they appeared on the two different trend lines.

In order to further understand the effect of solubility parameters on the dispersion of SWNTs, based on the eight solvents investigated in Chapter 5,

five additional solvents, DBE, NMP, nitromethane, acetonitrile and DMSO, were added according to their solubility parameters in Chapter 7.

Correlations between the dispersion limit (D_L) and solvent solubility parameters, including the Hildebrand solubility parameter and three dimensional Hansen solubility parameters, were explored, demonstrating that SWNTs are easily dispersed in solvents with a Hildebrand solubility parameter range from ~22-24 $MPa^{1/2}$ and Hansen polarity component (δ_P) ~12-14 $MPa^{1/2}$. No clear correlation between dispersion limits and the dispersion force (δ_D) or hydrogen bonding force (δ_H) are evident. It was found, however, that the degree of dispersion depends critically on sample preparation conditions and in particular sonication time. Increased sonication times increase the amount of SWNT debundled and solubilised but do not appear to affect the dispersion limit. However, increased sonication also induces discernible changes to the SWNTs themselves and in itself influences their solubility, under which conditions no clear solubility parameters can be determined. The results indicate that further systematic investigation of the sonication process is merited in order to differentiate the solubilising effects from the results of physical and/or chemical modification of the samples themselves.

Chapter 8 reported a systematic study of the dispersion of SWNTs in organic solvents during ultrasonication, the effect of sonication parameters and solvent parameters, including vapour pressure, viscosity, surface tension, density and molecular weight, which were reported to affect the cavitation process. It appeared that these parameters, rather than solubility parameters, govern the dispersion process. The dispersion limit, defined as the concentration at which

aggregates cease to dominate the (centrifuged) dispersion appears to be largely independent of sonication conditions, whereas the absorbance of the SWNTs dispersion, often used to characterise the degree of solubilisation, increases with the sonication time and the output power of the sonicator. It was furthermore clear that sonication results in damage to the nanotubes and choice of solvent should be guided by minimisation of sonication requirements.

9.2 Future Prospect

This work conducted a systematic study of the interaction between as-produced HiPco SWNTs and a series of organic solvents, and in doing so, established the correlation between dispersion limit and solvents solubility parameters, which would be useful in the research of dispersing nanoparticles and carbon based nanomaterials. However, the properties of as-produced carbon nanotubes synthesized by different techniques have been reported to vary significantly. The applicability of the established correlations for other types of SWNTs requires further study.

As-produced SWNT samples contain both metallic and semiconducting tubes which hinder them for some specific electrical applications. Although different techniques have been developed to separate metallic and semiconducting SWNTs, they are still limited by the separation efficiency and cost. Mass production of carbon nanotubes with either metallic or semiconducting character, or ideally with specific chirality is desirable.

The debundling and stabilizing process of SWNTs in liquid phase normally cannot be achieved without ultrasonication. Long time and high power sonication are critical to increase the solubility of SWNTs, but the process damages the tubes. The damage during sonication also relates to the solvent properties. The choice of solvents should consider both the ability to disperse SWNTs and minimisation of sonication requirements. Currently there are a few solvents which are capable of forming SWNT solutions with relatively high concentrations. These solvents are however normally characterized by high toxicity [1] or strong acidity [2]. The safety of these SWNT solutions remains therefore a matter of concern.

The high cost of good quality SWNTs is another obstacle for large scale application of SWNTs. SWNT samples of over 75% purity cost over 600 Euros per gram from Sigma Aldrich and SWNTs with specific chirality can cost up to nearly 900 Euros per gram [3].

In summary, the development of synthesis techniques is the fundamental solution for solving the existing problems. The search for solvents for SWNTs should not only consider high solubility, but damage minimisation and handling safety should also be considered.

9.3 References

1. Bergin, S.D.; Sun, Z.Y.; Streich, P.; Hamilton, J.; Coleman, J.N. New Solvents for Nanotubes: Approaching the Dispersibility of Surfactants. Journal of Physical Chemistry C, 2010, **114**, 231-237.
2. Davis, V.A.; Parra-Vasquez, A.N.G.; Green, M.J.; Rai, P.K.; Behabtu, N.; Prieto, V.; Booker, R.D.; Schmidt, J.; Kesselman, E.; Zhou, W.; Fan, H.; Adams, W.W.; Hauge, R.H.; Fischer, J.E.; Cohen, Y.; Talmon, Y.; Smalley, R.E.; Pasquali, M. True solutions of single-walled carbon nanotubes for assembly into macroscopic materials. Nature Nanotechnology, 2009, **4**, 830-834.
3. http://www.sigmaaldrich.com/catalog/Lookup.do?N5=All&N3=mode+matchpartialmax&N4=single+wall+carbon+nanotubes&D7=0&D10=single+wall+carbon+nanotubes&N1=S_ID&ST=RS&N25=0&F=PR. (10/03/2010)

LIST OF PUBLICATIONS AND PRESENTATIONS

Publications

1. **Qiaohuan Cheng**, Sourabhi Debnath, Elizabeth Gregan and Hugh J. Byrne, Ultrasound-assisted SWNTs dispersion: effects of sonication parameters and solvent properties, ***Journal of Physical Chemistry C,*** 114 (19), 8821 - 8827 (2010).

2. Qiaohuan Cheng, Sourabhi Debnath, Luke O'Neill, Theresa G. Hedderman, Elizabeth Gregan and Hugh J. Byrne, Systematic study of the dispersion of SWNTs in organic solvents, ***Journal of Physical Chemistry C,*** 114 (11), 4857 - 4863 (2010).

3. Qiaohuan Cheng, Sourabhi Debnath, Elizabeth Gregan and Hugh J. Byrne, Vibrational mode assignments for bundled single-wall carbon nanotubes using Raman spectroscopy at different excitation energies, ***Applied Physics A***, Jan. 2010, submitted.

4. Sourabhi Debnath, **Qiaohuan Cheng**, Theresa G. Hedderman and Hugh J. Byrne, A comparative study of the interaction of different polycyclic aromatic hydrocarbons on different types of single walled carbon nanotubes, ***Journal of Physical Chemistry C***,114 (18), 8167 - 8175 (2010).

5. Sourabhi Debnath, **Qiaohuan Cheng**, Theresa G. Hedderman and Hugh J. Byrne, A Raman spectroscopy study of the solubilisation of SWCNTs by polycyclic aromatic hydrocarbons, ***Carbon***, 48, 1489 - 1497 (2010).

6. Qiaohuan Cheng, Zhanxia Lü and Hugh J. Byrne, Synthesis of Maleic Anhydride grafted polypropylene-butadiene copolymer and its application in PP/OMMT/SBS composite as compatibilizer, ***Journal of Applied Polymer Science***, 114 (3), 1820 - 1827(2009).

7. Qiaohuan Cheng, Sourabhi Debnath, Elizabeth Gregan and Hugh J. Byrne, Effect of Solvent Solubility Parameters on the Dispersion of Single-Walled Carbon Nanotubes, ***Journal of Physical Chemistry C***, 112 (51), 20154-20158 (2008).

8. Sourabhi Debnath, **Qiaohuan Cheng**, Theresa G. Hedderman and Hugh J. Byrne, A study of the interaction between single walled carbon nanotubes and polycyclic aromatic hydrocarbons: towards structure-property relationships, ***Journal of Physical Chemistry C,*** 112, 10418 - 10422 (2008).

9. Qiaohuan Cheng, Sourabhi Debnath, Elizabeth Gregan and Hugh J. Byrne, Effects of chlorinated aromatic solvents on the dispersion of HiPco SWNTs, ***Physica Status Solidi B,*** 245, 1947 - 1950 (2008).

10. Sourabhi Debnath, **Qiaohuan Cheng**, Theresa G. Hedderman and Hugh J. Byrne, An experimental study of the interaction between single walled carbon nanotubes and polycyclic aromatic hydrocarbons, ***Physica Status Solidi B,*** 245, 1961 - 1963 (2008).

Poster Presentation

1. 1st Inspire Bionano International Conference Dublin, Ireland, 15th -16th October, 2009.

2. 10th International Conference in the Science and Applications of Nanotubes (NT09) Beijing, China, 20th - 26th June, 2009.

3. 9th International Conference in the Science and Applications of Nanotubes (NT08) Montpellier, France, 29th June - 4th July, 2008.

4. 22nd International Winterschool on Electronic Properties of Novel Materials (IWEPNM), Kirchberg, Austria, 1st -8th March 2008.

5. 21st International Winterschool on Electronic Properties of Novel Materials (IWEPNM), Kirchberg, Austria, 10th -17th March 2007.